

Deficient autophagy in epithelial stem cells drives aging in the freshwater cnidarian *Hydra*

Szymon Tomczyk¹, Nenad Suknovic¹, Quentin Schenkelaars¹, Yvan Wenger¹, Kazadi Ekundayo¹, Wanda Buzgariu¹, Christoph Bauer¹, Kathleen Fischer², Steven Austad² and Brigitte Galliot^{1,*}

ABSTRACT

Hydra possesses three distinct stem cell populations that continuously self-renew and prevent aging in *Hydra vulgaris*. However, sexual animals from the *H. oligactis* cold-sensitive strain *Ho_CS* develop an aging phenotype upon gametogenesis induction, initiated by the loss of interstitial stem cells. Animals stop regenerating, lose their active behaviors and die within 3 months. This phenotype is not observed in the cold-resistant strain *Ho_CR*. To dissect the mechanisms of *Hydra* aging, we compared the self-renewal of epithelial stem cells in these two strains and found it to be irreversibly reduced in aging *Ho_CS* but sustained in non-aging *Ho_CR*. We also identified a deficient autophagy in *Ho_CS* epithelial cells, with a constitutive deficiency in autophagosome formation as detected with the mCherry-eGFP-LC3A/B autophagy sensor, an inefficient response to starvation as evidenced by the accumulation of the autophagosome cargo protein p62/SQSTM1, and a poorly inducible autophagy flux upon proteasome inhibition. In the non-aging *H. vulgaris* animals, the blockade of autophagy by knocking down *WIPI2* suffices to induce aging. This study highlights the essential role of a dynamic autophagy flux to maintain epithelial stem cell renewal and prevent aging.

KEY WORDS: Aging model system, Autophagy sensor, Epithelial stem cells, *Hydra* regeneration, Evolution of aging, p62/SQSTM1, *WIPI2*, Rapamycin

INTRODUCTION

Studies using short-lived invertebrate organisms, such as the fruit fly or the nematode, have dramatically improved our understanding of aging (Helfand and Rogina, 2003; Longo and Finch, 2003; Olsen et al., 2006). However, these model systems have some drawbacks, such as developmental pausing under stress, implying that the life-prolonging interventions may work through mechanisms not present in humans (Austad, 2009). Additionally, except for the *Drosophila* gut, adult somatic tissues do not self-renew in flies and nematodes, whereas self-renewal is

an essential component of homeostasis in humans. Finally, a significant proportion of human orthologous genes were lost in fly and nematodes as evidenced by their presence in cnidarians, a bilaterian sister group (Kortschak et al., 2003; Wenger and Galliot, 2013; Schenkelaars et al., 2018). Therefore, additional invertebrate models could be profitably developed to help discover novel genes, pathways and mechanisms relevant for human aging (Valenzano et al., 2017). Among those, *Hydra*, a small carnivorous freshwater cnidarian polyp with a radially organized bi-layered body plan, is equipped with three distinct adult stem cell populations that continuously self-renew whatever the age of the animal (Fig. 1A-C). This dynamic homeostasis supports the amazing ability to regenerate any missing part (Galliot, 2012). In laboratory conditions, the mortality of *Hydra vulgaris* (*Hv*) remains negligible over the years as well-fed animals remain asexual, reproducing by budding without showing replicative aging (Brien, 1953; Martínez, 1998; Schaible et al., 2015).

The multifunctional but unipotent epithelial stem cells from the epidermis and the gastrodermis (eESCs and gESCs, respectively) cycle every 3–4 days whereas the multipotent interstitial stem cells (ISCs), which provide both somatic and germ cells (Fig. 1C), cycle every 24–30 h, faster than the ESCs (Hobmayer et al., 2012; Buzgariu et al., 2014). As a result, animals transiently exposed to anti-proliferative drugs rapidly lose their ISCs and interstitial progenitors (collectively named i-cells) and progressively become nerve-free animals (Marcum and Campbell, 1978; Sugiyama and Fujisawa, 1978; Buzgariu et al., 2014). If force-fed, such epithelial *Hydra* remain viable and able to bud and regenerate likely due to the rapid adaptation of their ESCs, which modify their genetic program (Wenger et al., 2016).

By contrast, another *Hydra* species named *H. oligactis* (*Ho*) undergoes aging when the temperature drops to 10°C, a condition that induces gametogenesis, budding arrest and progressive animal degeneration (Brien, 1953; Littlefield et al., 1991; Yoshida et al., 2006). The massive production of gametes is accompanied by the loss of somatic interstitial cells, cytoskeleton disorganization, decline in body movements and feeding behavior (Yoshida et al., 2006; Tomczyk et al., 2015, 2019). Sexual animals from male and female *Ho* strains die within 4 months, showing Gompertzian mortality dynamics normally associated with aging (Finch, 1990) whereas *Ho* animals maintained at 18°C exhibit no signs of aging. Here, we used cold transfer to induce aging and analyze the cellular and molecular basis of aging in *Hydra*. We identified two *Ho* strains, one cold-sensitive (*Ho_CS*) that undergoes aging and another, cold-resistant (*Ho_CR*) that survives gametogenesis (Fig. 1D). In this study, we investigated the epithelial properties in these two strains and we found striking differences in epithelial stem cell renewal and autophagy efficiency in aging and non-aging animals.

¹Department of Genetics and Evolution, Institute of Genetics and Genomics in Geneva (IGE3), University of Geneva, CH-1205 Geneva, Switzerland. ²Department of Biology, University of Alabama at Birmingham, Birmingham, AL 35294, USA.

*Author for correspondence (brigitte.galliot@unige.ch)

DOI: 10.1242/dev.177840; S.T., 0000-0002-2283-3156; Q.S., 0000-0002-8622-6443; Y.W., 0000-0002-6162-1527; W.B., 0000-0002-8492-6470; C.B., 0000-0002-0783-8119; K.F., 0000-0003-4431-4629; S.A., 0000-0003-4798-8442; B.G., 0000-0001-7596-8284

This is an Open Access article distributed under the terms of the Creative Commons Attribution License (<https://creativecommons.org/licenses/by/4.0>), which permits unrestricted use, distribution and reproduction in any medium provided that the original work is properly attributed.

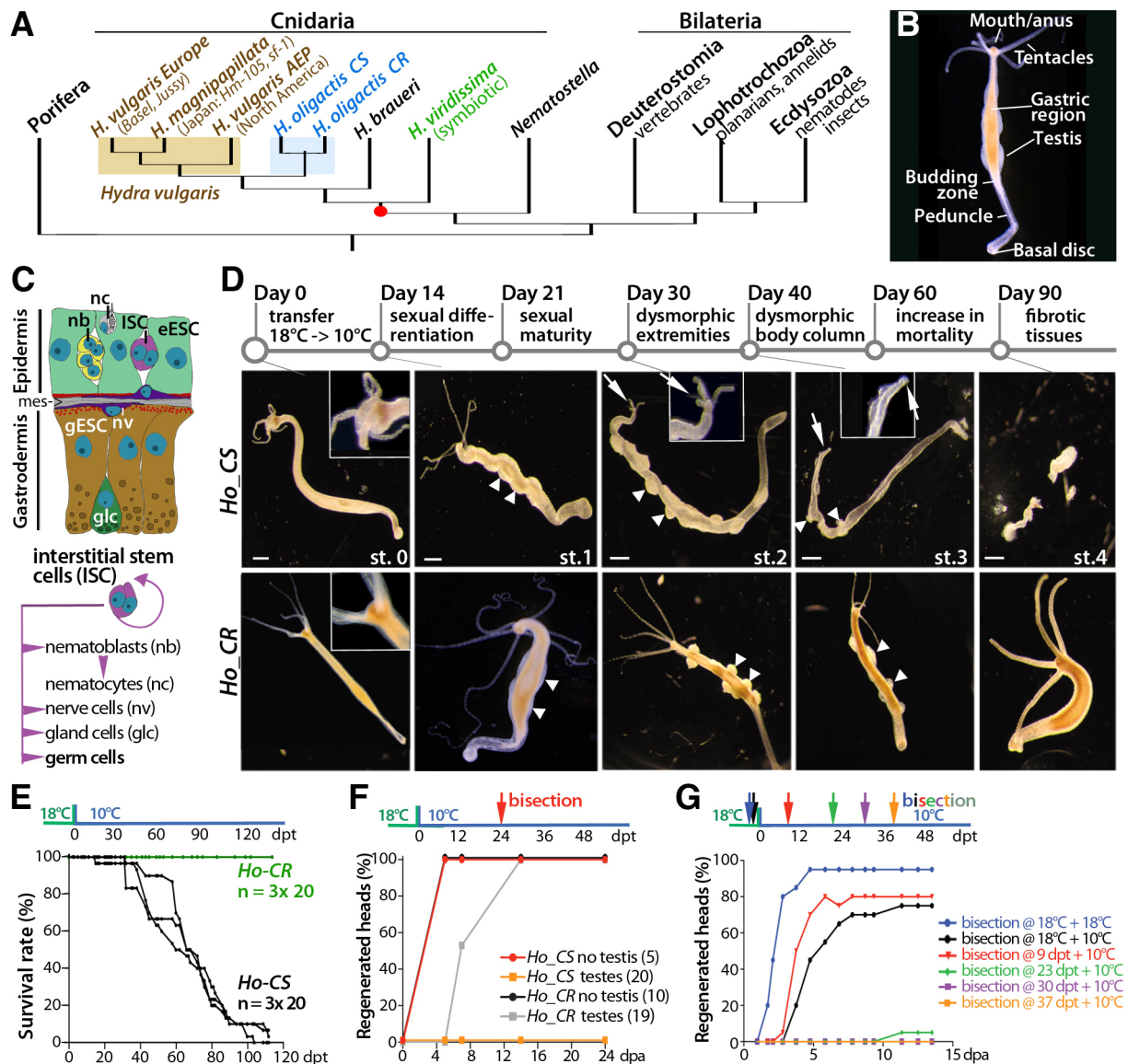


Fig. 1. Inducible aging phenotype in cold-sensitive *Hydra oligactis* (*Ho_CS*). (A) Phylogenetic position of *Hydra* among metazoans. (B) Anatomy of a male *H. oligactis* animal. (C) Schematic view of *Hydra* gastric tissue. Mes, mesoglea. (D) Morphological changes observed in *Ho_CS* (top) and *Ho_CR* (bottom) animals at various time points after transfer to 10°C (day 0); arrowheads indicate testes, arrows indicate head regions. Scale bars: 500 μm. (E) Survival rates among *Ho_CR* and *Ho_CS* cohorts maintained at 10°C for 120 days. (F) Head regeneration in *Ho_CR* or *Ho_CS* animals selected for the presence or the absence of testes, bisected at mid-gastric level on day 24 post-transfer (dpt) and monitored for 24 days post-amputation (dpa). (G) Head regeneration measured in *Ho_CS* animals bisected at 18°C (blue, black) or at various time points after transfer to 10°C (9, 23, 30, 37 dpt) and monitored for 15 days.

RESULTS

The aging phenotype observed in *Ho_CS* in response to gametogenesis

To investigate aging in *Hydra*, we used two closely related male strains named *Ho_CR* and *Ho_CS*, which exhibit a similar budding rate at 18°C but respond differently to cold exposure (Fig. 1, Fig. S1). After cold transfer, ~70% *Ho_CR* animals remained asexual and healthy and ~30% reached sexual maturity within 25 days, then lost sexual traits and returned to physiological fitness without exhibiting aging signs (Fig. 1D,E, Fig. S1B). After 300 days at 10°C, all *Ho_CR* animals were healthy and budding, some showing mild dysmorphic signs, such as duplicated basal region and non-detached buds (not shown). By contrast, after transfer to 10°C, *Ho_CS* animals stopped budding within 4 weeks (Fig. S1B,C), differentiated testes for 90% of them and developed

an irreversible aging phenotype that includes tentacle shrinking, head loss and stenosis of the body column as previously reported (Yoshida et al., 2006). Their survival time was negatively correlated to the testis number (Fig. S1D,E). Within 1 month, *Ho_CS* animals lost the ability to regenerate (Fig. 1F,G) and showed behavioral defects (Tomczyk et al., 2019) and aging became irreversible (Fig. S1F-N). Hence, *Ho_CS* but not *Ho_CR* animals undergo aging in response to cold-induced gametogenesis. We then decided to compare the properties of stem cells in these two strains, by selecting animals differentiating at least four testes.

Impact of gametogenesis on somatic interstitial cells in *Ho_CS* and *Ho_CR*

To monitor the impact of gametogenesis, we first analyzed the DNA content profiles of cells from *Ho_CS* and *Ho_CR* animals at various

time points after transfer to 10°C (Buzgariu et al., 2014). At 25 days post-transfer (dpt) we noted a similar proportion of haploid and diploid cells and similar cell cycle profiles in both strains, at 35 dpt the number of haploid cells dropped significantly in *Ho_CR* but not in *Ho_CS*, and at 45 dpt haploid cells could no longer be detected in *Ho_CR* animals but were still present in *Ho_CS*, representing over

20% of all cells (Fig. 2A,B). At 35 dpt the fraction of S-phase cells was much higher in *Ho_CR* than in *Ho_CS* animals, suggesting a recovery of somatic interstitial proliferation. To confirm this transient versus sustained impact of gametogenesis on the stock of somatic i-cells, we quantified the proportion of i-cells and ESCs on macerated tissues over a 50-day period. In both strains we recorded a

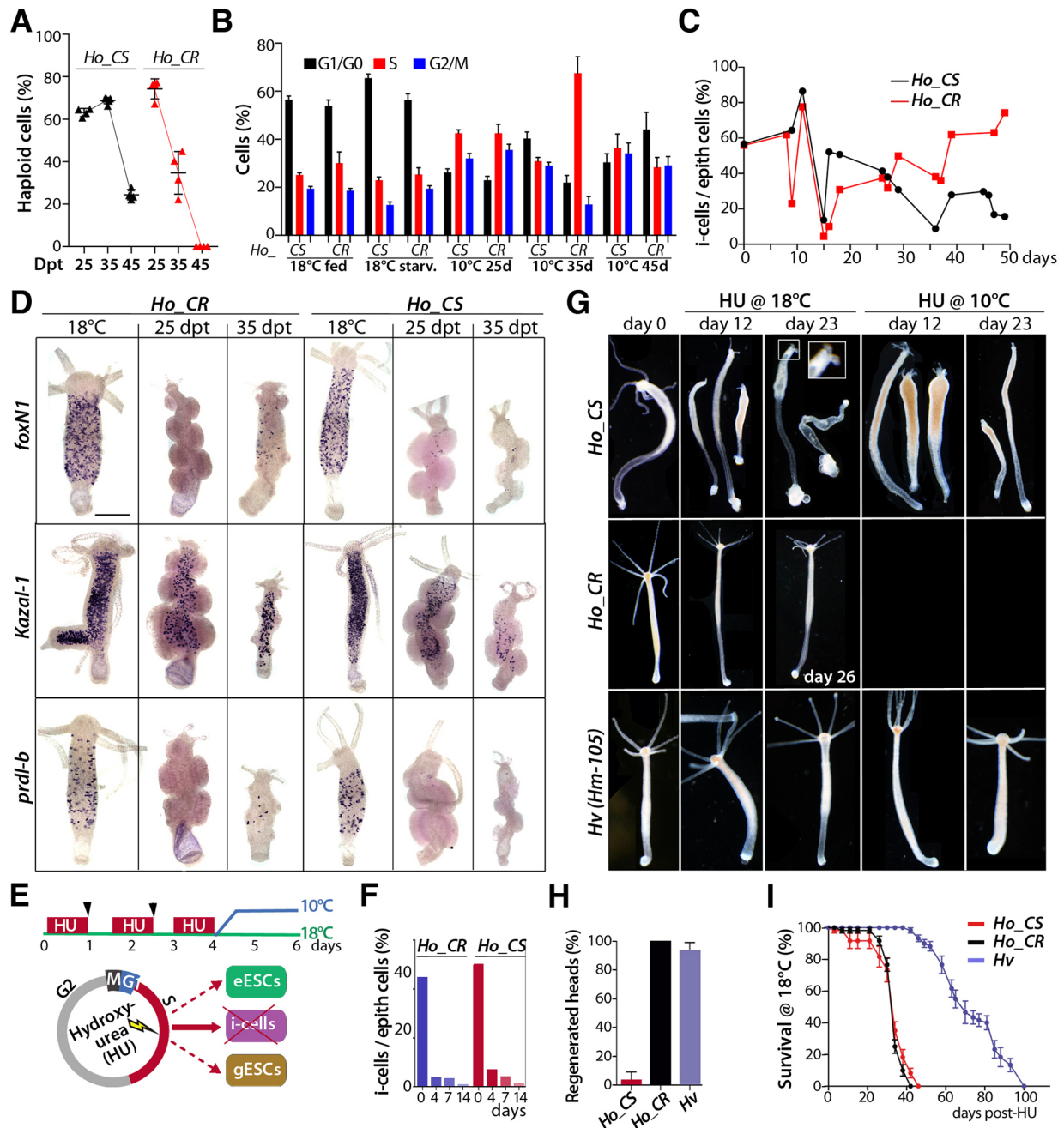


Fig. 2. Somatic interstitial loss upon gametogenesis-induced aging and pharmacological induction of aging in asexual *Ho_CS* animals.

(A,B) Modulations in haploid cell content (A) and cell cycle profiles (B) detected by flow cytometry in *Ho_CS* and *Ho_CR* animals maintained at 18°C or at 10°C for 25, 35 or 45 days; starv., 7-day starvation. Error bars represent s.d. (C) Fraction of interstitial cells (i-cells, single and pairs) over epithelial (epith) cells counted in macerated tissues (300 cells minimum per condition). (D) Expression of *foxN1* in i-cells, *Kazal-1* in gland cells and *prdl-b* in nematoblasts in *Ho_CS* and *Ho_CR* animals before and after transfer to 10°C ($n=20$ animals/condition). Scale bar: 300 µm. (E) Hydroxyurea (HU) treatment given as three successive 24 h pulses eliminates all cycling i-cells without affecting the ESCs, which cycle three to four times slower. Arrowheads indicate feeding times. (F) Fraction of i-cells over epithelial cells measured in *Ho_CR* and *Ho_CS* animals maintained at 18°C and analyzed before (day 0) or after HU treatment initiation (4, 7, 14 days). (G) HU-induced morphological changes noted in animals taken 12 or 23 days after day 0. Inset in the top row shows a magnification of the boxed area. (H) Head regeneration of *Ho_CS* and *Ho_CR* animals bisected 9 days after HU treatment initiation ($n=3 \times 10$). (I) Survival rate of HU-treated *Hv*, *Ho_CS* and *Ho_CR* animals ($n=6 \times 10$). Error bars represent s.e.m. values in H,I. All HU treatments were performed as shown in E.

maximal decrease in the interstitial fraction at 15 dpt, followed by a complete recovery in *Ho_CR* by 40 dpt and a transient and partial recovery in *Ho_CS* (Fig. 2C). These results indicate that gametogenesis leads to a massive loss of somatic interstitial cells in both strains, which is rapidly compensated for in *Ho_CR* but not in *Ho_CS*.

The expression patterns of *FoxN1*, *prdl-b* and *Kazal-1* in ISCs, nematoblasts and gland cells, respectively, confirmed the massive drop of expression at 25 dpt in both strains, followed by a recovery at 35 dpt in *Ho_CR* but not in *Ho_CS* (Fig. 2D). To monitor the recovery of somatic i-cells at the molecular level, we compared the RNA-seq profiles of 20 genes expressed in the interstitial lineages (Wenger et al., 2016). In *Ho_CS* and *Ho_CR* animals maintained at 10°C, we found 16/20 genes downregulated within the first 2 weeks after transfer, half of them showing a persisting low level of expression, and the other half showing at 35 dpt a secondary upregulation in *Ho_CR*, which was lacking or only partially observed in *Ho_CS* (*Cnnos2*, *cnox-2*, *foxN1*, *Notchl4*, *Pax-A*, *Cnvas1*, *Cnvas2*, *ZNF845*; Fig. S2A,B, Table S1).

We also compared the downregulation of these 20 interstitial-lineage markers in asexual *H. vulgaris* (*sf-1* strain) animals exposed to antiproliferative drugs [hydroxyurea (HU) and colchicine] or to heat-shock as reported by Wenger et al. (2016) with that measured in sexual *H. oligactis* strains: 11/20 genes exhibited a more drastic reduction of expression 10 days after drug or heat-shock exposure in *Hv_sf-1* than during gametogenesis in *Ho_CS* (see *CnASH*, *Cnnos1*, *Cnnos2*, *cnox-2*, *foxN1*, *myc1*, *NOWA*, *Pax-A*, *prdl-b*, *Hyzic*, *ZNF845* in Fig. S2C). This result indicates that the loss of somatic i-cells is more extensive after drug or heat-shock treatment in *Hv_sf-1* than in aging *Ho_CS* animals. Nevertheless, *Hv_sf-1* animals totally depleted of their i-cells remain fit whereas *Ho_CS* animals partially depleted of their i-cells undergo aging.

Pharmacological induction of aging in *Ho_CS* in the absence of gametogenesis

Next, we tested the impact of interstitial cell loss in the absence of gametogenesis. We compared the respective responses to somatic i-cell loss in *Ho_CS* animals undergoing gametogenesis, and in asexual *Ho_CS* and *Ho_CR* animals maintained at 18°C and exposed to HU (Fig. 2E). We recorded a similar rapid global loss of i-cells in HU-treated *Ho_CS* and *Ho_CR* animals (Fig. 2F), which was actually faster than in animals maintained at 10°C (compare Fig. 2F with 2C). We also noted that *Ho_CS* but not *Ho_CR* animals exhibited an aging phenotype at 18°C when exposed to HU. This phenotype is similar to that observed after cold-induced gametogenesis although it was detected much earlier (Fig. 2G, upper row), indicating that gametogenesis is not necessary to promote an aging phenotype in *Ho_CS*. By contrast, the *Ho_CR* animals exhibited a starvation phenotype after HU treatment, characterized by a lack of dysmorphic features and a reduced thickness and size, whereas *Hv* animals remained fit longer (Fig. 2G, middle and lower rows). *Hv* and *Ho_CR* animals were able to regenerate their head structures when bisected 9 days after HU treatment but *Ho_CS* were not (Fig. 2H). Despite these phenotypic differences, both *Ho_CS* and *Ho_CR* animals died within 6 weeks, whereas *Hv* animals were resistant to HU-induced i-cell depletion for twice as long (Fig. 2I). In *Ho_CR* the death occurred abruptly, whereas in *Ho_CS* it corresponded to a progressive deterioration.

To explain the low survival of *Ho_CR* animals after HU treatment at 18°C, we analyzed the bacterial load in each strain because in *H. oligactis* commensal bacteria populate the epithelial cells

(Fraune and Bosch, 2007). We found the bacterial load in epithelial cells to be constitutively lower in *Ho_CR* than in *Ho_CS* but expanded upon HU treatment in *Ho_CR* epithelial cells (Fig. S3A). To test the deleterious effect of this bacterial load, we exposed HU-treated animals to an antibiotic cocktail (Wein et al., 2018) and recorded in *Ho_CR* cohorts an improved fitness and a prolonged survival (Fig. S3B,C), suggesting that the heavier bacterial load after HU impacts animal survival. In *Ho_CS* animals, the bacterial load remained low after HU and the antibiotic cocktail treatment was toxic.

Epithelial response to interstitial cell loss in *Ho_CS*

Besides the i-cell loss, we also analyzed the global morphology of the epithelial layers in *Ho_CS* and *Ho_CR* animals, either after gametogenesis or after HU treatment (Fig. 3). In *Ho_CS* we detected a progressive disorganization of the muscle fibers, implying a loss of contractile function after 35 to 50 days at 10°C, whereas these myofibrils remained organized in *Ho_CR* (Fig. 3A,B). In *Ho_CS* animals exposed to HU at 18°C, we also recorded dramatic alterations of the myoepidermal network after 28 days (Fig. 3C). To test whether epithelial cell proliferation is modified during aging, we labeled live animals with bromo-2'-deoxyuridine (BrdU) for 96 h and quantified the proportion of BrdU-positive ESCs at various time points during cold exposure (Fig. 3D). From 40% BrdU⁺ cells at 18°C (day 0), we noted in both strains a rapid decline during the first 2 weeks post-transfer, followed by a stabilization with about 20% epithelial cells remaining cycling in *Ho_CR*. By contrast, in *Ho_CS* the stock of epithelial cycling cells dropped below 10% at day 25, and showed a slight recovery at later time points. Similarly, after HU treatment at 18°C, the stock of epithelial cycling cells first dropped during the first 2 weeks then became progressively re-established within 28 days in *Ho_CR* whereas it continued to decline in *Ho_CS* animals (Fig. 3E). At the molecular level, the upregulation of a large subset of cell cycle genes observed in *Ho_CR* animals was delayed in *Ho_CS* ones (Figs S4, S5, Table S2), which is in agreement with their inability to maintain epithelial proliferation after i-cell loss. In *H. vulgaris*, ESCs appear to adapt to i-cell loss (Wenger et al., 2016), therefore we hypothesized that the epithelial adaptation to i-cell loss is deficient in *Ho_CS*, a deficiency that contributes to the aging phenotype (Fig. 3F). As induction of autophagy is a key epithelial response to environmental changes in *Hydra* (Buzgariu et al., 2008; Chera et al., 2009), we decided to investigate the autophagy response in aging and non-aging *Hydra*.

Starvation does not induce autophagy in *Ho_CS*

Autophagy is a dynamic flux that degrades intracellular components, a process essential for homeostasis and the stress response (Yu et al., 2018). Upon autophagy induction, double-membrane vesicles named autophagosomes form, which sequester part of the cytoplasm, then fuse with lysosomes to form autolysosomes that degrade their content. In *H. vulgaris* epithelial cells, the autophagy flux is enhanced upon starvation or stress (Buzgariu et al., 2008; Chera et al., 2009). As a first approach, we starved animals maintained at 18°C and noted a slower decrease in size and thickness in *Hv* animals, which lived twice as long as *Ho* ones (Fig. S6A,B). Despite the similar survival rate of starved *Ho_CS* and *Ho_CR* animals, we noted striking differences on histological sections, the former ones undergoing a dramatic reduction of their gastrodermis during an 11-day starvation (Fig. 4A). On sections analyzed by electronic microscopy, we could identify autophagosomes in *H. vulgaris* cells but rarely in *Ho_CS* ones (Fig. S6C). The ubiquitin-like protein ATG8/LC3,

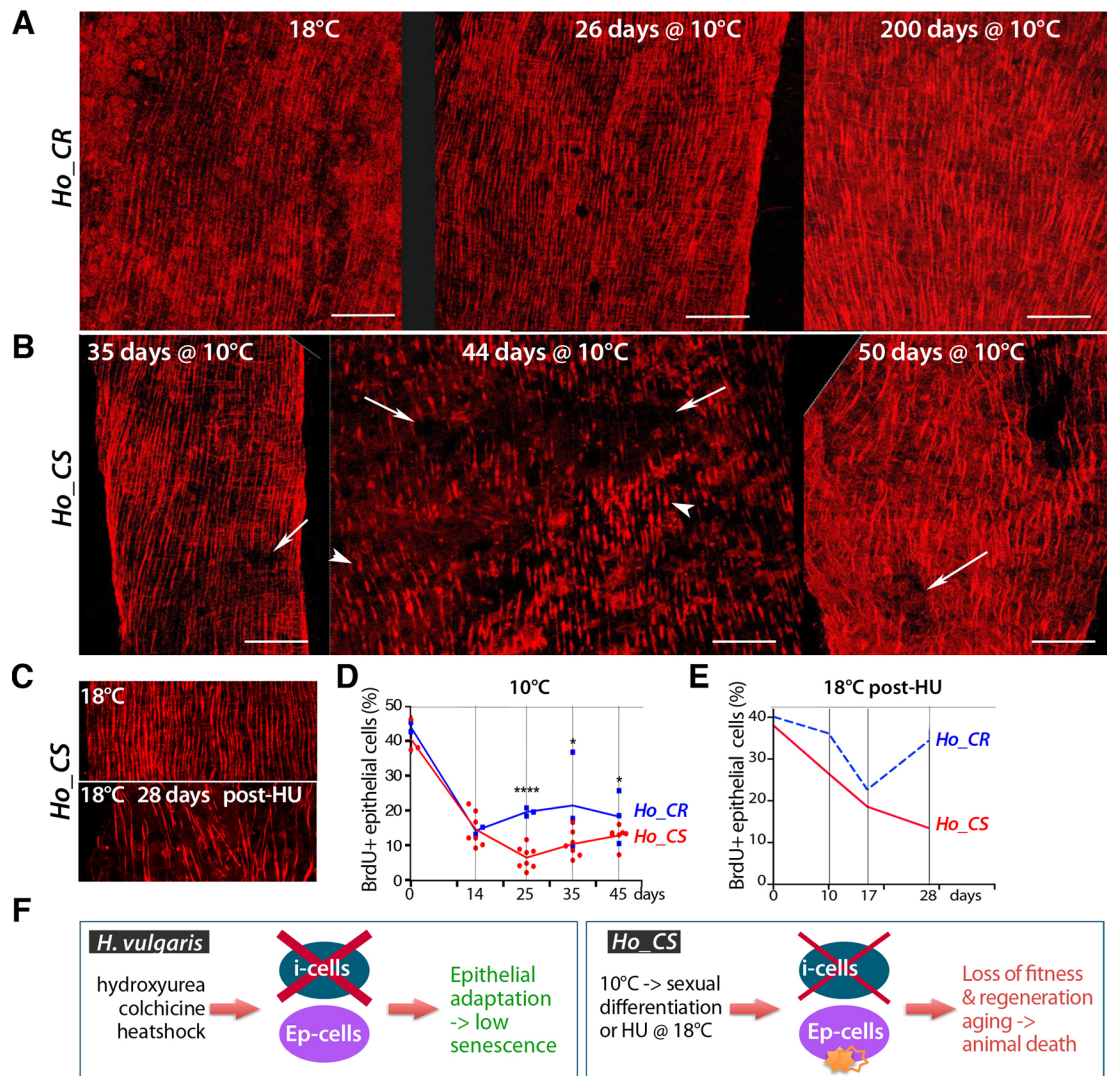


Fig. 3. Disorganization of the epithelial epidermal layer in aging *Ho_CS* animals. (A,B) Phalloidin staining of the epidermis in *Ho_CR* and *Ho_CS* animals transferred to 10°C and fixed at the indicated time points. Arrows indicate disorganized regions of the epidermis, arrowheads indicate shortened myofibrils. Scale bars: 50 µm. (C) Phalloidin staining of the epidermis in control or HU-treated *Ho_CS* animals maintained at 18°C and fixed after 28 days. (D,E) BrdU-labeling index values measured after 96 h BrdU exposure performed at the indicated time points either after transfer to 10°C (D) or after HU treatment at 18°C as in Fig. 2E. In D, each dot corresponds to a replicate in which at least 300 cells were counted. In E, animals were maintained at 18°C. * $P < 0.05$, **** $P < 0.0001$ (unpaired t -test). (F) Scheme comparing the impact of i-cell loss in *Hv* animals, in which epithelial stem cells adapt (Wenger et al., 2016), and in *Ho_CS*, in which a more limited i-cell loss is lethal, suggesting a lack of epithelial adaptation.

which is an essential autophagosome component (Birgisdottir et al., 2013), is encoded by two *LC3*-related genes in *Hydra* (*LC3A/B*, *LC3C*), predominantly expressed in ESCs (Figs S7 and S8).

To detect autophagosomes, we used an anti-human LC3B antibody that detects in one-day starved animals maintained at 18°C LC3-positive puncta and vacuoles (Fig. 4B,C). We defined puncta as small structures, approximately 1 µm in diameter, containing LC3 signal detected either in fixed cells after anti-LC3 immunolabeling or in live conditions in cells expressing the LC3-GFP-mCherry recombinant protein (Fig. 4G-L). By contrast, vacuoles are larger structures, several microns in diameter limited by a LC3⁺ rim that commonly surrounds a MitoTracker-positive core; they correspond to mature autophagosomes. Puncta were quantified by automated Imaris analysis whereas vacuoles were counted manually. After a 17-day starvation, the number of both vacuoles and LC3 puncta were significantly increased in *Hv* and *Ho_CR* animals but not in *Ho_CS* ones (Fig. 4D,E). Surprisingly, in

daily-fed *Ho_CS* animals the number of LC3 puncta was constitutively high, decreasing with starvation, whereas in cold-maintained *Ho_CS* animals, which progressively stop eating, the number of LC3 vacuoles did not increase between day 0 and day 35, but increased moderately later between day 35 and day 45 (Fig. 4F). All these results suggest that autophagy regulation is altered in *Ho_CS*.

Proteasome inhibition does not induce compensatory autophagy in *Ho_CS*

As in mammals, autophagy plays a crucial role in proteostasis and is upregulated upon proteasome inhibition (Kocaturk and Gozuacik, 2018), we used proteasome inhibition to induce autophagy in *Hydra*. We first tested the sensitivity of *Hydra* to the proteasome inhibitor MG132, and treated the animals either continuously over 6 days, or for a 16-h pulse (Fig. S9). In both conditions, *Ho_CS* animals showed signs of toxicity long before *Ho_CR* and *Hv* ones, suggesting a deficiency in compensatory autophagy. To visualize the autophagy

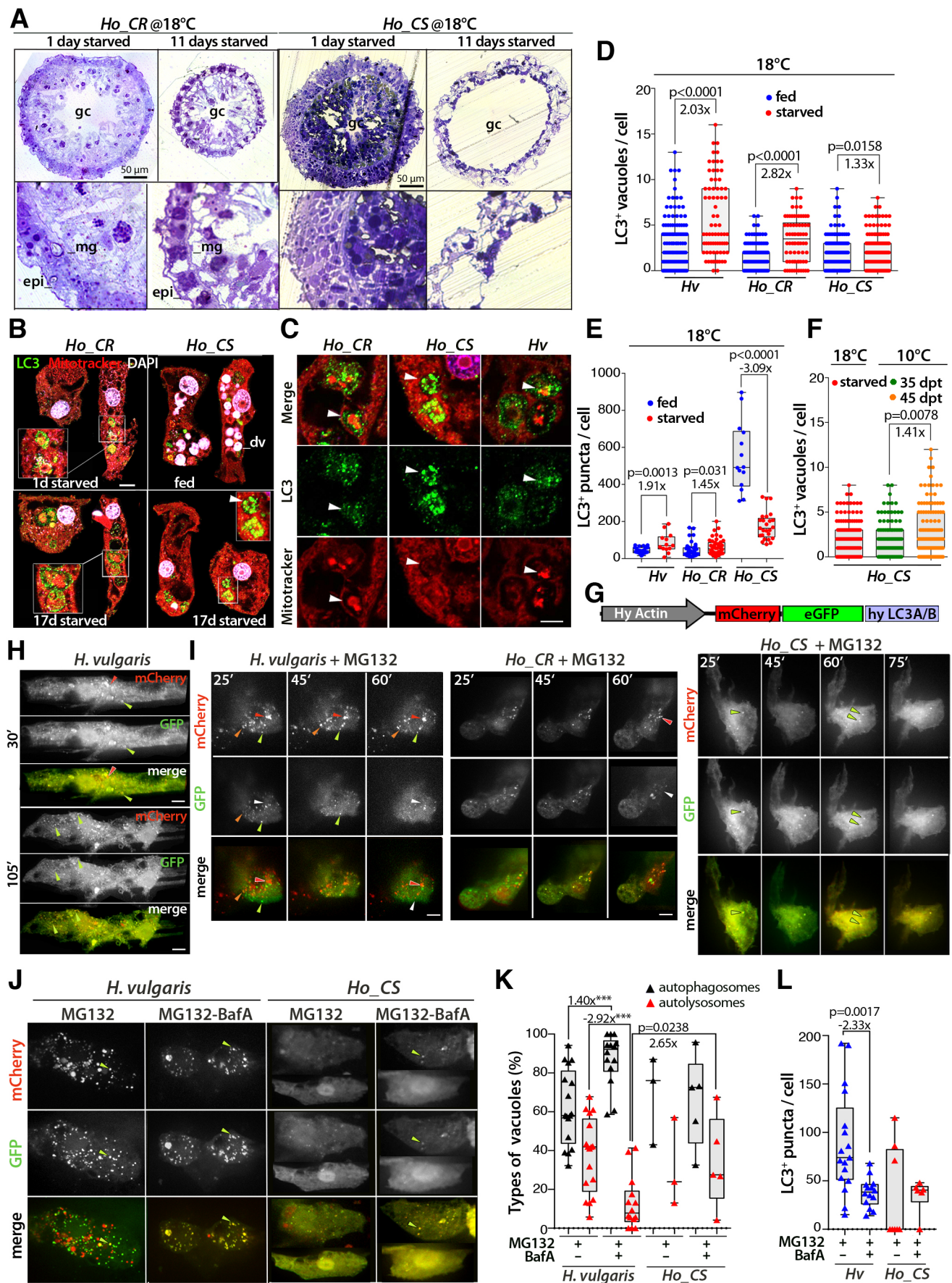


Fig. 4. See next page for legend.

Fig. 4. Deficiency in the inducibility of the autophagy flux in ESCs from *Ho_CS* animals. (A) Toluidine-stained transversal sections of gastric regions from 1- and 11-day starved animals. Lower panel show enlarged areas of the panels above. epi, epidermis; gc, gastric cavity; mg, mesoglea. (B) Detection of autophagic vacuoles (arrowhead) and digestive vacuoles (dv, pink) in epithelial cells immunostained for LC3 (green) and stained with MitoTracker (red) and DAPI (white). Scale bar: 10 μ m. (C) Enlarged view of the LC3⁺ structures shown in B. Arrowheads indicate circular LC3⁺ structures surrounding sequestered portions of cytoplasm. Scale bar: 5 μ m. (D,E) Number of LC3⁺ vacuoles (D) or LC3 puncta (E) in ESCs of regularly fed or 17-day starved *Hv*, *Ho_CR* and *Ho_CS* animals maintained at 18°C. (F) Number of LC3⁺ vacuoles in ESCs of *Ho_CS* maintained at 10°C for 35 or 45 days. (G) Structure of the mCherry-eGFP-hyLC3A/B dual autophagy sensor. (H,I) Live imaging of ESCs expressing the autophagy sensor in regularly fed *Hv*, *Ho_CR* or *Ho_CS* animals maintained at 18°C either untreated (H) or exposed to MG132 immediately before imaging (I). Green arrowheads indicate autophagosomes, orange arrowheads autophagosomes losing GFP fluorescence and red and white arrowheads autolysosomes. (J) Live imaging of ESCs expressing the autophagy sensor in *Hv* or *Ho_CS* animals exposed before imaging to MG132 for 3 h and to BafA (100 nM) for 16 h or not. Green arrowheads indicate autophagosomes. (K) Distribution of the LC3⁺ vacuoles between autophagosomes (black triangles) and autolysosomes (red triangles). (L) Number of LC3⁺ puncta in the cells shown in J. For box and whisker plots, the box indicates the 25th to 75th percentile, the line shows the median and the whiskers indicate the smallest and the largest value. Points represent individual values. *P*-values calculated using unpaired *t*-test. ****P*=0.0003.

flux, we modified the mCherry-eGFP-LC3 sensor produced by Pankiv et al. (2007). This chimeric protein is anchored in phagosomes, shows bi-fluorescence (green and red) in early and mature autophagosomes, but monofluorescence (red only) in autolysosomes, in which the pH-sensitive GFP fluorescence is quenched upon acidification after lysosome fusion (Pankiv et al., 2007). For the *Hydra* sensor, we coupled mCherry and eGFP to the *Hydra* LC3A/B protein under the control of the *Hydra* actin promoter (Fig. 4G). Animals electroporated with the mCherry-eGFP-hyLC3A/B plasmid expressed the chimeric protein for several days in a limited number of epidermal epithelial cells that were imaged 2 days after electroporation on whole intact animals in the presence of MG132.

In *Hv* and *Ho_CR* animals, the GFP fluorescence of most mCherry-GFP-hyLC3 puncta persisted in untreated animals (Fig. 4H) but vanished within 60 min of MG132 exposure, indicating an efficient activation of the autophagy flux (Fig. 4I). By contrast, in *Ho_CS* epithelial cells the fluorescence was constitutively diffuse and the rare mCherry-GFP-LC3 puncta remained stable in the presence of MG132. In epithelial cells exposed to MG132 in combination with bafilomycin A (BafA), which prevents lysosome fusion, the autophagic vacuoles remained stable in *Hv* and the diffuse LC3 pattern in *Ho_CS* remained unmodified (Fig. 4J). As expected, upon BafA treatment the proportion of autolysosomes decreased and the proportion of autophagosomes increased as they accumulated in the absence of autolysosome formation in *Hv* cells (Fig. 4K). The total number of LC3 puncta, including both the autophagosomes (green, yellow) and the autolysosomes (red), decreased in *Hv* cells after BafA treatment, suggesting that these cells form fewer autophagic vacuoles (Fig. 4L). In *Ho_CS* cells, the formation of LC3 puncta was limited although seemingly enhanced upon BafA treatment and the ratio of autophagosomes to autolysosomes did not vary (Fig. 4K,L). These *in vivo* assays confirm the poor inducibility of the autophagy flux in *Ho_CS*.

Differential gene regulation of the autophagy machinery in *Ho_CS* and *Ho_CR*

In mammals, the autophagy machinery is tightly controlled at the transcriptional level by FoxO and TFEB (Füllgrabe et al., 2016).

As this machinery is highly conserved in *Hydra* (Chera et al., 2009), we investigated gene regulation of the autophagy machinery in aging versus non-aging animals. Through a transcriptomic analysis performed in *Ho_CS* and *Ho_CR* animals, we compared the RNA-seq profiles of 75 genes linked to autophagy (Figs S10 and S11, Table S3). We found 51/75 genes specifically regulated at 10°C, 34/51 transiently upregulated in both strains but for 21/34 with a 10-day delay in *Ho_CS* compared with *Ho_CR*, 5/51 upregulated in *Ho_CR* but poorly in *Ho_CS* (*Ambra1*, *Atg16L1*, *Becn1*, *Rab24*, *Vamp7*), 4/51 transiently upregulated in *Ho_CS* but poorly in *Ho_CR* (*Atg2B*, *Atg4C*, *Plekhf2*, *Tollip*) and 7/51 upregulated at late time points in *Ho_CS* (*Atg4B*, *Atg7*, *Calr*, *DAPK1*, *LAMP1*, *NBR1*, *p62/SQSTM1*). These profiles indicate distinct regulations of the autophagy flux in *Ho_CS* compared with *Ho_CR*.

The lack of *Ambra1* and *Beclin-1* upregulation in *Ho_CS* points to a deficient initiation of phagosome formation at 10°C, whereas the stronger upregulation of *Ulk1/2* and *Atg13* in *Ho_CS* might reveal a possible regulatory feedback loop mechanism to activate the Ulk1 complex, which is crucial for activation of the Beclin-1 complex. In agreement with a deficient initiation, we noted a delayed upregulation of *Atg4B*, which encodes the protease required for LC3 cleavage, an essential step for autophagosome elongation. Also *Rab24*, which encodes a small GTPase required for terminating starvation-independent autophagy (Ylä-Anttila et al., 2015), shows a limited upregulation in *Ho_CS*. Finally, the late upregulation in *Ho_CS* of *NBR1* and *p62/SQSTM1* (named here *p62*) likely reflects a blockade of the autophagy flux. The shuttle receptor *p62*, which binds and brings polyubiquitylated proteins to proteasomal or autophagic degradation, accumulates when its cargo is not properly degraded (Seibenhener et al., 2004; Bjørkøy et al., 2005; Johansen and Lamark, 2011). In cnidarians, *p62* is well conserved, is present as a single gene in *Hydra* and is predominantly expressed in ESCs (Figs S12 and S13A–C). Upregulation of *p62* in aging *Ho_CS* might be interpreted as an additional sign of inefficient autophagy flux.

The *p62/SQSTM1* protein is a marker of deficient autophagy in *Hydra*

To monitor the *p62* regulation in aging animals further, we raised a polyclonal antibody against the *Hydra* *p62* C-terminus (Fig. 5A, Fig. S12). As anticipated, *p62* levels were lower in *p62(RNAi)* animals, and increased in MG132-treated animals (Fig. 5B). Also, *p62* colocalized with LC3⁺ autophagosomes in immunocytological analyses (Fig. 5C, Movie 1). *Ho_CS* animals showed higher *p62* levels than *Ho_CR* ones when maintained at 10°C (Fig. 5D), but also when starved at 18°C and/or treated with MG132 (Fig. 5E). As expected, *p62* accumulated when autophagy was inhibited with BafA, although to a much higher level in *Ho_CS* than in *Ho_CR* (Fig. 5D), indicating that autophagy contributes to *p62* degradation in both *Ho_CS* and *Ho_CR* animals. As *p62* binds polyubiquitylated (polyUb) proteins through its UBA domain, we analyzed whether an increase in *p62* levels correlates with a parallel increase in polyUb proteins. At 18°C, MG132-treated *Ho_CS* animals exhibited a dose-dependent increase in both *p62* and polyUb proteins (Fig. 5F, Fig. S14A); however, the polyUb pattern on western analysis was different between *Ho_CS* and *Ho_CR*, with high molecular bands more abundant in *Ho_CS* (Fig. 5G). Finally, we noted a decrease in the level of polyUb proteins in *p62(RNAi)* *Ho_CR* animals but not in *Ho_CS* ones, suggesting that the *p62*-dependent autophagy blockade induces an enhanced compensatory proteasome degradation in *Ho_CR* but not in *Ho_CS* animals (Fig. 5H). Hence, the accumulation of *p62* protein in *Ho_CS*

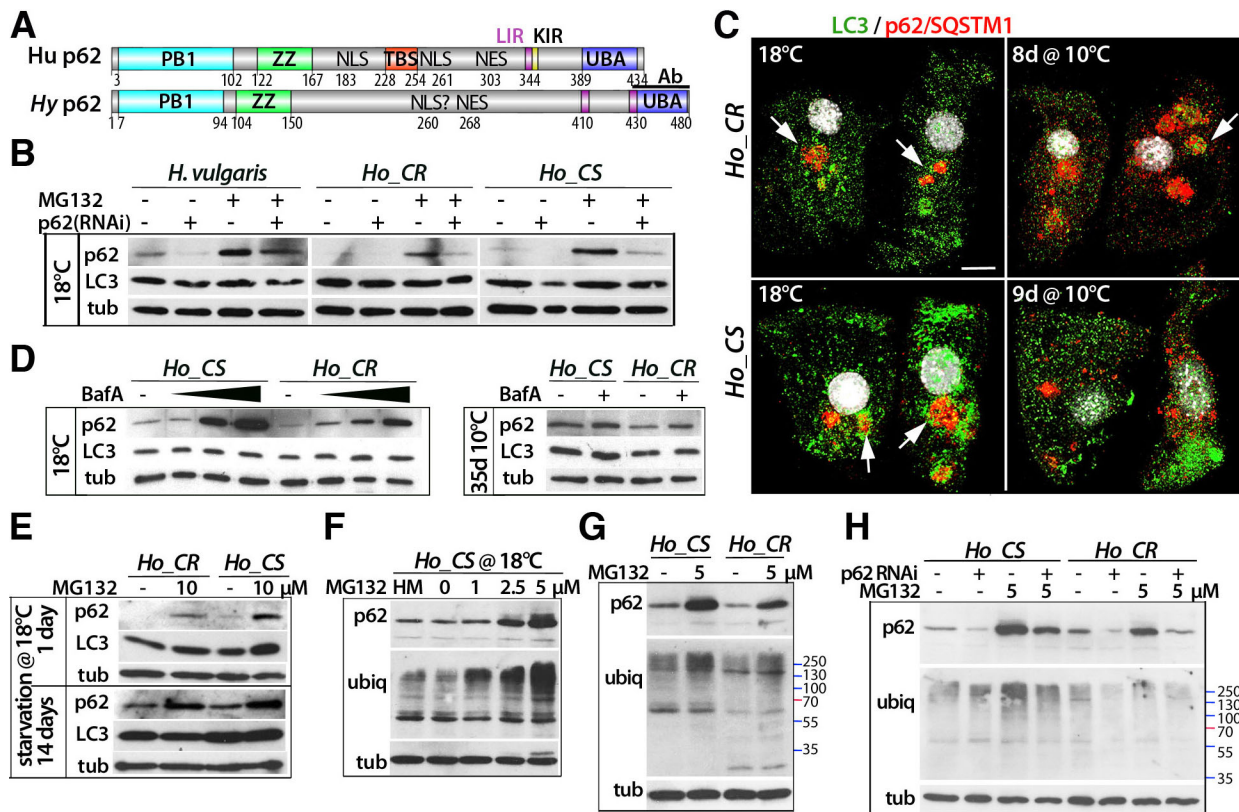


Fig. 5. Modulation of p62/SQSTM1 expression levels in *Ho_CS* animals. (A) Structure of the human (Hu) and *Ho* p62/SQSTM1 (p62) proteins (see Fig. S12). 'Ab' indicates the region used to raise the anti-*Hydra* p62 antibody. (B) p62 levels in p62(RNAi) animals exposed or not to MG132; tub: α -tubulin. (C) Epithelial cells immunostained with the anti-*Hydra* p62/SQSTM1 (red) and the anti-human LC3 (green) antibodies, co-stained with DAPI (white). Arrows point to p62-labeled granules associated with LC3. Scale bar: 10 μ m. (D,E) p62 levels in animals treated with increasing levels of BafA (D, left), or maintained at 10°C for 35 days and exposed or not to BafA (D, right), or starved for 1 or 14 days and exposed to MG132 (E). (F-H) p62 levels and ubiquitin patterns in animals exposed to MG132 (F,G), or knocked down for p62 and exposed to MG132 (H). Except in D (right), all animals were maintained at 18°C and drug treatments given for 16 h.

animals in response to physiological or pharmacological signals known to induce autophagy confirms the hypothesis of deficient autophagy flux. The parallel analysis of p62 and polyUb protein levels also confirms that the cross-talk between autophagy and proteasome degradation is less active in *Ho_CS* than in *Ho_CR*.

Rapamycin delays aging and improves epithelial proliferation in *Ho_CS*

In yeast, as in mammals, the macrolide compound rapamycin acts as a potent inhibitor of MTORC1 (Mechanistic Target of Rapamycin Complex 1), a complex that integrates signals coming from nutrients and energy levels. Through MTORC inhibition, rapamycin promotes resistance to starvation and induces autophagy, a necessary condition for lifespan extension (Bjedov et al., 2010; Fontana et al., 2010; Shen and Mizushima, 2014). To test the effect of rapamycin on *Hydra* aging, we continuously exposed *Ho_CS* animals to rapamycin from day 2 at 10°C and noted a significant improvement of the morphology, the contractility and the regenerative ability of treated animals (Fig. 6A, Fig. S14B). At 58 dpt, the head region, which was highly degenerated in untreated *Ho_CS* animals, remained equipped with tentacles in rapamycin-treated animals, which survived about 3 weeks longer (Fig. 6B). On histological sections, the attrition of the gastrodermis previously observed in aging animals (Fig. 3A) was reduced upon rapamycin treatment and the testes exhibited a flattened shape and contained fewer mature sperm cells (Fig. 6C, Fig. S14C). We measured the effect of rapamycin treatment on epithelial cell proliferation by monitoring the BrdU-labeling index at various time

points after transfer to 10°C (Fig. 6D). The rapamycin treatment did not prevent the initial decline in ESC proliferation in *Ho_CS* but promoted the recovery of cell cycling as observed at 35 dpt and 45 dpt, when 20% ESCs were observed to be cycling, a level similar to that recorded in untreated *Ho_CR* animals (see Fig. 3D). We assume that the drastic reduction in ESC proliferation observed during gametogenesis or after HU treatment plays an important role in *Hydra* aging, and that rapamycin delays aging through the restoration of epithelial proliferation.

Rapamycin does not enhance the autophagy flux in *Ho_CS*

Next, we tested whether the positive effects of rapamycin on health and lifespan in *Ho_CS* are mediated by a rescue of the deficient autophagic flux. In rapamycin-treated animals, we recorded at 35 dpt a modest increase (1.47 \times) in the number of LC3⁺ vacuoles (Fig. 6E), still p62 levels were increased in *Ho_CS* but lowered in *Ho_CR*, suggesting an efficient induction of autophagy in *Ho_CR* but not in *Ho_CS* (Fig. 6F). These results were confirmed by two independent quantitative proteomic analyses that showed an increase in p62 levels at 35 dpt in rapamycin-treated *Ho_CS* animals (Fig. 6G, Fig. S14D). *In vivo* analysis with the autophagy sensor showed a rapid activation upon rapamycin exposure of the autophagy flux in ESCs from *Hv* and *Ho_CR* but not in ESCs from *Ho_CS*, in which the mCherry-eGFP-LC3A/B fluorescence remained predominantly cytoplasmic with rare LC3⁺ puncta that persisted for 90 min after rapamycin exposure (Fig. 6H). All these results point to a persistent blockade of the autophagy flux in

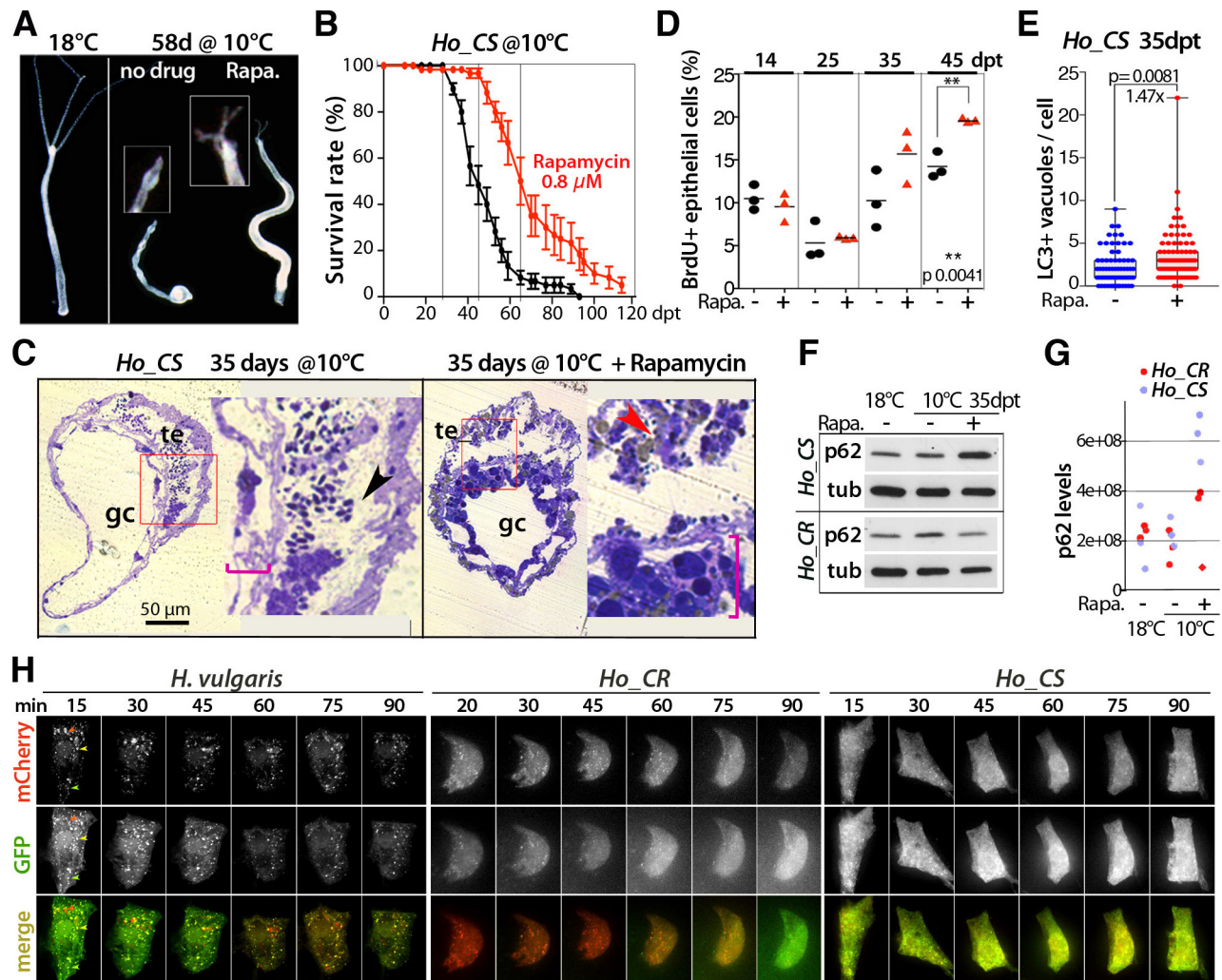


Fig. 6. Rapamycin treatment delays aging in *Ho_CS* without enhancing the autophagy flux. (A,B) Aging phenotype at 58 dpt (A) and survival rate (B) in *Ho_CS* animals exposed, or not, to rapamycin from day 3 (dpt). Error bars represent s.e.m. (C) Toluidine-stained transversal sections of gastric regions from untreated (left) or rapamycin-treated (right) *Ho_CS* animals taken at 35 dpt. Red boxes indicate the enlarged areas shown on the right; pink brackets indicate gastrodermis thickness; black arrowhead indicates sperm cells in the testis lumen and red arrowhead indicates sperm cells engulfed in an epithelial cell. gc, gastric cavity; te, testis. (D) BrdU-labeling index values measured after 96 h BrdU exposure in *Ho_CS* animals maintained at 10°C in the presence (red triangles) or absence (black circles) of rapamycin. (E) Number of LC3+ vacuoles in ESCs of *Ho_CS* animals exposed (red dots) or not (blue dots) to rapamycin. Error bars represent s.d.; *P*-values calculated using the unpaired *t*-test. (F,G) p62 levels assessed by western blotting (F) or proteomic analysis (G) in *Ho_CR* and *Ho_CS* animals maintained at 18°C or transferred to 10°C and exposed to rapamycin for 35 days. tub: α -tubulin. (H) Live imaging of epithelial cells transiently expressing the mCherry-eGFP-hyLC3A/B autophagy sensor in animals maintained at 18°C and exposed to rapamycin (0.8 μM) from day 0. Arrowheads indicate newly formed autophagosomes with full GFP fluorescence and limited mCherry fluorescence (green); mature autophagosomes with double fluorescence GFP/mCherry (yellow); or autolysosomes with quenched GFP fluorescence (red).

Ho_CS despite the presence of rapamycin, indicating that the positive effects of the rapamycin treatment on aging in *Ho_CS* are mediated via a distinct mechanism. We incidentally found that the epithelial cells from rapamycin-treated animals contain numerous sperm cells (Fig. S14E,F, Movie 2), pointing to a possible rapamycin-induced enhanced engulfment.

The genetic blockade of autophagy in *H. vulgaris* impacts animal fitness and survival

As autophagy seems to play a pivotal role in the aging process of *Ho_CS*, we tested whether impairing autophagy in the non-aging *H. vulgaris* species promotes aging. To impair the autophagy process, we selected *WIP12* for RNAi knockdown, a gene well conserved across metazoans (Fig. S15, Fig. S16A) that encodes the WD-repeat domain phosphoinositide-interacting protein 2, involved

in the recruitment of the Atg12–5–16L1 complex, which is essential for LC3 conjugation and autophagosome formation (Dooley et al., 2014) (Fig. 7A). *Hydra* WIP12 possesses both Atg16- and PI3P-binding motifs, which are necessary for its function (Fig. 7B, Fig. S15). To silence *WIP12* that is ubiquitously expressed (Fig. S16B,C), we repeatedly electroporated *Hv_Basel* polyps with siRNAs and recorded an 80% reduction in *WIP12* transcript level after 6 days of electroporation (EP6) (Fig. 7C). At the phenotypic level, we noted in *WIP12*(RNAi) animals a decrease in size and an apical disorganization after EP7 (Fig. 7D) together with a high mortality rate recorded after 2 weeks (Fig. 7E). All control animals bisected after EP6 survived the amputation and regenerated their head within 5 days, whereas *WIP12*(RNAi) animals exhibited a high mortality rate shortly after amputation (50–70%) and about 30% of survivors did not regenerate their head within 2 weeks (Fig. 7E).

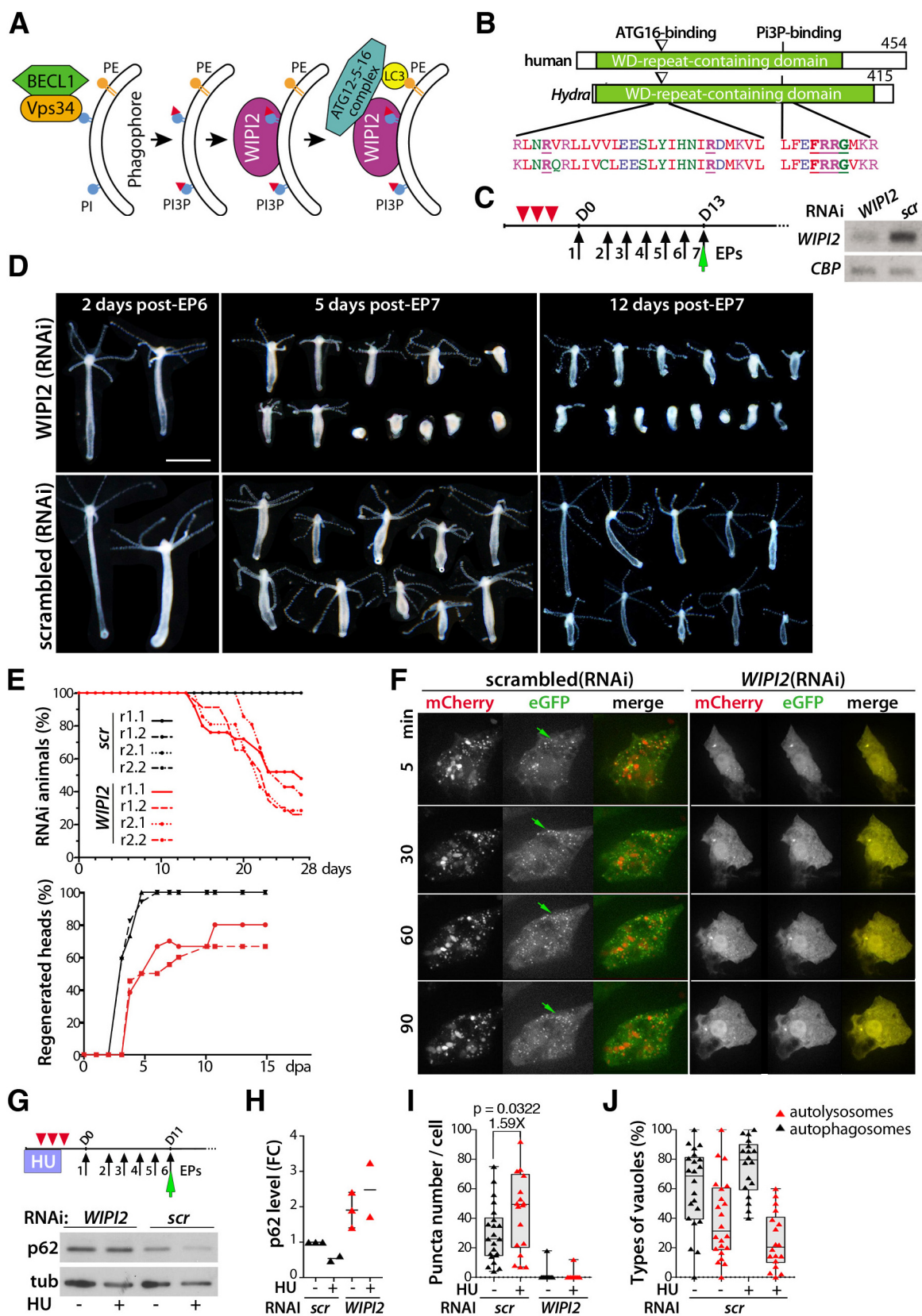


Fig. 7. See next page for legend.

The *in vivo* LC3 pattern in epithelial cells of *WIPI2*(RNAi) animals was diffuse and cytoplasmic, similar to that observed in *Ho_CS* epithelial cells (Fig. 7F). Also, the p62 level was twice as

high (Fig. 7G,H) and the number of LC3 puncta dramatically decreased (Fig. 7I). These results indicate that a partial but sustained silencing of *WIPI2* suffices to block autophagy as evidenced by the

Fig. 7. Deficient autophagy flux upon *WIPI2* silencing in *H. vulgaris*.

(A) Scheme showing the role of *WIPI2* in autophagosome formation (adapted from Dooley et al., 2014). (B) Structure of the human and *Hydra* *WIPI2* proteins and alignment of the regions involved in ATG12-5-16 complex or PI3P binding. (C) Left: RNAi procedure used to knock down *WIPI2* expression in intact animals. Red arrowheads indicate feedings preceding siRNAi delivery, black arrows indicate siRNA electroporation (EP), green arrow indicates co-electroporation of the mCherry-eGFP-hyLC3 autophagy sensor on EP7. Right: *WIPI2* and *CBP* (CREB-binding protein) RNA levels measured by RT-PCR in animals exposed to *WIPI2* or scrambled (scr) siRNAs. D, day. (D) Phenotypic analysis of *WIPI2*(RNAi) and *scr*(RNAi) animals post-EP6 or -EP7. Scale bar: 1 mm. Note that all images have been cut and aligned on black background for ease of comparison. (E) Mortality rates recorded after EP7 and head regeneration efficiency in animals bisected at mid-gastric level 24 h after EP6. (F) Live detection of LC3 vacuoles in epithelial cells from *WIPI2*(RNAi) or *scr*(RNAi) animals 2 days post-EP7. MG132 added just before imaging. Green arrows indicate formation of GFP⁺ puncta in *scr*(RNAi) cells. (G-J) *WIPI2* silencing in HU-treated animals. (G) p62 and tubulin levels in *Hv* animals electroporated six times with *WIPI2*- or *scr*-siRNAs. (H) Fold change (FC) in p62 levels in animals exposed or not to HU and knocked down or not for *WIPI2*; each triangle represents a distinct experiment. (I,J) Imaris quantification of LC3 puncta (I), and autophagosomes and autolysosomes (J) in epithelial cells of *WIPI2*(RNAi) or *scr*(RNAi) animals expressing the autophagy sensor, imaged 2 days post-EP7. Vacuoles were quantified 3 h after MG132 exposure. For box and whisker plots, the box indicates the 25th to 75th percentile, the line shows the median and the whiskers indicate the smallest and the largest value. Points represent individual values. *P*-values calculated using the unpaired *t*-test.

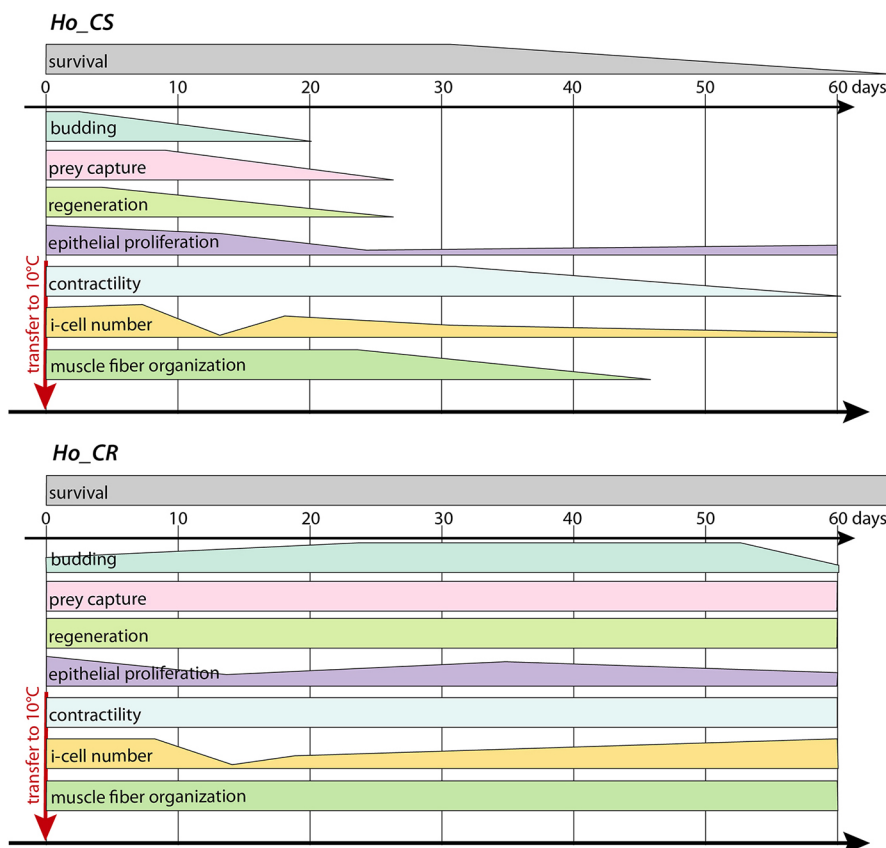
switch from a dotted to a diffuse LC3 pattern. This autophagy blockade in *Hv* animals leads to a syndrome resembling the aging phenotype observed in *Ho_CS* animals. Finally, we tested whether the epithelial response to the loss of i-cells does require a fully functional epithelial autophagy in *H. vulgaris*. To do so, we exposed *Hv* animals first to HU and then to *WIPI2* siRNAs (Fig. 7G). In

control RNAi animals, the HU treatment led to a decrease in p62 level (Fig. 7G,H), an increase in LC3 puncta (1.59×) together with a higher ratio of autophagosomes to autolysosomes (Fig. 7I,J), suggesting enhanced autophagosome formation. In *WIPI2*(RNAi) animals, HU treatment did not modify the higher p62 levels (Fig. 7G,H). These results indicate that the loss of i-cells tends to enhance epithelial autophagy in the non-aging *H. vulgaris*, but does not modify the autophagy partial blockade induced by *WIPI2* silencing.

DISCUSSION

The loss of interstitial stem cells triggers aging in the cold-sensitive strain of *H. oligactis*

To investigate aging in *Hydra*, we used two *H. oligactis* (*Ho*) strains, one named *Ho_CS* (cold sensitive) that rapidly develops an aging phenotype when undergoing gametogenesis upon cold exposure as previously shown (Yoshida et al., 2006), and another that resists aging, therefore named *Ho_CR* (cold resistant). The developmental properties that characterize *Hydra*, i.e. budding and regeneration, were already irreversibly altered by 20 days after transfer to cold in *Ho_CS* animals but not in *Ho_CR* ones (Fig. 8). In both strains, the loss of somatic interstitial cells was massive after 2 weeks when spermatogenesis is maximal, and were progressively rescued in *Ho_CR* but not in *Ho_CS*. We assume that the massive gametogenesis prevents stocks of somatic i-cells from being replenished. In aging *Ho_CS* animals, the rapid loss of interstitial cell lineages led to the loss of *de novo* neurogenesis (Tomczyk et al., 2019), which is responsible for the loss of the feeding response, loss of contractility and progressive starvation. Similarly, epithelial proliferation was reduced within the first 2-3 weeks, a reduction that was spontaneously reversible in *Ho_CR* but not in *Ho_CS*. This aging phenotype shares features with mammalian aging, such as

**Fig. 8. Comparative view of the timing of the different signs of aging recorded in *Ho_CS* and *Ho_CR* sexual animals.** The data linked to survival are shown in Fig. 1E and Fig. S1, budding in Fig. S1, prey capture in Fig. 1C and Fig. S1N, regeneration in Fig. 1F,G, i-cell loss in Fig. 2C,D, epithelial cell proliferation in Fig. 3D, and Fig. S4A, animal contractility in Fig. S1M, and muscle fiber organization in Fig. 3A-C.

deterioration of the muscular network, neurodegeneration and global loss of health (Brien, 1953; Yoshida et al., 2006; Tomczyk et al., 2019; this work).

Epithelial autophagy is required for maintaining epithelial self-renewal in *Hydra*

A previous study had proposed that the massive loss of interstitial stem cells is actually the driving force for aging in *Ho_CS* (Yoshida et al., 2006). Here, we focused on the epithelial properties in *Ho_CS* versus *Ho_CR* and we found that the starvation induced by the loss of the feeding response in *Ho_CS* animals is not followed by a sustained autophagy in epithelial cells as observed in *Ho_CR* or *Hv* animals. This deficient autophagy in *Ho_CS* appears to be constitutive as observed in all contexts, either homeostatic or after induction upon starvation, proteasome inhibition by MG132, autolysosome formation inhibition by bafilomycin or inhibition of the TORC1 complex by rapamycin. These modulators provide convergent results that all support an inefficient induction of autophagy in *Ho_CS* (Fig. 9). This conclusion relies on investigations performed at multiple levels: (1) histological and cytological with the analysis of LC3⁺ vacuoles, (2) molecular with the fluctuations of p62/SQSTM1 levels and the regulations of the autophagy genes as static indicators of the autophagy flux, and (3) live imaging with the dual autophagy sensor, used here in an intact adult organism. We propose a scenario in which slow aging in *Hydra* requires an epithelial adaptation to environmental challenges

through induction of an efficient autophagy that rescues epithelial cell cycling. Such a scenario is supported by: (1) the drop of epithelial self-renewal observed in animals that either undergo gametogenesis at 10°C or are exposed to HU at 18°C followed by an induction of the autophagy flux, which is efficient in *Ho_CR* but not in *Ho_CS* animals; (2) the rescue of epithelial cell cycling upon rapamycin-induced phagocytosis, which provides nutrients; and (3) the induction of aging in non-aging *Hv* animals upon blockade of autophagy through *WIP12* silencing (Fig. 9). Therefore, in *Hydra* an inducible autophagy flux appears to be essential to maintain epithelial stem cell renewal.

Compensatory autophagy induced by UPS blockade is deficient in *Ho_CS*

Autophagy has two main functions – to generate nutrients for the cell and to degrade altered intracellular proteins to maintain protein homeostasis (proteostasis), both functions being crucial for longevity (Cuervo, 2008; Morimoto and Cuervo, 2009). The maintenance of proteostasis relies on two main systems, the ubiquitin-proteasome system (UPS) and the lysosome-autophagosome, which are linked as autophagy can compensate the toxic effects of proteasome inhibition as shown in mammalian cells and *Drosophila* (Iwata et al., 2005; Ding et al., 2007; Pandey et al., 2007). To test the level of compensatory autophagy induced by UPS blockade in aging and non-aging *Hydra*, we used the proteasome inhibitor MG132 and we identified three distinct responses to UPS blockade (Fig. 9): in *Ho_CS* a rapid toxicity of MG132 and a lack of compensatory autophagy, with LC3 remaining mostly cytoplasmic; in *Ho_CR* a lower toxicity of MG132 and a moderate compensatory autophagy; in *H. vulgaris* a persisting fitness despite a prolonged exposure to MG132 and a high level of compensatory autophagy.

These responses reflect the expected correlation between the ability to enhance autophagy and the tolerance to proteasome inhibition and support the finding that autophagy is deficient in aging *Ho_CS*. In addition, the differences in MG132 tolerance between the *H. vulgaris* and *H. oligactis* species likely reflect a constitutive difference in proteostasis efficiency as previously reported (Gellner et al., 1992; Brennecke et al., 1998). The molecular chaperone Hsp70 is likely not similarly active in these two species, as *Hsp70* expression is upregulated in both species upon heat-shock but transcripts are unstable in *H. oligactis* and the Hsp70 protein not efficiently translated. At the evolutionary level, these results indicate that the link between autophagy and UPS is functional in non-bilateria species. Given the multiple mechanisms proposed to integrate these two pathways (Korolchuk et al., 2010; Lamark and Johansen, 2010), *Hydra* provides a useful framework to trace their respective origins.

In conclusion, this study shows that the loss of somatic interstitial cells, linked or not to gametogenesis, provides a condition that reveals the efficiency in epithelial autophagy but is not the main cause of aging. In fact, the deficiency in epithelial autophagy, which remains to be characterized at the molecular level, appears to be the primary cause of aging, leading to reduced epithelial proliferation, loss of regeneration and, ultimately, animal death. This mechanism could be tested in the non-aging *H. vulgaris*, in which blocking autophagosome formation suffices to shorten animal lifespan. This mechanism shares similarities with the role of autophagy in aging mammals, in which autophagy is crucial for the survival of stem cells (Boya et al., 2018), including hematopoietic stem cells (Warr et al., 2013; Gomez-Puerto et al., 2016) and muscle satellite cells (García-Prat et al., 2016). These findings point to autophagy as an evolutionarily conserved robust anti-aging mechanism that contributes to the preservation of adult stem cells.

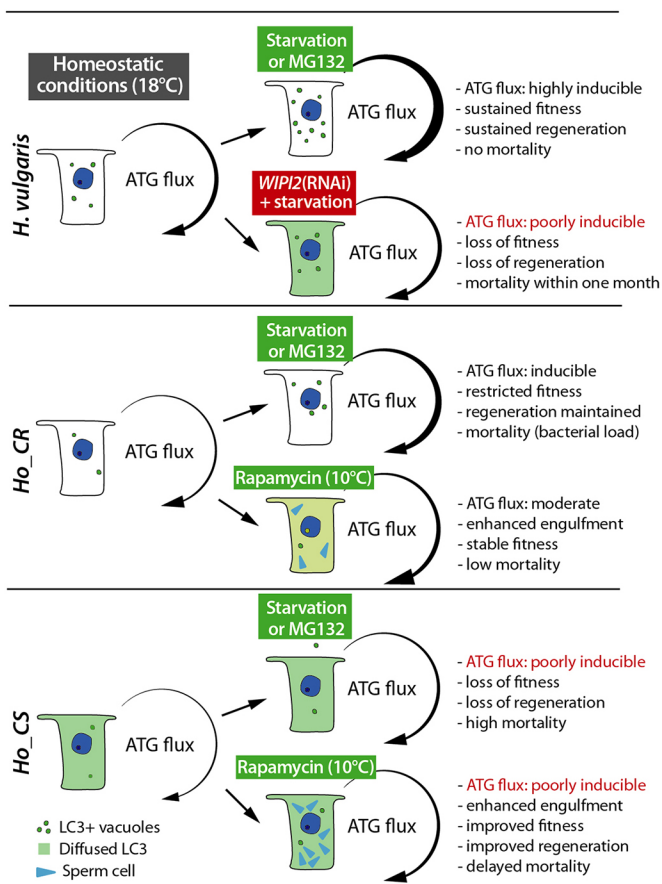


Fig. 9. The autophagic flux in epithelial cells of aging and non-aging *Hydra*. Inducibility of the autophagy flux upon starvation, MG132 or rapamycin treatments as deduced from the formation of LC3-positive vacuoles and puncta *in vivo*, or the accumulation of p62/SQSTM1. Thickness of curved arrows indicate the relative extent of ATG inducibility.

MATERIALS AND METHODS

Hydra strains, *Hydra* culture, monitoring of aging and behavioral analyses

Hydra vulgaris from the Basel or *sf-1* strains (*Hv_Basel*, *Hv_sf-1*) and two *Hydra oligactis* (*Ho*) strains, cold-sensitive (*Ho_CS*), cold-resistant (*Ho_CR*), were mass cultured at 18°C±0.5°C in Hydra Medium (HM; 1 mM NaCl, 1 mM CaCl₂, 0.1 mM KCl, 0.1 mM MgSO₄, 1 mM Tris-HCl pH 7.6). Animals were fed three to four times a week with freshly hatched brine shrimps (*Artemia*; Watson Aquaculture). To induce gametogenesis, *Ho_CS* and *Ho_CR* animals were transferred to 10°C±0.3°C and then fed twice a week. To monitor aging six sets of ten animals per condition placed in six-well plates (Greiner Bio-One) were observed five to seven times a week at the stereomicroscope and imaged at least once a week. Budding animals were counted daily and detached buds were removed. The reversibility of aging was tested on cohorts of 20 animals. For touch responsiveness, animals were stimulated with tweezers in the peduncle region and observed under the binocular microscope. For testing prey ingestion, animals were observed at the stereomicroscope 1 h after feeding and counted as positive when at least one *Artemia* was found in the gastric cavity.

Drug treatments and regeneration experiments

To deplete cycling cells at 18°C, cohorts of 20 animals were exposed to N-hydroxyurea (HU, Applichem, 5 mM diluted in HM) as indicated in Fig. 2E. The post-HU antibiotic treatment was given as an antibiotic mix containing ampicillin, rifampicin, streptomycin and neomycin (50 mg/ml each) as reported previously (Wein et al., 2018). This treatment was given continuously from day 2 after HU release and changed every other day. Untreated animals were kept in HM containing 0.01% DMSO during the same period. For rapamycin treatment, animals were continuously exposed to rapamycin (LC Laboratories, 0.8 µM diluted in HM) from 3 dpt to 10°C, the drug being changed three times a week. To inhibit proteasomal degradation, animals were treated with the proteasome inhibitor MG132 (SelleckChem, 5 µM diluted in HM, DMSO 0.05%) either for 16 h, or over a 5-day period at the indicated concentrations. To test the effect of these drugs on head regeneration, two sets of 15 animals per condition fed twice a week prior to bisection were starved for 2 days, bisected at the mid-gastric position and monitored over 13–15 days. For bafilomycin A (Enzo Life Sciences) treatment, animals were exposed to 50, 100 or 200 nM solution for 16 h diluted in HM, DMSO 0.01%.

mRNA *in situ* hybridization and phalloidin staining on whole mounts

For mRNA whole-mount *in situ* hybridization (WM-ISH) 2-day starved animals were relaxed for 60 s in 2% urethane, fixed overnight at 4°C in 4% paraformaldehyde (PFA) prepared in HM pH 7.5 (PFA-HM) and stored in methanol at –20°C. Transcripts were then detected with specific riboprobes as described by Bode et al. (2008). To visualize actin fibers, animals were starved for at least 24 h, washed in HM, relaxed for 60 s in 2% urethane, fixed for 4 h in PFA-HM, permeabilized in 0.1% Triton X-100 in PBS (PBS-TX) for 15 min, stained for 1 h in phalloidin-Alexa Fluor 546 1:100 (Invitrogen), washed in PBS, DAPI-stained (0.2 µg/ml) for 30 min, washed in PBS, washed briefly in water, mounted in Mowiol and imaged using Zeiss LSM700 or Leica SP8 confocal microscopes.

Histological sections and transmission electronic microscopy (TEM)

Animals were fixed in Fixative-1 [2% glutaraldehyde, 4% formaldehyde, 0.1 M 2AsO₂Na (pH 7.4), 2 mM CaCl₂, 150 mM sucrose] for 30 min at room temperature (RT), then overnight at 4°C, then washed three times in pre-cooled 0.1 M sodium cacodylate, transferred to Fixative-2 [1% OsO₄, 0.8% K₃Fe(CN)₆, 0.1 M 2AsO₂Na (pH 7.4)] for 60 min on ice, then washed three times in 0.1 M 2AsO₂Na, five times in H₂O and stained in 1% uranyl acetate for 90 min in the dark. After stepwise ethanol dehydration, samples were washed three times in 100% C₃H₆O, incubated overnight in 1:1 propylene oxide Epon resin solution (25.7 ml Agar 100 resin, 9.3 ml dodecenylsuccinic anhydride, 16.5 ml NMA, 1.6 ml BDMA from Agar Scientific), then three times for 120 min each in fresh 100% Epon

embedding medium, transferred into embedding molds and cured for 48 h at 60°C. Resin blocks were cut with a Leica UCT ultramicrotome, 70 nm ultrathin sections were transferred onto 100-mesh copper grids, stained for 5 min in 2% uranyl acetate (in 1:1 water-acetone), for 10 min in lead citrate (25 mg/ml in H₂O), observed with a Tecnai G2 transmission electron microscope at 120 kV accelerating voltage and imaged with a Tietz TemCam F214 CCD camera. For histological analysis, sections were dried on a glass slide, covered with a puddle of Toluidine Blue solution (1% Toluidine Blue, 1% sodium borate in water) and heated on a hot plate (70°C) for 30–120 s, or until the puddle steams. Excess stain was gently washed off with distilled water, and slides were dried and mounted in Mowiol.

Hydra p62/SQSTM1 antibody production and immunodetection on macerated tissues

A mouse polyclonal antibody was raised against *Hydra* p62/SQSTM1 by Delphi Genetics (Charleroi, Belgium) against the C-terminal stretch KES-KLERSLRQMEAMGFDNEGGWLRQLLISKDCSIDKVLDALSPAK (for validation of this antibody see Fig. 5B and Fig. S13D). The corresponding DNA sequence was synthesized following the mammalian codon usage, then inserted into the pStabyBoost expression vector and electroporated *in vivo* into mouse muscle. Sera were collected from five mice after three immunizations. For immunodetection, three to seven animals per condition were macerated as described by David (1973), cells were then spread on Superfrost Plus slides (Thermo Scientific), dried for 2 days at RT, washed in PBS, blocked in BSA-TX (bovine serum albumin 2%, Triton X-100 0.1%) for 2 h, incubated overnight at 4°C with the following antibodies: anti-ubiquitin (1:200, FK2 antibody, BML-PW0755-0025, Enzo Life Sciences), anti-LC3B (1:300, Novus Biologicals, nb100-2220, raised against the 1–100 N-terminus human LC3B), anti-*Hydra* p62/SQSTM1 (1:200), anti-tubulin (1:300, T5168, Sigma-Aldrich) (see Table S6). Slides were then washed in PBST [PBS (pH 7.2), Tween-20 0.1%] incubated in anti-rabbit Alexa Fluor 488 and/or anti-mouse Alexa Fluor 555 antibodies (1:600, Invitrogen, A-21206 and A31570), counterstained with DAPI and MitoFluor Red589 (1:5000, Life Technologies) and imaged as above. Autophagic vacuoles were counted in 100–300 cells per condition.

BrdU labeling and immunodetection on macerated tissues

30 polyps per condition were exposed to BrdU (5 mM in HM, Sigma-Aldrich) for 96 h or as indicated. After BrdU exposure, animals were washed in HM and the body columns of three sets of three animals per condition were dissected, macerated as independent triplicates, immunodetected with the BrdU Labeling and Detection Kit-I (Roche) and DAPI counterstained. Samples were imaged using a Leica D5550 fluorescence microscope, and at least 300 epithelial cells were counted on each replicate to calculate the BrdU-labeling index. The same slides were used to count the interstitial to epithelial stem cell ratio (ISCs/ESCs). For sexual animals, only those bearing at least four testes were selected.

In vivo detection of the autophagy flux with the mCherry-GFP-LC3A/B autophagy sensor

The mCherry and eGFP sequences were codon optimized for expression in *Hydra* (GenScript) and inserted into the hoTG vector after removal of the original GFP sequence (Wittlieb et al., 2006). The hoTG vector contains 1386 bp of the *Hydra* Actin promoter and a 677 bp-long terminator from the *Hydra* Actin gene. The *Hydra* LC3A/B sequence was amplified from *Ho_CS* cDNA and inserted into the pGEM-T vector. Coding sequences of mCherry, eGFP and hyLC3A/B were amplified from the hoTG_mCherry, hoTG_eGFP and pGEM-T_hyLC3A/B plasmids, respectively, and inserted in-frame into the hoTG vector following the Gibson method (Gibson et al., 2009). See Table S4 for primer sequences. To monitor the autophagy flux, 20 regularly fed animals were electroporated 8 h after feeding with a GenePulserXcell (Bio-Rad) delivering two pulses of 150 V at 1-s intervals, 50 ms each as described by Watanabe et al. (2014). Animals were immediately transferred from the electroporation cuvettes to six-well dishes in HM for recovery. Forty hours later, animals displaying fluorescent cells in the gastric region were relaxed in dishes containing 1% urethane HM. Unless otherwise specified, animals were incubated in

MG132 (5 μ M) for 3 h before live imaging was performed with a 3i spinning disc confocal microscope with laser power 75, exposure time 100 ms for *Hv* and *Ho_CR* animals; laser power 50, exposure time 50 ms for *Ho_CS* animals; camera intensification 250 in all conditions.

Whole cell extracts (WCE) and western analyses

WCE were prepared from 20–100 polyps starved for 2 days, washed in HM, resuspended in lysis buffer [SDS 2%, Tris-HCl pH 8.0 100 mM containing a mix of protease (Roche complete cocktail) and phosphatase inhibitors (Biotools cocktail or lab-made cocktail: 8 mM NaF, 20 mM β -glycerophosphate, 10 mM Na_3VO_4 , 0.1 mg/ml PMSF)] and passed through a 0.6 \times 30 mm syringe needle, yielding 100–500 μ g proteins per sample. For each condition, 10–30 μ g WCE were loaded on a 12% Rotiphorese Gel 30 (Roth), transferred to Hybond-P membrane (GE Healthcare) and detected with the antibodies raised against LC3B (1:1000, Novus Biologicals, nb100-2220), *Hydra* p62/SQSTM1 (1:1000, lab-made), ubiquitin (1:2000, Abcam, ab137025) and α -tubulin (1:2000, Sigma-Aldrich, T5293).

RNA interference (RNAi) procedure

RNAi was performed by electroporating siRNAs as previously reported (Watanabe et al., 2014) with minor modifications. Briefly, 30 animals were electroporated as above either with a ‘scrambled’ siRNA (4 μ M, diluted in water) used as control, or with a mixture of three siRNAs (Eurofins Genomics) targeted against *p62/SQSTM1* or *WIP1* (final concentration 4 μ M in water, see Table S5 for sequences). The procedure was repeated every other day as indicated.

Transcriptomic analyses

RNAs were extracted from pools of 20 *Hydra* using the RNeasy kit (Qiagen) (see Fig. S2A for conditions). Libraries were prepared with the Low Sample TruSeq total RNA preparation protocol using 15 PCR cycles. Library concentrations were measured with a Q-bit (Life Technologies). Pools of seven multiplexed libraries were loaded on a HiSeq 2000 sequencer (Illumina) and single-end sequenced using the standard 100 bp protocol. On average, 28 mio reads (3 mio s.d.) were obtained and cleaned for remaining adapters using cutadapt v1.9.1 (Martin, 2011). Assemblies were done separately for *Ho_CR* and *Ho_CS*, using Trinity v2.2.0 (Grabherr et al., 2011) with the *in silico* normalization option. These contigs were translated into protein sequences, keeping the longest open reading frame (ORF) per contig and excluding all proteins with ORFs <100 residues. Translated sequences were subjected to one round of clustering using Cd-hit (Li and Godzik, 2006) with options $-c1$ and $-s1$, which remove strictly identical protein coding sequences. After this step, for *Ho_CR* there remained 44,490 sequences and 24,590 Trinity ‘genes’, and for *Ho_CS* 45,002 sequences and 23,128 Trinity ‘genes’. Reads were cleaned with cutadapt (see above) and abundances were estimated by using Salmon (Patro and Kingsford, 2015). Quantification outputs were extracted, summarized and normalized using tximport and DESeq2 as described by Sonesson et al. (2016). These normalized counts per gene were used to produce heat maps and plots. For heat map representations, each value corresponds to the median number of reads obtained at given 10°C time points divided by the number of reads measured at the corresponding time point at 18°C, except for the day 35 10°C time point, which was normalized using the day 32 18°C value. After log₂ transformation, data were standardized by strain using time points from day 7 to day 35. Orthologies between *Ho_CR* and *Ho_CS* transcripts/genes were assigned manually. Sequences and RNA-seq profiles are available at https://hydratlas.unige.ch/blast/datasets/normacounts_CR2017.csv.gz and https://hydratlas.unige.ch/blast/datasets/normacounts_CS2017.csv.gz.

Proteomic analyses

The dimethyl stable isotope labeling protocol (Boersema et al., 2008, 2009) was used to quantify relative protein levels in *Ho_CS* polyps maintained either at 18°C (control), or at 10°C for 35 days (aging), or at 10°C for aging but exposed to rapamycin (rapamycin aging). For each condition, 10 μ g WCE were digested by filter-aided sample preparation (FASP) (Wiśniewski et al., 2009) with minor modifications. Dithiothreitol (DTT) was replaced by Tris(2-carboxyethyl)phosphine (TCEP) as reducing agent and

iodoacetamide by chloroacetamide as alkylating agent. Proteolytic digestion was first performed with Endoproteinase Lys-C followed by a second trypsin digestion. Next, peptide samples were labeled on StageTips with isotopomeric tags as follows: control samples were labeled with light dimethyl reactants ($\text{CH}_2\text{O}+\text{NaBH}_3\text{CN}$), aging samples were labeled with medium dimethyl reactants ($\text{CD}_2\text{O}+\text{NaBH}_3\text{CN}$) and rapamycin aging samples were labeled with heavy dimethyl reactants ($^{13}\text{CD}_2\text{O}+\text{NaBD}_3\text{CN}$). Independently labeled peptide samples were subsequently mixed in equal (1:1:1) ratio and fractionated into six fractions by strong cation exchange (SCX) chromatography on StageTips (Kulak et al., 2014). For LC-MS/MS measurements, each SCX fraction was again separated by C18 Reverse Phase nano UPLC using a Dionex Ultimate 3000 RSLC system (Thermo Fisher Scientific) on line connected to an Orbitrap Elite Mass Spectrometer (Thermo Fisher Scientific). Samples were first trapped on a home-made capillary pre-column (Magic AQ C18; 3 μ m–200 Å; 2 cm \times 100 μ m ID), then separated on a C18 capillary column (Nikkoy Technos Co.; Magic AQ C18; 3 μ m–100 Å; 15 cm \times 75 μ m ID) using a gradient ranging from 99% of solvent A (2% acetonitrile and 0.1% formic acid) to 90% of solvent B (90% acetonitrile and 0.1% formic acid). The Source spray voltage was set at 1.6 kV, and capillary temperature at 250°C. Acquisitions were performed using a Data-Dependent mode; the 20 most intense parent ions were selected for subsequent fragmentation by collision induced dissociation (CID) into the Linear Ion Trap and then excluded for the following 40 s. Orbitrap MS survey scan (m/z 300–1800) resolution was set to 120,000 (at 400 m/z) and fragments were recorded with low-resolution Rapid mode on the Trap. Filling times were set as follows: MS mode, 200 ms with a limit of 1×10^6 ions and MS² mode, 50 ms with a limit of 5×10^3 ions. Only multiply charged ions were allowed for fragmentation when reaching a threshold of 1000 counts, and during fragmentation an activation Q value of 0.25 was used and the normalized collision energy was set at 35% for 10 ms. For protein identification, quantification and bioinformatics, data were processed using MaxQuant software (Cox and Mann, 2008) (v1.5.1.2) as described by Chopra et al. (2014). MS/MS spectra were searched against the conceptually translated *de novo* transcriptome protein database described above. Statistical processing and outputs displays were performed using the embedded MaxQuant tool Perseus (Cox and Mann, 2012) and home-made programs written in R.

Statistical analyses

There were no statistical or computational methods involved in the determination of the sample size. The sample size, when applicable, is indicated in the figure legend or Materials and Methods section. Biological replicates come from fully independent experiments performed on different days. Technical replicates are a series of samples of a given experiment, all samples collected the same day (usually three or four). The number of replicates is indicated in the Materials and Methods section. As a general rule, we tried to perform at least three independent experiments. We did not exclude any data from the analyses. When applicable, the statistical methods we used are described in the Materials and Methods section or in the figure legends. For most results, raw data from the replicates are plotted directly in the figure. For the plots shown in Figs 2A,B, 4D–F,K,L, 6E and 7I,J, average values with s.d. are shown; for the plots shown in Figs 2H,I and 6B, average values with s.e.m. values are represented. The raw data for Fig. 2I and Fig. 6B are shown in Table S7 and Table S8, respectively.

Acknowledgements

The authors thank H. Shimizu (NIG Mishima, Japan) who provided animals of the *Ho_CS* strain; D. Chiappe and R. Hamelin from the Proteomics Core Facility at EPFL; C. Perruchoud, M.-L. Curchod and D. Benoni, for excellent technical support; A.-M. Cuervo, R. Loewith and T. Soldati for discussions and useful advice; and R. Loewith, T. Lamark and M. Vogg for helpful comments on the manuscript.

Competing interests

The authors declare no competing or financial interests.

Author contributions

Conceptualization: B.G., S.T., N.S.; Methodology: B.G., S.T., N.S., Y.W., W.B.; Software: S.T., Y.W., W.B.; Validation: B.G., S.T., N.S., Y.W., K.E., W.B., C.B., K.F.; Formal analysis: S.T., N.S.; Investigation: S.T., N.S., Q.S., K.E., W.B., C.B., K.F.; Resources: S.T., N.S., Y.W., W.B., C.B., K.F.; Data curation: B.G., S.T.; Writing -

original draft: B.G., S.T., N.S., Q.S., Y.W.; Writing - review & editing: B.G.; Visualization: B.G., S.A.; Supervision: B.G.; Project administration: B.G., S.A.; Funding acquisition: B.G., S.A.

Funding

This research was supported by the National Institutes of Health (R01AG037962 to S.A. and B.G.), the Swiss National Science Foundation (Schweizerischer Nationalfonds zur Förderung der Wissenschaftlichen Forschung; 31003A_149630, 31003_169930 to B.G.), the Canton de Genève (B.G.), and the Claraz Donation (B.G.). Deposited in PMC for immediate release.

Data availability

All raw RNA-seq data shown in Figs S2, S4, S5, S7, S8, S10, S11, S12, S13, S15, S16, and Tables S1, S2 and S3 have been deposited on the HydrATLAS server: https://hydratlas.unige.ch/blast/datasets/normacounts_CR2017.csv.gz and https://hydratlas.unige.ch/blast/datasets/normacounts_CS2017.csv.gz. All proteomic data shown in Fig. S14 have been deposited on the HydrATLAS server: https://hydratlas.unige.ch/blast/datasets/SignificanceB_proteinGroups_eLife.csv and https://hydratlas.unige.ch/blast/datasets/SignificanceB_proteinGroups_raw_data.csv.

Supplementary information

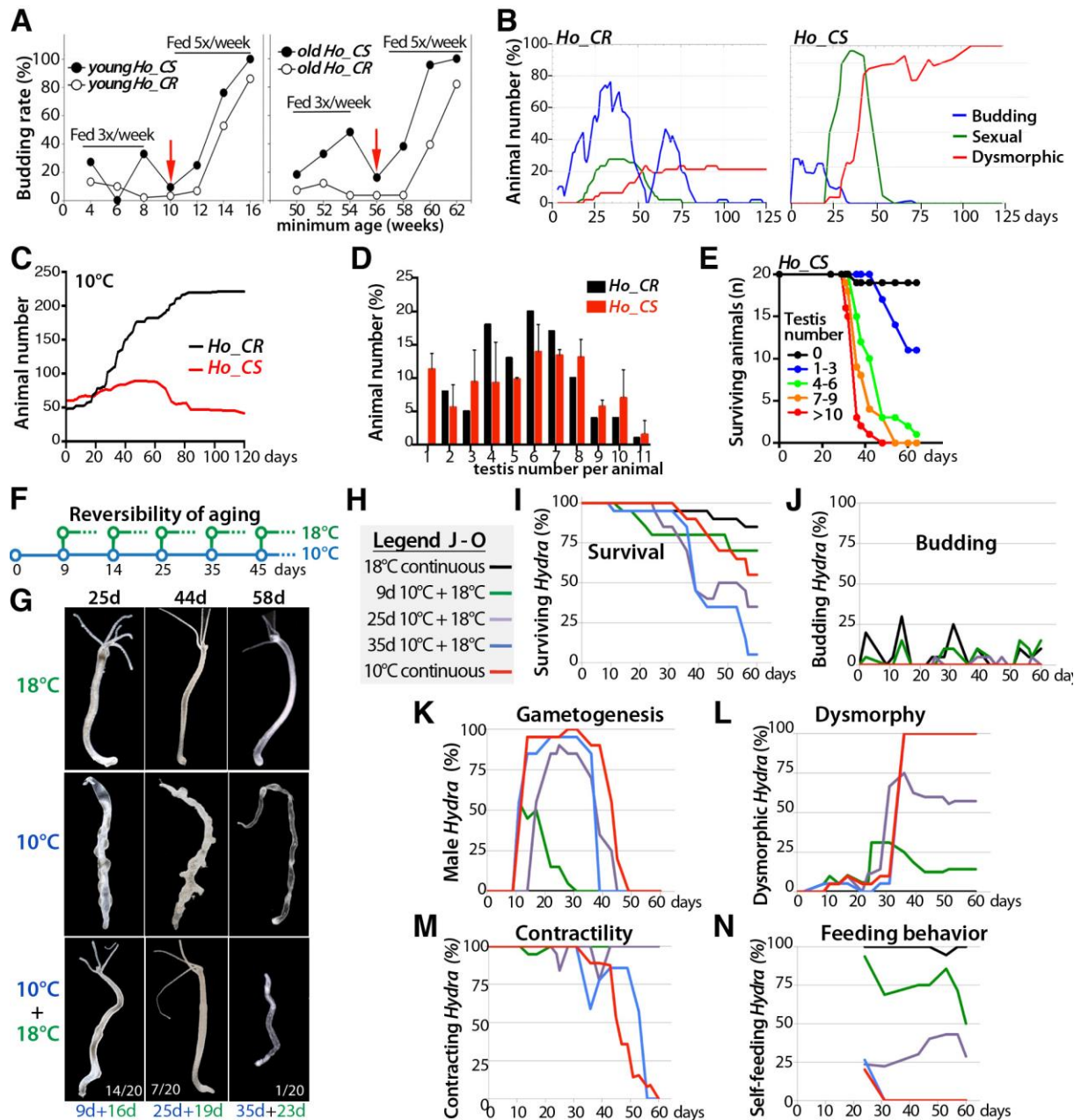
Supplementary information available online at <http://dev.biologists.org/lookup/doi/10.1242/dev.177840.supplemental>

References

- Austad, S. N. (2009). Is there a role for new invertebrate models for aging research? *J. Gerontol. A Biol. Sci. Med. Sci.* **64A**, 192–194. doi:10.1093/gerona/gln059
- Birgisdottir, A. B., Lamark, T. and Johansen, T. (2013). The LIR motif - crucial for selective autophagy. *J. Cell Sci.* **126**, 3237–3247.
- Bjedov, I., Toivonen, J. M., Kerr, F., Slack, C., Jacobson, J., Foley, A. and Partridge, L. (2010). Mechanisms of life span extension by rapamycin in the fruit fly *Drosophila melanogaster*. *Cell Metab.* **11**, 35–46. doi:10.1016/j.cmet.2009.11.010
- Bjørkøy, G., Lamark, T., Brech, A., Outzen, H., Perander, M., Øvervatn, A., Stenmark, H. and Johansen, T. (2005). p62/SQSTM1 forms protein aggregates degraded by autophagy and has a protective effect on huntingtin-induced cell death. *J. Cell Biol.* **171**, 603–614. doi:10.1083/jcb.200507002
- Bode, H., Lengfeld, T., Hobmayer, B. and Holstein, T. W. (2008). Detection of expression patterns in Hydra pattern formation. *Methods Mol. Biol.* **469**, 69–84. doi:10.1007/978-1-60327-469-2_7
- Boersema, P. J., Aye, T. T., van Veen, T. A. B., Heck, A. J. R. and Mohammed, S. (2008). Triplex protein quantification based on stable isotope labeling by peptide dimethylation applied to cell and tissue lysates. *Proteomics* **8**, 4624–4632. doi:10.1002/pmic.200800297
- Boersema, P. J., Raijmakers, R., Lemeer, S., Mohammed, S. and Heck, A. J. R. (2009). Multiplex peptide stable isotope dimethyl labeling for quantitative proteomics. *Nat. Protoc.* **4**, 484–494. doi:10.1038/nprot.2009.21
- Boya, P., Codogno, P. and Rodríguez-Muela, N. (2018). Autophagy in stem cells: repair, remodelling and metabolic reprogramming. *Development* **145**, dev146506. doi:10.1242/dev.146506
- Brennecke, T., Gellner, K. and Bosch, T. C. G. (1998). The lack of a stress response in Hydra oligactis is due to reduced hsp70 mRNA stability. *Eur. J. Biochem.* **255**, 703–709. doi:10.1046/j.1432-1327.1998.2550703.x
- Brien, P. (1953). La pérennité somatique. *Biol. Rev.* **28**, 308–349. doi:10.1111/j.1469-185X.1953.tb01381.x
- Buzgariu, W., Chera, S. and Galliot, B. (2008). Methods to investigate autophagy during starvation and regeneration in hydra. *Methods Enzymol.* **451**, 409–437. doi:10.1016/S0076-6879(08)03226-6
- Buzgariu, W., Crescenzi, M. and Galliot, B. (2014). Robust G2 pausing of adult stem cells in Hydra. *Differentiation* **87**, 83–99. doi:10.1016/j.diff.2014.03.001
- Chera, S., Buzgariu, W., Ghila, L. and Galliot, B. (2009). Autophagy in Hydra: a response to starvation and stress in early animal evolution. *Biochim. Biophys. Acta* **1793**, 1432–1443. doi:10.1016/j.bbamer.2009.03.010
- Chopra, T., Hamelin, R., Armand, F., Chiappe, D., Moniatte, M. and McKinney, J. D. (2014). Quantitative mass spectrometry reveals plasticity of metabolic networks in *Mycobacterium smegmatis*. *Mol. Cell. Proteomics* **13**, 3014–3028. doi:10.1074/mcp.M113.034082
- Cox, J. and Mann, M. (2008). MaxQuant enables high peptide identification rates, individualized p.p.b.-range mass accuracies and proteome-wide protein quantification. *Nat. Biotechnol.* **26**, 1367–1372. doi:10.1038/nbt.1511
- Cox, J. and Mann, M. (2012). 1D and 2D annotation enrichment: a statistical method integrating quantitative proteomics with complementary high-throughput data. *BMC Bioinformatics* **13** Suppl. 16, S12. doi:10.1186/1471-2105-13-S16-S12
- Cuervo, A. M. (2008). Autophagy and aging: keeping that old broom working. *Trends Genet.* **24**, 604–612. doi:10.1016/j.tig.2008.10.002
- David, C. N. (1973). A quantitative method for maceration of hydra tissue. *Roux' Arch. Dev. Biol.* **171**, 259–268. doi:10.1007/BF00577724
- Ding, W.-X., Ni, H.-M., Gao, W., Yoshimori, T., Stolz, D. B., Ron, D. and Yin, X.-M. (2007). Linking of autophagy to ubiquitin-proteasome system is important for the regulation of endoplasmic reticulum stress and cell viability. *Am. J. Pathol.* **171**, 513–524. doi:10.2353/ajpath.2007.070188
- Dooley, H. C., Razi, M., Polson, H. E. J., Girardin, S. E., Wilson, M. I. and Tooze, S. A. (2014). WIP1 links LC3 conjugation with PI3P, autophagosome formation, and pathogen clearance by recruiting Atg12-5-16L1. *Mol. Cell* **55**, 238–252. doi:10.1016/j.molcel.2014.05.021
- Finch, C. E. (1990). *Longevity, Senescence, and the Genome*. Chicago: University of Chicago Press.
- Fontana, L., Partridge, L. and Longo, V. D. (2010). Extending healthy life span – from yeast to humans. *Science* **328**, 321–326. doi:10.1126/science.1172539
- Fraune, S. and Bosch, T. C. G. (2007). Long-term maintenance of species-specific bacterial microbiota in the basal metazoan Hydra. *Proc. Natl. Acad. Sci. USA* **104**, 13146–13151. doi:10.1073/pnas.0703375104
- Füllgrabe, J., Ghislat, G., Cho, D.-H. and Rubinsztein, D. C. (2016). Transcriptional regulation of mammalian autophagy at a glance. *J. Cell Sci.* **129**, 3059–3066. doi:10.1242/jcs.188920
- Galliot, B. (2012). Hydra, a fruitful model system for 270 years. *Int. J. Dev. Biol.* **56**, 411–423. doi:10.1387/ijdb.120086bg
- García-Prat, L., Martínez-Vicente, M., Perdiguero, E., Ortet, L., Rodríguez-Ubreva, J., Rebollo, E., Ruiz-Bonilla, V., Gutarra, S., Ballestar, E., Serrano, A. L. et al. (2016). Autophagy maintains stemness by preventing senescence. *Nature* **529**, 37–42. doi:10.1038/nature16187
- Gellner, K., Praetzel, G. and Bosch, T. C. G. (1992). Cloning and expression of a heat-inducible hsp70 gene in two species of Hydra which differ in their stress response. *Eur. J. Biochem.* **210**, 683–691. doi:10.1111/j.1432-1033.1992.tb17469.x
- Gibson, D. G., Young, L., Chuang, R.-Y., Venter, J. C., Hutchison, C. A., III and Smith, H. O. (2009). Enzymatic assembly of DNA molecules up to several hundred kilobases. *Nat. Methods* **6**, 343–345. doi:10.1038/nmeth.1318
- Gomez-Puerto, M. C., Folkerts, H., Wierenga, A. T. J., Schepers, K., Schuringa, J. J., Coffier, P. J. and Vellenga, E. (2016). Autophagy proteins ATG5 and ATG7 are essential for the maintenance of human CD34⁺ hematopoietic stem-progenitor cells. *Stem Cells* **34**, 1651–1663. doi:10.1002/stem.2347
- Grabherr, M. G., Haas, B. J., Yassour, M., Levin, J. Z., Thompson, D. A., Amit, I., Adiconis, X., Fan, L., Raychowdhury, R., Zeng, Q. et al. (2011). Full-length transcriptome assembly from RNA-Seq data without a reference genome. *Nat. Biotechnol.* **29**, 644–652. doi:10.1038/nbt.1883
- Helfand, S. L. and Rogina, B. (2003). Genetics of aging in the fruit fly, *Drosophila melanogaster*. *Annu. Rev. Genet.* **37**, 329–348. doi:10.1146/annurev.genet.37.040103.095211
- Hobmayer, B., Jenewein, M., Eder, D., Eder, M.-K., Glasauer, S., Gufler, S., Hartl, M. and Salvenmoser, W. (2012). Stemness in Hydra - a current perspective. *Int. J. Dev. Biol.* **56**, 509–517. doi:10.1387/ijdb.113426bh
- Iwata, A., Riley, B. E., Johnston, J. A. and Kopito, R. R. (2005). HDAC6 and microtubules are required for autophagic degradation of aggregated huntingtin. *J. Biol. Chem.* **280**, 40282–40292. doi:10.1074/jbc.M508786200
- Johansen, T. and Lamark, T. (2011). Selective autophagy mediated by autophagy adapter proteins. *Autophagy* **7**, 279–296. doi:10.4161/auto.7.3.14487
- Kocaturk, N. M. and Gozuacik, D. (2018). Crosstalk between mammalian autophagy and the ubiquitin-proteasome system. *Front. Cell Dev. Biol.* **6**, 128. doi:10.3389/fcell.2018.00128
- Korolchuk, V. I., Menzies, F. M. and Rubinsztein, D. C. (2010). Mechanisms of cross-talk between the ubiquitin-proteasome and autophagy-lysosome systems. *FEBS Lett.* **584**, 1393–1398. doi:10.1016/j.febslet.2009.12.047
- Kortschak, R. D., Samuel, G., Saint, R. and Miller, D. J. (2003). EST analysis of the cnidarian *Acropora millepora* reveals extensive gene loss and rapid sequence divergence in the model invertebrates. *Curr. Biol.* **13**, 2190–2195. doi:10.1016/j.cub.2003.11.030
- Kulak, N. A., Pichler, G., Paron, I., Nagaraj, N. and Mann, M. (2014). Minimal, encapsulated proteomic-sample processing applied to copy-number estimation in eukaryotic cells. *Nat. Methods* **11**, 319–324. doi:10.1038/nmeth.2834
- Lamark, T. and Johansen, T. (2010). Autophagy: links with the proteasome. *Curr. Opin. Cell Biol.* **22**, 192–198. doi:10.1016/j.cob.2009.11.002
- Li, W. and Godzik, A. (2006). Cd-hit: a fast program for clustering and comparing large sets of protein or nucleotide sequences. *Bioinformatics* **22**, 1658–1659. doi:10.1093/bioinformatics/btl158
- Littlefield, C. L., Finkemeier, C. and Bode, H. R. (1991). Spermatogenesis in Hydra oligactis: II. How temperature controls the reciprocity of sexual and asexual reproduction. *Dev. Biol.* **146**, 292–300. doi:10.1016/0012-1606(91)90231-Q
- Longo, V. D. and Finch, C. E. (2003). Evolutionary medicine: from dwarf model systems to healthy centenarians? *Science* **299**, 1342–1346. doi:10.1126/science.1077991
- Marcum, B. A. and Campbell, R. D. (1978). Development of Hydra lacking nerve and interstitial cells. *J. Cell Sci.* **29**, 17–33.
- Martin, M. (2011). Cutadapt removes adapter sequences from high-throughput sequencing reads. *EMBnet journal* **17**, 10–12. doi:10.14806/ej.17.1.200
- Martínez, D. E. (1998). Mortality patterns suggest lack of senescence in hydra. *Exp. Gerontol.* **33**, 217–225. doi:10.1016/S0531-5565(97)00113-7

- Morimoto, R. I. and Cuervo, A. M. (2009). Protein homeostasis and aging: taking care of proteins from the cradle to the grave. *J. Gerontol. A Biol. Sci. Med. Sci.* **64A**, 167-170. doi:10.1093/gerona/gln071
- Olsen, A., Vantipalli, M. C. and Lithgow, G. J. (2006). Using *Caenorhabditis elegans* as a model for aging and age-related diseases. *Ann. N. Y. Acad. Sci.* **1067**, 120-128. doi:10.1196/annals.1354.015
- Pandey, U. B., Nie, Z., Batlevi, Y., McCray, B. A., Ritson, G. P., Nedelsky, N. B., Schwartz, S. L., DiProspero, N. A., Knight, M. A., Schuldiner, O. et al. (2007). HDAC6 rescues neurodegeneration and provides an essential link between autophagy and the UPS. *Nature* **447**, 860-864. doi:10.1038/nature05853
- Pankiv, S., Clausen, T. H., Lamark, T., Brech, A., Bruun, J.-A., Outzen, H., Øvervatn, A., Bjørkøy, G. and Johansen, T. (2007). p62/SQSTM1 binds directly to Atg8/LC3 to facilitate degradation of ubiquitinated protein aggregates by autophagy. *J. Biol. Chem.* **282**, 24131-24145. doi:10.1074/jbc.M702824200
- Patro, R. and Kingsford, C. (2015). Data-dependent bucketing improves reference-free compression of sequencing reads. *Bioinformatics* **31**, 2770-2777. doi:10.1093/bioinformatics/btv248
- Schaible, R., Scheuerlein, A., Daňko, M. J., Gampe, J., Martínez, D. E. and Vaupel, J. W. (2015). Constant mortality and fertility over age in *Hydra*. *Proc. Natl. Acad. Sci. USA* **112**, 15701-15706. doi:10.1073/pnas.1521002112
- Schenkelaars, Q., Tomczyk, S., Wenger, Y., Ekundayo, K., Girard, V., Buzgariu, W., Austad, S. and Galliot, B. (2018). *Hydra*, a model system for deciphering the mechanisms of aging and resistance to aging. In *Conn's Handbook For Models On Human Aging*, 2nd edn. (ed. P. M. Conn and J. Ram) pp. 507-520. Elsevier.
- Seibenhener, M. L., Babu, J. R., Geetha, T., Wong, H. C., Krishna, N. R., Wooten, M. W. (2004). Sequestosome1/p62 is a polyubiquitin chain binding protein involved in ubiquitin proteasome degradation. *Mol. Cell Biol.* **24**, 8055-8068. doi:10.1128/MCB.24.18.8055-8068.2004
- Shen, H.-M. and Mizushima, N. (2014). At the end of the autophagic road: an emerging understanding of lysosomal functions in autophagy. *Trends Biochem. Sci.* **39**, 61-71. doi:10.1016/j.tibs.2013.12.001
- Soneson, C., Love, M. I. and Robinson, M. D. (2016). Differential analyses for RNA-seq: transcript-level estimates improve gene-level inferences. *F1000 Res.* **4**, 1521. doi:10.12688/f1000research.7563.2
- Sugiyama, T. and Fujisawa, T. (1978). Genetic analysis of developmental mechanisms in *Hydra*. II. Isolation and characterization of an interstitial cell-deficient strain. *J. Cell Sci.* **29**, 35-52.
- Tomczyk, S., Fischer, K., Austad, S. and Galliot, B. (2015). *Hydra*, a powerful model for aging studies. *Invert. Reprod. Dev.* **59**, 11-16. doi:10.1080/07924259.2014.927805
- Tomczyk, S., Buzgariu, W., Perruchoud, C., Fisher, K., Austad, S. and Galliot, B. (2019). Loss of neurogenesis in aging *Hydra*. *Dev. Neurobiol.* **79**, 479-496. doi:10.1002/dneu.22676
- Valenzano, D. R., Aboobaker, A., Seluanov, A. and Gorbunova, V. (2017). Non-canonical aging model systems and why we need them. *EMBO J.* **36**, 959-963. doi:10.15252/embj.201796837
- Warr, M. R., Binnewies, M., Flach, J., Reynaud, D., Garg, T., Malhotra, R., Debnath, J. and Passequé, E. (2013). FOXO3A directs a protective autophagy program in haematopoietic stem cells. *Nature* **494**, 323-327. doi:10.1038/nature11895
- Watanabe, H., Schmidt, H. A., Kuhn, A., Höger, S. K., Kocagöz, Y., Laumann-Lipp, N., Özbek, S. and Holstein, T. W. (2014). Nodal signalling determines biradial asymmetry in *Hydra*. *Nature* **515**, 112-115. doi:10.1038/nature13666
- Wein, T., Dagan, T., Fraune, S., Bosch, T. C. G., Reusch, T. B. H. and Hülter, N. F. (2018). Carrying capacity and colonization dynamics of curvibacter in the *hydra* host habitat. *Front. Microbiol.* **9**, 443. doi:10.3389/fmicb.2018.00443
- Wenger, Y. and Galliot, B. (2013). Punctuated emergences of genetic and phenotypic innovations in eumetazoan, bilaterian, euteleostome, and hominidae ancestors. *Genome Biol. Evol.* **5**, 1949-1968. doi:10.1093/gbe/evt142
- Wenger, Y., Buzgariu, W. and Galliot, B. (2016). Loss of neurogenesis in *Hydra* leads to compensatory regulation of neurogenic and neurotransmission genes in epithelial cells. *Philos. Trans. R. Soc. Lond. B Biol. Sci.* **371**, 20150040. doi:10.1098/rstb.2015.0040
- Wiśniewski, J. R., Zougman, A., Nagaraj, N. and Mann, M. (2009). Universal sample preparation method for proteome analysis. *Nat. Methods* **6**, 359-362. doi:10.1038/nmeth.1322
- Wittlieb, J., Khalturin, K., Lohmann, J. U., Anton-Erxleben, F. and Bosch, T. C. G. (2006). Transgenic *Hydra* allow in vivo tracking of individual stem cells during morphogenesis. *Proc. Natl. Acad. Sci. USA* **103**, 6208-6211. doi:10.1073/pnas.0510163103
- Ylä-Anttila, P., Mikkonen, E., Happonen, K. E., Holland, P., Ueno, T., Simonsen, A. and Eskelinen, E.-L. (2015). RAB24 facilitates clearance of autophagic compartments during basal conditions. *Autophagy* **11**, 1833-1848. doi:10.1080/15548627.2015.1086522
- Yoshida, K., Fujisawa, T., Hwang, J. S., Ikeo, K. and Gojobori, T. (2006). Degeneration after sexual differentiation in *hydra* and its relevance to the evolution of aging. *Gene* **385**, 64-70. doi:10.1016/j.gene.2006.06.031
- Yu, L., Chen, Y. and Tooze, S. A. (2018). Autophagy pathway: cellular and molecular mechanisms. *Autophagy* **14**, 207-215. doi:10.1080/15548627.2017.1378838

SUPPLEMENTARY FIGURES

Figure S1: Features and reversibility of the cold-induced aging phenotype in *Ho_CS* animals

(A) Budding rate of juvenile (4 to 16 weeks old, left graph) and older (50 to 62 weeks old, right graph) *Ho_CS* and *Ho_CR* animals kept at 18°C and submitted to two successive feeding regimes. Red arrows indicate the transition from 3x to 5x feedings a week. In both cohorts the budding rate is up-regulated by a heavy diet, however older *Ho_CS* animals appear more prone to bud than *Ho_CR*. (B,C) Comparative analysis of two cohorts of *Ho_CR* (n=48) and *Ho_CS* (n=60) animals transferred to 10°C on day-0, showing in (B) the rates of budding (blue), sexual differentiation (green) and dysmorphic traits (red), and in (C) the population size kinetics. Buds produced at 10°C do not undergo aging. In the experiment depicted in (C), buds were not removed from the culture and thus included in the population size. The recorded dysmorphic features were duplicated head or foot regions, and arrested budding process in *Ho_CR*, tentacle shrinking, head loss, body column stenosis in *Ho_CS*. (D) Similar distribution of testis number in *Ho_CS* and *Ho_CR* cohorts maintained at 10°C for 25 days. Animals that did not develop testes were not included. (E) Survival of *Ho_CS* animals according to the number of testes they produce. (F) Scheme showing the procedure for testing the reversibility of aging. At day-0 seven *Ho_CS* cohorts (for each cohort n=20)

were separated from the 18°C main culture, one was maintained at 18°C (top line) whereas the others were transferred to 10°C. At each indicated time-point, one cohort was moved back to 18°C, while one cohort remained at 10°C throughout the experiment (blue bottom line). Animals were fed twice a week all through the experiment.

(G) Representative phenotypes of animals maintained either at 18°C (upper row) or at 10°C (middle row) or moved from 10°C to 18°C at day-9, day-25 or day-35 (lower row). The fraction of animals appearing healthy when returned from 10°C to 18°C is 70% (14/20), 35% (7/20) after 5% (1/20) respectively. After 35 days at 10°C, animals no longer recover, the single animal still alive 23 days after the switch back to 18°C died in the following days. Approximately 50% animals returned to 18°C at day-9 had shown first signs of sexual traits. Upon return to 18°C, testes of these animals stopped develop and resorbed. **(H-N)** Observed percentages of surviving (I), budding (J), sexually differentiating (K), dysmorphic (L), or touch-responsive (M) animals when maintained at 10°C over 60 days. All parameters were recorded five times a week except the feeding behavior (N) recorded only twice. For measuring the survival rate, buds produced during that period were removed from the culture soon after detachment, thus not included in the total animal number (I). The observed peaks of budding are caused by the feeding rhythm (twice a week, J). Contractibility was measured by stimulating briefly the peduncle region with tweezers and the percentage of animals contracting upon stimuli was recorded (M). The efficiency of the feeding behavior was assessed one hour after feeding as the percentage of animals with preys inside the gastric cavity (N). Animals able to catch preys with tentacles but unable to transfer it to the gastric cavity were excluded.

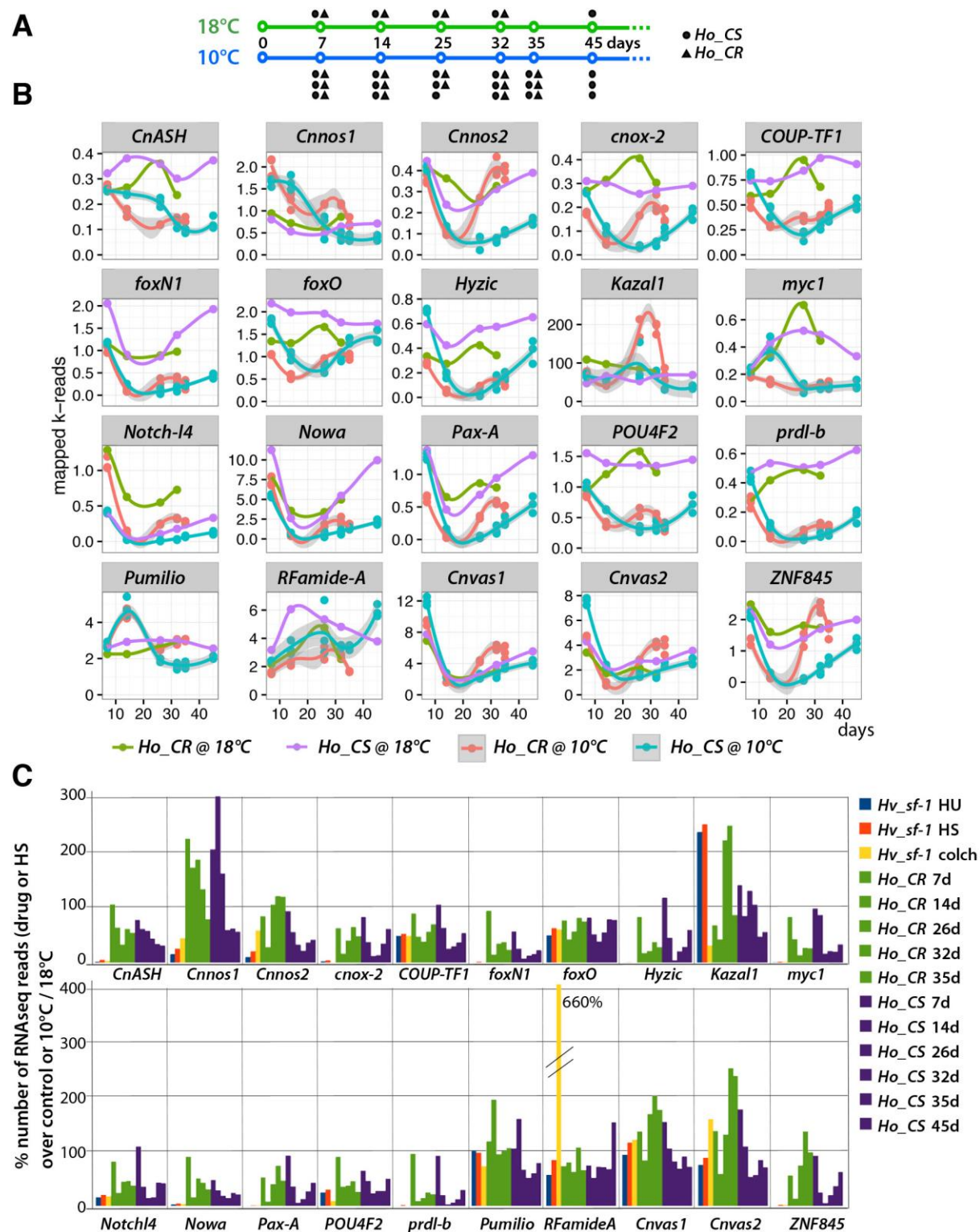


Figure S2: RNA-seq profiles of 20 genes expressed in interstitial cell lineages in *Ho_CS* and *Ho_CR* animals maintained at 18°C or transferred to 10°C.

(A) Scheme describing the procedure used for quantitative RNA-seq analysis of aging. RNA samples were collected at indicated time points from *Ho_CS* and *Ho_CR* animals either maintained as a unique cohort at 18°C or as three distinct parallel cohorts at 10°C. (B) Individual RNA-seq profiles of 20 evolutionarily-conserved genes predominantly expressed in the interstitial cell lineage in *H. vulgaris* as described in ref. (Wenger et al., 2016). See the access of the corresponding sequences in **Table-S1**. Note the drastic but transient down-regulation of most genes in *Ho_CR* and *Ho_CS* animals maintained at 10°C, highlighting the partial elimination followed by the recovery of the corresponding cell types. (C) Comparative RNA-seq analysis of i-cell gene expression in *Hv_sf-1* animals 10 days after exposure to HU (blue), heatshock (HS, red), colchicine (yellow), or in *Ho_CR* (green) and *Ho_CS* (purple) at various time points after transfer to 10°C. Values were normalized on values measured in untreated *Hv_sf-1* animals (blue, red, yellow and green values) or in *Ho* animals maintained at 18°C (purple). All data are available on HydrATLAS.unige.ch.

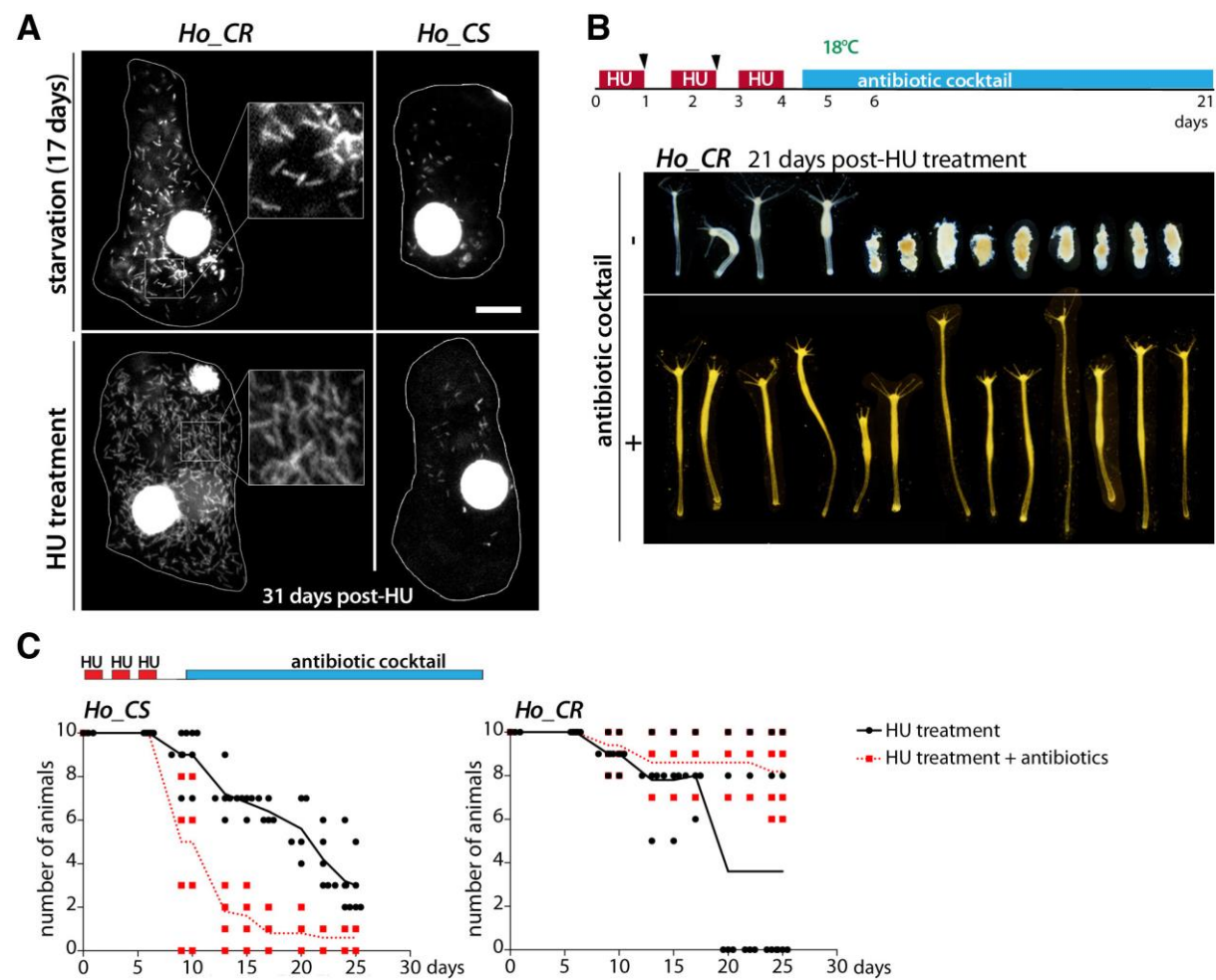


Figure S3: Distinct bacterial loads in *Ho_CR* and *Ho_CS* epithelial cells

(A) Abundance of commensal intra-epithelial bacteria in epithelial cells of *Ho_CS* and *Ho_CR* either starved for 17 days (upper row) or treated with HU as indicated in B and pictured 31 days later (lower row). Bacteria are visualized by DAPI staining. Scale bar: 10 μ m. (B) Animal morphologies of *Ho_CR* cohorts treated with HU and subsequently exposed or not to a cocktail of antibiotics. (C) Survival rate of 5 cohorts of 10 HU-treated animals exposed or not to a cocktail of antibiotics. The antibiotic treatment is toxic for *Ho_CS* animals while improving the survival rate of *Ho_CR* ones.

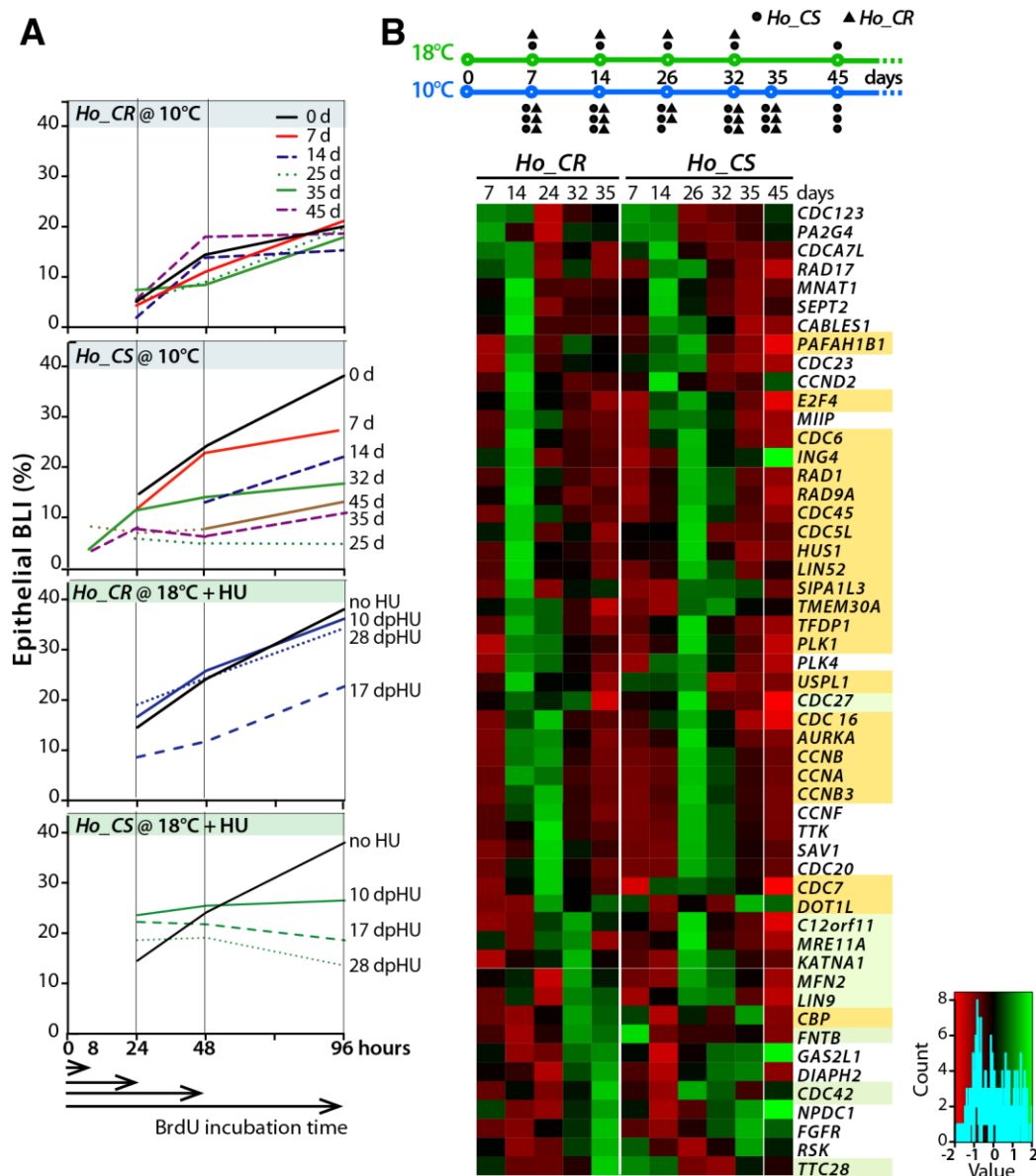


Figure S4: Comparative analysis of epithelial proliferation in *Ho_CS* and *Ho_CR* animals.

(A) Cycling activity of ESC in *Ho_CS* and *Ho_CR* animals transferred to 10°C (two upper graphs) or maintained at 18°C after HU treatment (two lower graphs). The BrdU-labeling index (BLI) was measured 7, 14, 25, 32, 45, 35 days (d) after transfer to 10°C, or 10, 17 or 28 days post-HU release (dpHU). For each time point, animals were exposed to BrdU for 24, 48 or 96 hours, then macerated for immunodetection. The fraction of BrdU-positive ESCs was counted to measure the linear progression of the cumulative eBLIs. The *Ho_CS* and *Ho_CR* cultures tested at 10°C were not fed at the same rhythm in the weeks preceding the transfer to 10°C, four times a week for *Ho_CS*, twice a week for *Ho_CR*, explaining the different eBLI values at day-0. This experiment was performed independently of the experiment shown in Figure 3D.

(B) Quantitative RNA-seq analysis of 52 *Hydra* genes orthologous to human genes annotated as involved in “cell cycle” or “cell proliferation” (www.uniprot.org, Table-S2). The experimental RNA-seq procedure is that described in Figure S2A. The heatmap shows relative fold changes defined as the ratio between the values measured at 10°C at a given time point over the value measured at 18°C at same or similar time point in *Ho_CR* and *Ho_CS* animals. Yellow and green backgrounds highlight genes whose modulations are delayed or advanced in *Ho_CS* compared to *Ho_CR* respectively. See the individual profile of each gene in Figure S5 and access to the corresponding sequences in Table S2.

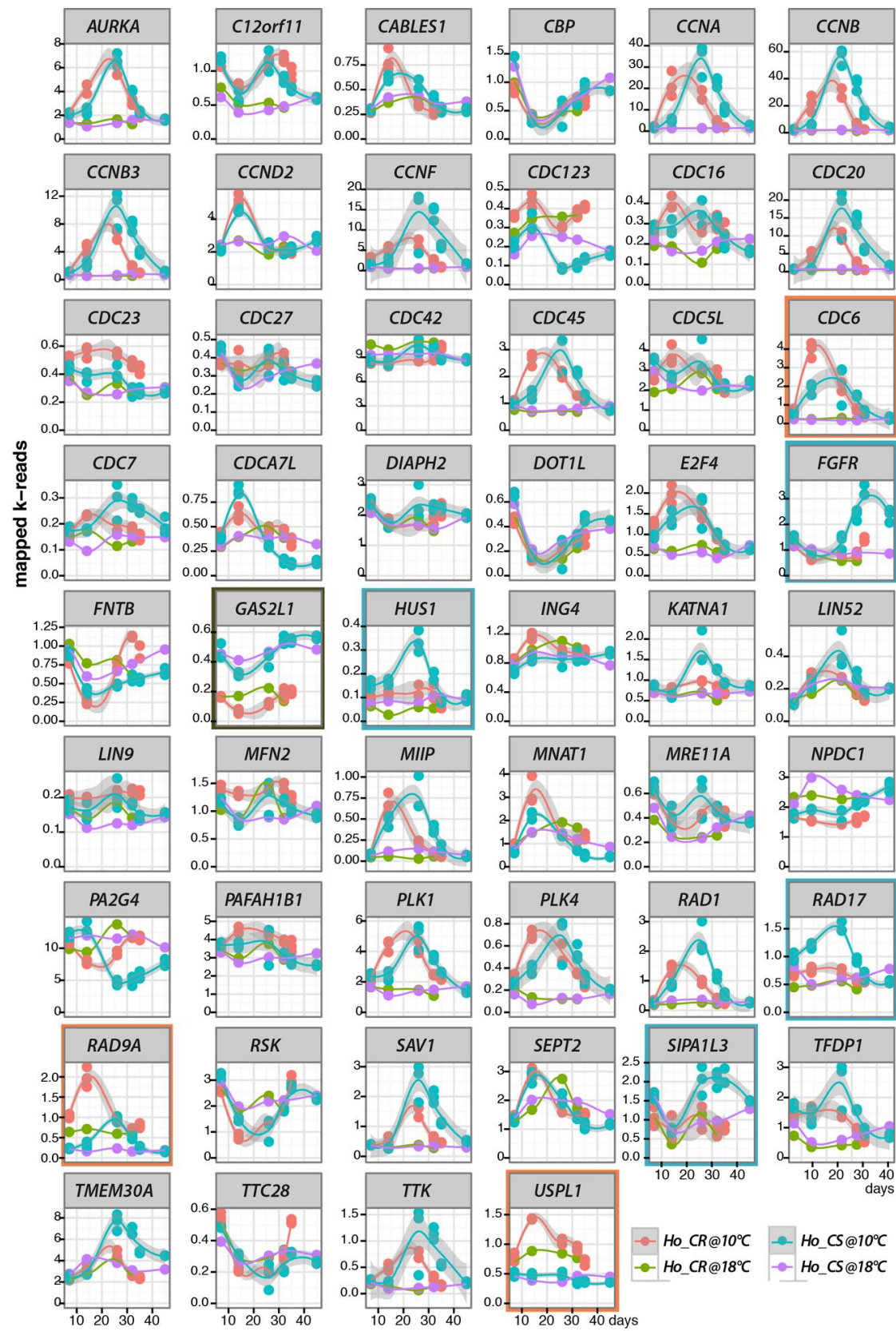


Figure S5: RNA-seq profiles of 52 *Hydra* orthologs to mammalian genes involved in cell cycle and/or cell proliferation

RNA-seq expression profiles of 52 cell cycle / cell proliferation genes tested in *Ho_CR* and *Ho_CS* animals maintained at 18°C or at 10°C as depicted in **Fig. S2A, S4B**. Note the delayed up-regulation of *CCNA*, *CCNB*, *CDC16*, *CDC45*, *MIIP*, *PLK1*, *PLK4*, *RAD1*, in *Ho_CS* when compared to *Ho_CR*. Orange frames indicate genes up-regulated in *Ho_CR* at 10°C at much higher level than in *Ho_CS* (*CDC6*, *MNAT1*, *RAD9A*, *USPL1*), blue frames indicate genes up-regulated in *Ho_CS* at 10°C at much higher level than in *Ho_CR* (*CCNF*, *CDC20*, *FGFR*, *HUS1*, *KATNA1*, *LIN52*, *RAD17*, *SAV1*, *SIPA1L3*, *TFDP1*, *TTK*), black frames indicate genes that exhibit a constitutively sustained up-regulation in *Ho_CS* when compared to *Ho_CR* (*GAS2L1*). Values on x axis = days, on y axis = mapped k-reads. For access to the corresponding sequences, see **Table S2**.

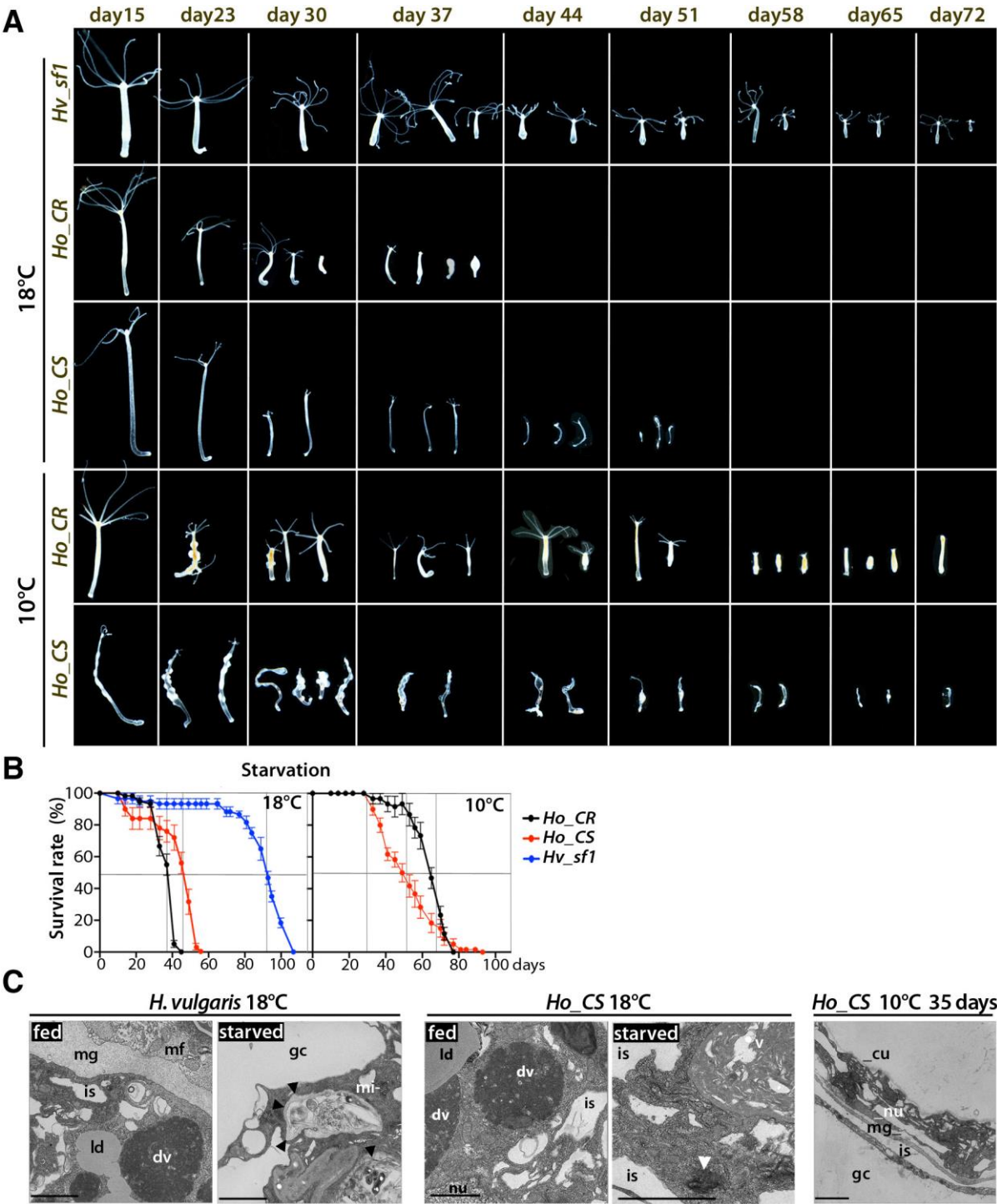


Figure S6: Starvation-induced phenotypes in *Ho_CR*, *Ho_CS* and *H. vulgaris* animals

(A, B) Morphological alterations (A) and survival rates (B) recorded in starved *Hv_sf1*, *Ho_CR*, *Ho_CS* animals maintained at 18°C or 10°C (for each condition n = 6x 10 animals). At 18°C *Ho_CR* animals die by day-40 without showing morphological alterations typical of aging, while *Ho_CS* animals commonly die later, by day-58, but exhibit aging-like morphological alterations from day-30. Note that *Hv_sf1* animals resist about 50 days longer to starvation than *Ho_CS* and *Ho_CR* animals. At 10°C, starved *Ho_CR* animals undergo spermatogenesis and maintain their physiological fitness up to day-51, while starved *Ho_CS* animals exhibit aging signs from day-15, similar to those observed in animals fed twice a week (see **Figure 1D**). The two *Ho* strains exhibit a similar resistance to starvation, enhanced in case of *Ho_CR* animals maintained at 10°C when compared to 18°C. (C) TEM views of body column sections from *Hv* (Basel strain) and *Ho_CS* animals either maintained at 18°C regularly fed or starved for 11 days, or maintained at 10°C for 35 days. Black arrowheads: autophagosome, white arrowhead: aggregate. Note the dramatically reduced gastrodermis after 35 days at 10°C in *Ho_CS* animals. Abbreviations: cu: cuticle, dv: digestive vacuole, gc: gastric cavity, is: intracellular space, ld: lipid droplets, mf: myofibril, mg: mesoglea, mi: mitochondria, nu: nucleus. Scale bars = 2 µm.

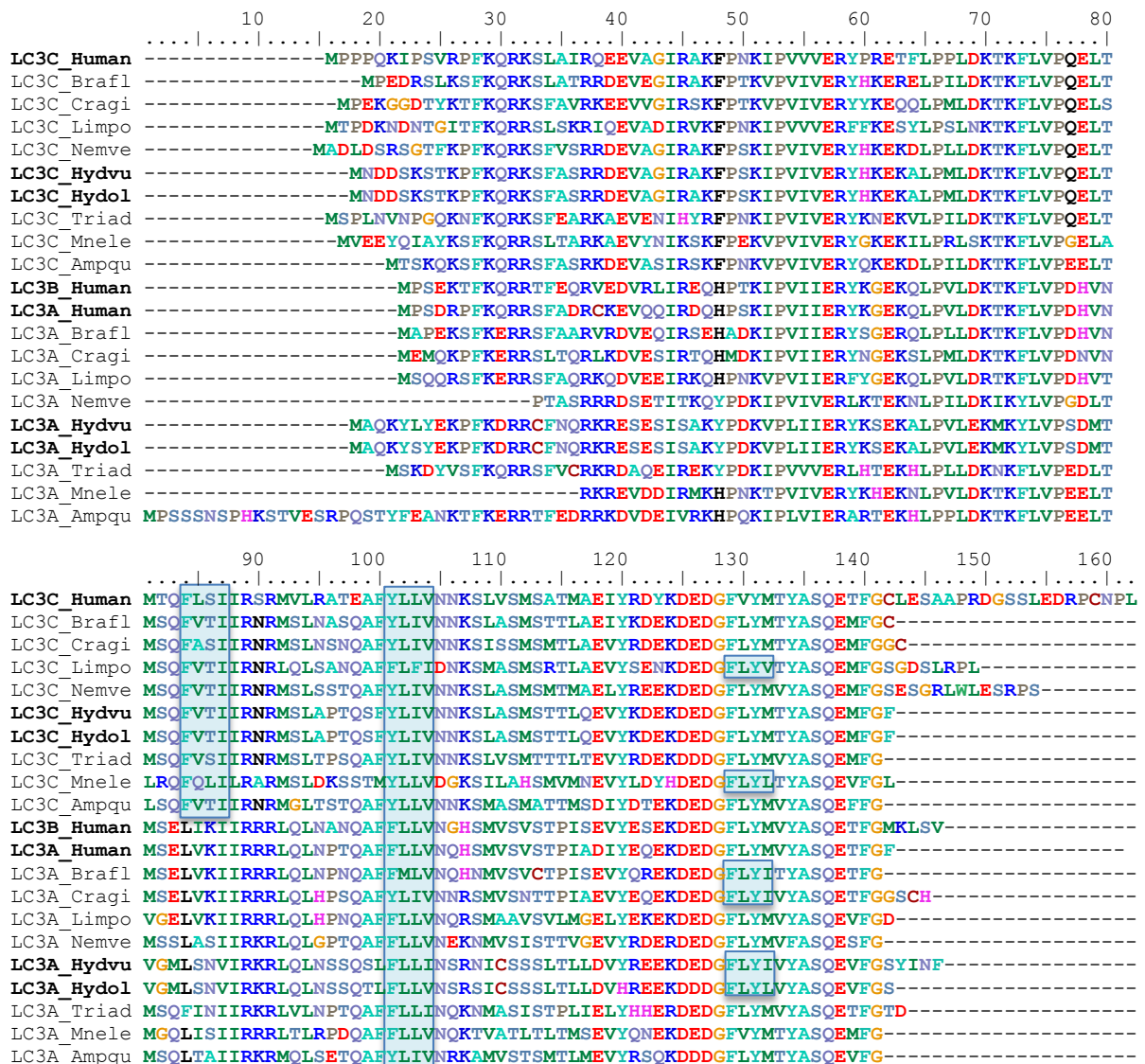


Figure S7: Alignment of the metazoan LC3/ATG8 protein sequences

The blue boxes indicate the LIR motifs with the core consensus sequence: [W/F/Y]xx[L/I/V] (Birgisdottir et al., 2013). Species abbreviations and accession numbers: **Ampqu:** *Amphimedon queenslandica* (demosponge, Porifera), LC3A: XM_003385475.2, LC3C: XM_003385524.2 (NCBI); **Brafl:** *Branchiostoma floridae* (amphioxus, Cephalochordata), LC3A: XM_002612378.1, LC3C: XM_002596383.1 (NCBI); **Cragi:** *Crassostrea gigas* (oyster, Mollusca), LC3A: XM_011449392.1, LC3C: XM_011417532.1 (NCBI); **Human:** LC3A: Q9H492, LC3B: Q9GZQ8, LC3C: Q9BXW4 (Uniprot); **Hydol:** *Hydra oligactis* (Cnidaria), LC3A: S043022c1g3_i01, R033468c0g1_i01, LC3C: S040689c0g1_i01, R036327c0g1_i01; **Hydru:** *Hydra vulgaris* (Cnidaria), LC3A: seq54452, LC3C: c26188_g3_i03, T2M644 (Uniprot); **Limpo:** *Limulus polyphemus* (horseshoe crab, Arthropoda), LC3A: XM_013930807.1, LC3C: XM_013919901.1 (NCBI); **Mnele:** *Mnemiopsis leidyi* (comb jelly, Ctenophora), LC3A: ML1904, LC3C: ML0233 (found in genome from compagen); **Nemve:** *Nematostella vectensis* (sea anemone, Cnidaria), LC3A: XM_001627787.1, LC3C: XM_001635074.1 (NCBI); **Triad:** *Trichoplax adhaerens* (Placozoa), LC3A: XM_002108002.1, LC3C: XM_002113115.1 (NCBI). See accession numbers of *Hydra* sequences in Table S3 and sequences on HydrATLAS.

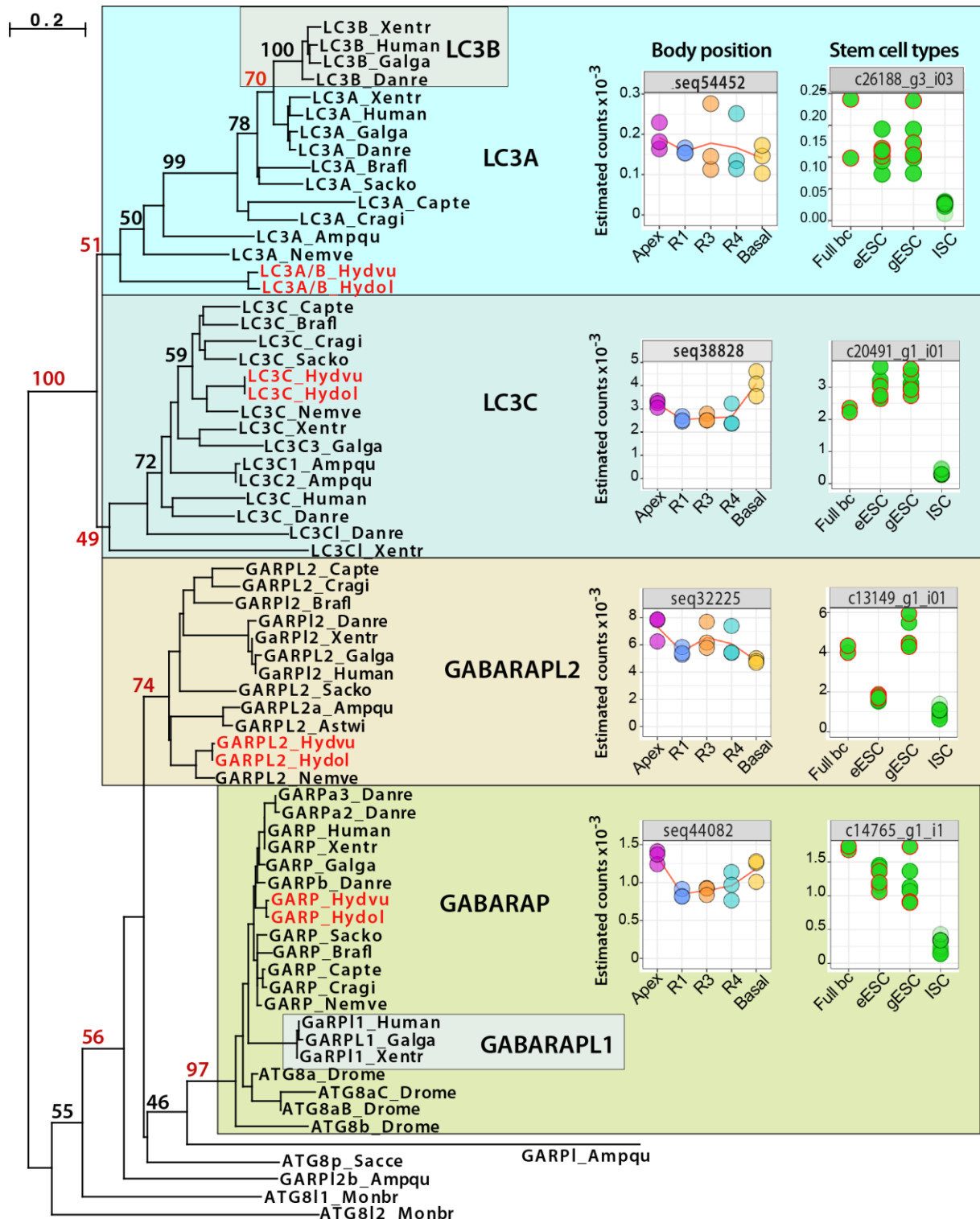


Figure S8: Phylogenetic analysis of the metazoan LC3/ATG8 gene families and RNA-seq profiles of the four *H. vulgaris* LC3-related genes

Phylogenetic tree of the LC3/ATG8 protein sequences aligned with MUSCLE and built with PhyML 3.0, tested with 100 bootstraps. *Hydra* sequences are written red. Species code is as follows: *Ampqu*: *Amphimedon queenslandica* (demo-sponge); *Capte*: *Capitella teleta* (polychaete worm); *Cragi*: *Crassostrea gigas* (oyster); *Danre*: *Danio rerio* (zebrafish); *Drome*: *Drosophila melanogaster* (fruitfly); *Galga*: *Gallus gallus* (chick); *Hydvu*: *Hydra vulgaris*; *Hydol*: *Hydra oligactis*; *Monbr*: *Monosiga brevicollis* (choanoflagellate); *Nemve*: *Nematostella vectensis* (sea anemone); *Sacce*: *Saccharomyces cerevisiae* (yeast); *Sacko*: *Saccoglossus kowalevskii* (acorn worm); *Xentr*: *Xenopus tropicalis* (Western clawed frog). The four main families MAP1LC3A (LC3A), MAP1LC3C (LC3C), GABARAPL2 (GARPL2) and GABARAP (GARP) include sequences from deuterostomes,

protostomes, cnidarians and poriferans. The GARPI_Ampqu sequence appears related to GABARAP although highly derived, while the two families LC3B and GABARAPL1 are vertebrate-specific duplications of LC3A and GABARAP respectively. Note the *Drosophila* sequences that all cluster in the GABARAP family. By contrast the non-metazoan sequences from yeast or choanoflagellates do not cluster in any of these four metazoan families. The graphs on the right show the RNA-seq profiles of the four LC3/ATG8 family members expressed in homeostatic *H. vulgaris*, along the body column (bc, left) and in each stem cell populations (right) as reported in ref. (Wenger et al., 2016; Wenger et al., 2019). Abbreviations: R1: upper body column, R3: upper mid-gastric region, R4: lower mid-gastric region, Foot: peduncle and basal disk; eESC: epidermal epithelial stem cells; gESC: gastrodermal epithelial stem cells; ISC: interstitial stem cells.

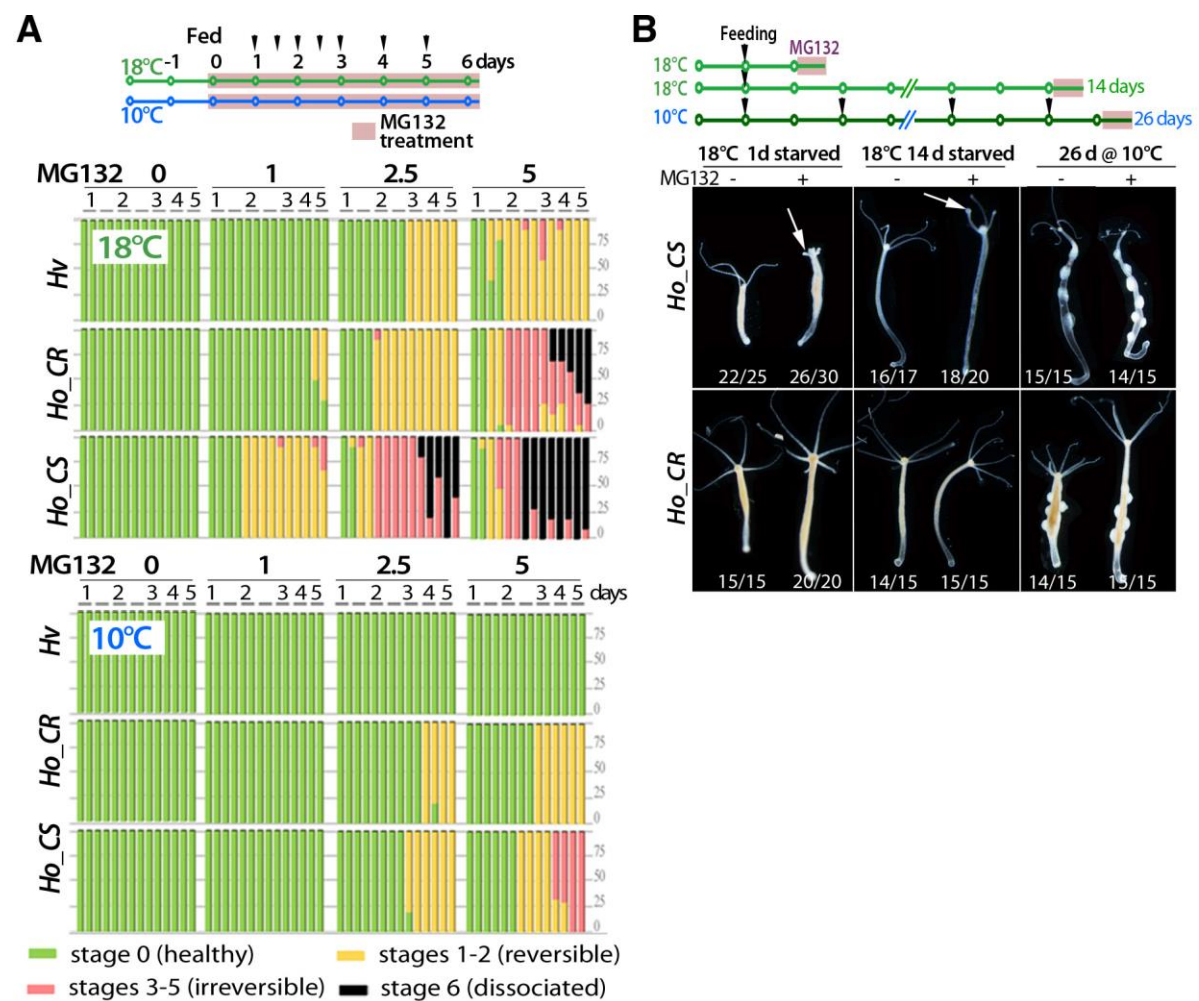


Figure S9: Different sensitivity to MG132 in *Ho_CS*, *Ho_CR* and *Hv*.

(A) Toxicity recorded in animals ($n = 2 \times 10$ /strain) maintained at 18°C (top) or 10°C (bottom) and continuously exposed to the proteasome inhibitor MG132 at indicated concentrations (0, 1, 2.5 or 5 μM) for 1, 2, 3, 4 or 5 days. (B) Resistance to proteasome inhibition tested in *Ho_CS* and *Ho_CR* animals exposed to MG132 (5 μM) for 16 hours and then pictured live. When maintained at 18°C, animals were either fed 4x a week or starved for 14 days, at 10°C animals were fed twice a week. Note the higher sensitivity of *Ho_CS* animals that rapidly exhibit shortened, “ball-shaped” tentacles (arrows) as signs of stress.

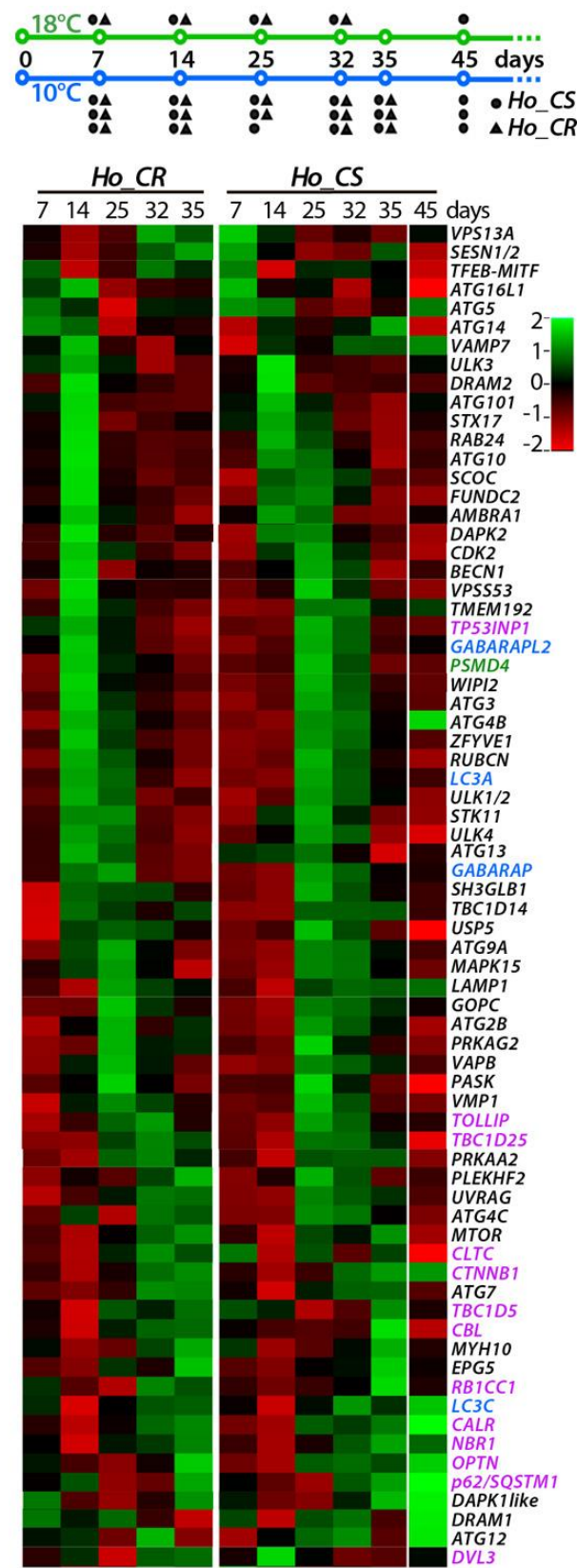
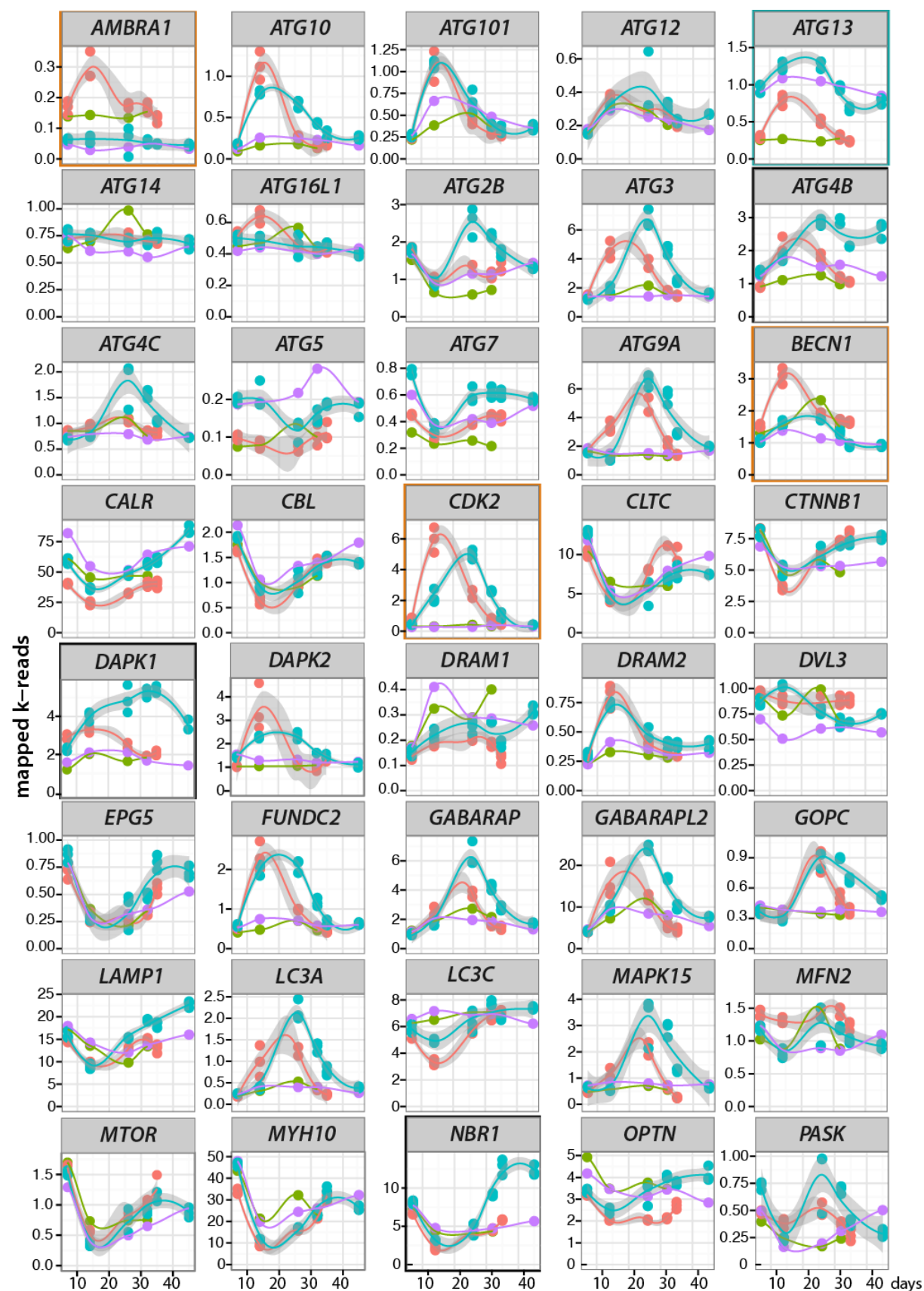
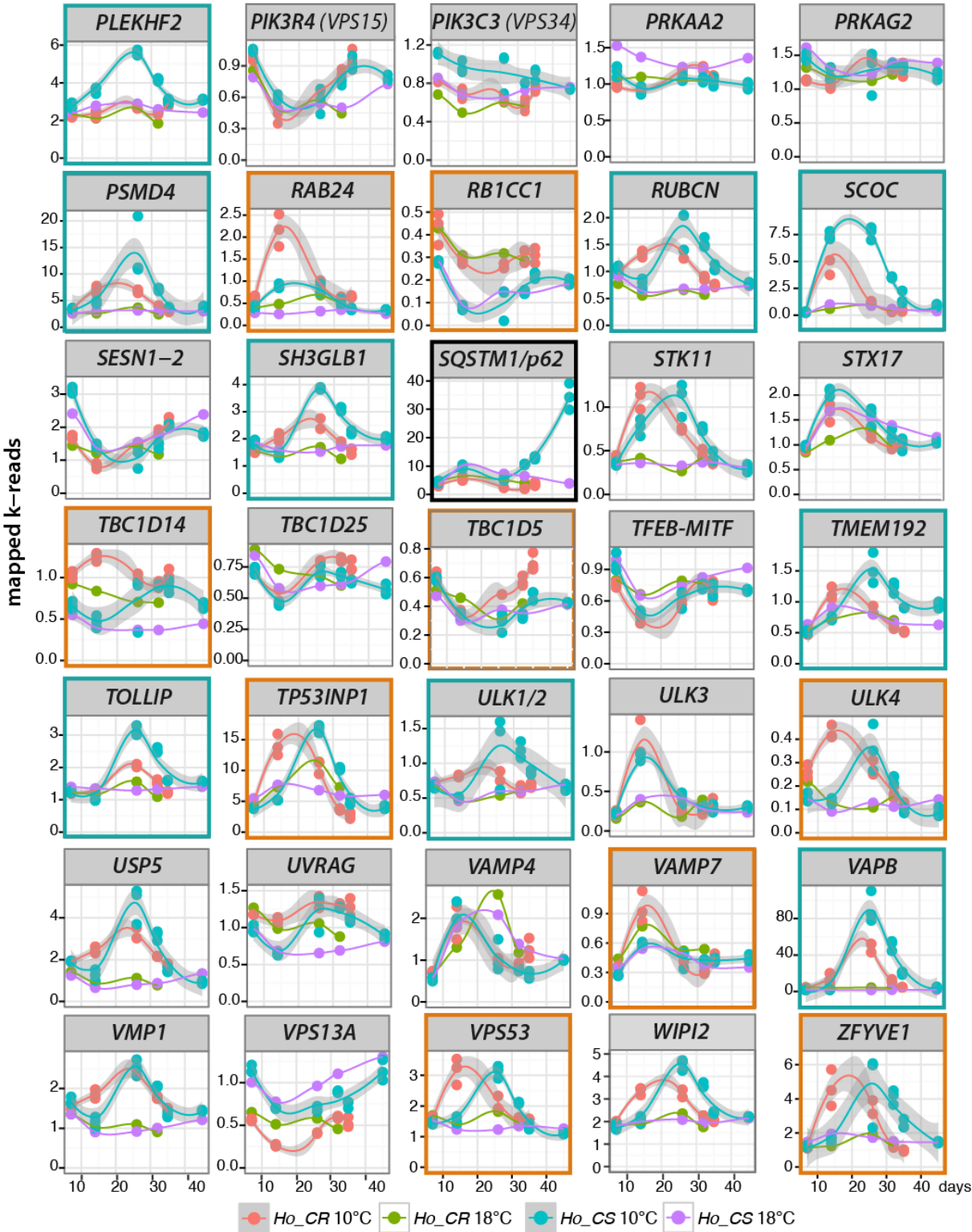


Figure S10: Comparative transcriptomic analysis of 75 *Hydra* orthologs to mammalian autophagy genes in *Ho_CS* and *Ho_CR*

Upper scheme: Experimental design of the quantitative RNA-seq analysis. RNAs from *Ho_CR* and *Ho_CS* animals were prepared at indicated time points with biological triplicates for animals maintained at 10°C. Lower panel: Heatmap showing the log2 fold changes of RNA-seq levels of 75 *Hydra* genes orthologous to human genes involved in autophagy. Fold changes are defined as ratio between the values measured at 10°C at a given time point over the value measured at 18°C at same or similar time point in a given strain. For technical details, see the Methods section. Gene names written **black** encode regulators of autophagy initiation and progression, **purple**: autophagy receptors or adaptors interacting with LC3/ATG8, **blue**: members of the LC3-GABARAP family, **green**: proteasome components. See the corresponding individual expression profiles in **Figure S11** and access to corresponding sequences in **Table-S3**. Note in *Ho_CS* the delayed activation of most autophagy genes and the late up-regulation of *NBR1* and *p62/SQSTM1*.





21/51 genes transiently up-regulated in both strains but delayed by 10 days in <i>Ho_CS</i> (10/20 exhibit higher levels in <i>Ho_CS</i> – underlined -)	<i>ATG3</i> , <i>ATG9A</i> , <i>ATG13</i> , <i>CDK2</i> , <i>DAPK2</i> , <i>GABARAP</i> , <i>GABARAPL2</i> , <i>LC3A</i> , <i>PSMD4</i> , <i>RUBCN</i> , <i>SCOC</i> , <i>SH3GLB1</i> , <i>STK11</i> , <i>TBC1D14</i> , <i>TMEM192</i> , <i>TP53INP1</i> , <i>ULK1/2</i> , <i>ULK4</i> , <i>VPS53</i> , <i>WIPI2</i> , <i>ZFYVE1</i>
14/51 genes similarly transiently up-regulated in <i>Ho_CS</i> and <i>Ho_CR</i> , peaking at day14 or day25, (underlined: exhibit higher levels in <i>Ho_CS</i>)	<i>ATG10</i> , <i>ATG101</i> , <i>ATG12</i> , <i>ATG9A</i> , <i>DRAM2</i> , <i>FUNDC2</i> , <i>GOPC</i> , <i>MAPK15</i> , <i>STX17</i> , <i>TOLLIP</i> , <i>ULK3</i> , <i>USP5</i> , <i>VAMP4</i> , <i>VAPB</i>
5/51 up-regulated in <i>Ho_CR</i> but poorly in <i>Ho_CS</i>	<i>AMBRA1</i> , <i>ATG16L1</i> , <i>BECN1</i> , <i>RAB24</i> , <i>VAMP7</i>
4/51 up-regulated in <i>Ho_CS</i> , not or poorly in <i>Ho_CR</i>	<i>ATG2B</i> , <i>ATG4C</i> , <i>PLEKHF2</i> , <i>TOLLIP</i>
7/51 genes sustainably up-regulated in <i>Ho_CS</i> , i.e. showing a temporal accumulation	<i>ATG4B</i> , <i>ATG7</i> , <i>CALRC</i> , <i>DAPK1</i> , <i>LAMP1</i> , <i>NBR1</i> , <i>p62/SQSTM1</i>

Figure S11: RNA-seq profiles of 75 *Hydra* orthologs to mammalian autophagy genes

RNA-seq expression profiles of 75 autophagy genes tested in *Ho_CR* and *Ho_CS* animals maintained at 18°C or at 10°C as depicted in **Figure_S10**. Orange frames indicate genes up-regulated in *Ho_CR* at 10°C but not at all or less in *Ho_CS*, blue frames indicate genes up-regulated in *Ho_CS* at 10°C but not at all or less in *Ho_CR*, black frames indicate genes that exhibit a sustained up-regulation at late time-points in *Ho_CS* but not in *Ho_CR*. Values on x axis = days, on y axis = mapped k-reads. For the corresponding sequences, see **Table S3**.

Development • Supplementary information

Figure S12: Alignment of vertebrate and non-vertebrate p62/SQSTM1 protein sequences

The alignment was obtained on MUSCLE (www.ebi.ac.uk/Tools/msa/muscle/) and manually corrected to align the functional domains as listed in refs (Seibenhener et al., 2004, Birgisdottir et al., 2013, Bitto et al., 2014): **PB1**, Phox and Bem1 domains (blue) involved in protein kinase binding; **ZZ**, ZZ-type zinc finger domain (green); **NLS1** and **NLS2**, nuclear localization signals 1 and 2 (turquoise); **NES**, nuclear export signal (grey); **LIR**, LC3- interacting region (green-yellow); **KIR**, KEAP-interacting region (beige); **UBA**, ubiquitin-associated domain (purple). In non-vertebrate sequences, the putative LIR, NLS and NES motifs were manually identified following the consensus sequence reported in refs (Pankiv et al., 2007) and (Birgisdottir et al., 2013): **LIR** = x₅(s) x₄(dt) x₃(desg) x₂(ds) [WFY] x₁(evtd) x₂(implt) [LIV] x₄(pdsr) x₅; **NLS** = [R] [K] x₁(vs) [K] or [K] [R] x₁(vs) [R]; **NES** = [L] x₁ x₂ x₃ (2, 3) [LIVFM] x₅ x₆ (2 or 3) [LI] x₇ [LI]. The UBA sequence used for raising the anti-*Hydra* p62/SQSTM1 antibody is underlined (KESKLERALSPAK). Species code and accession numbers are given in **Figure S13A** and **Table S3**.

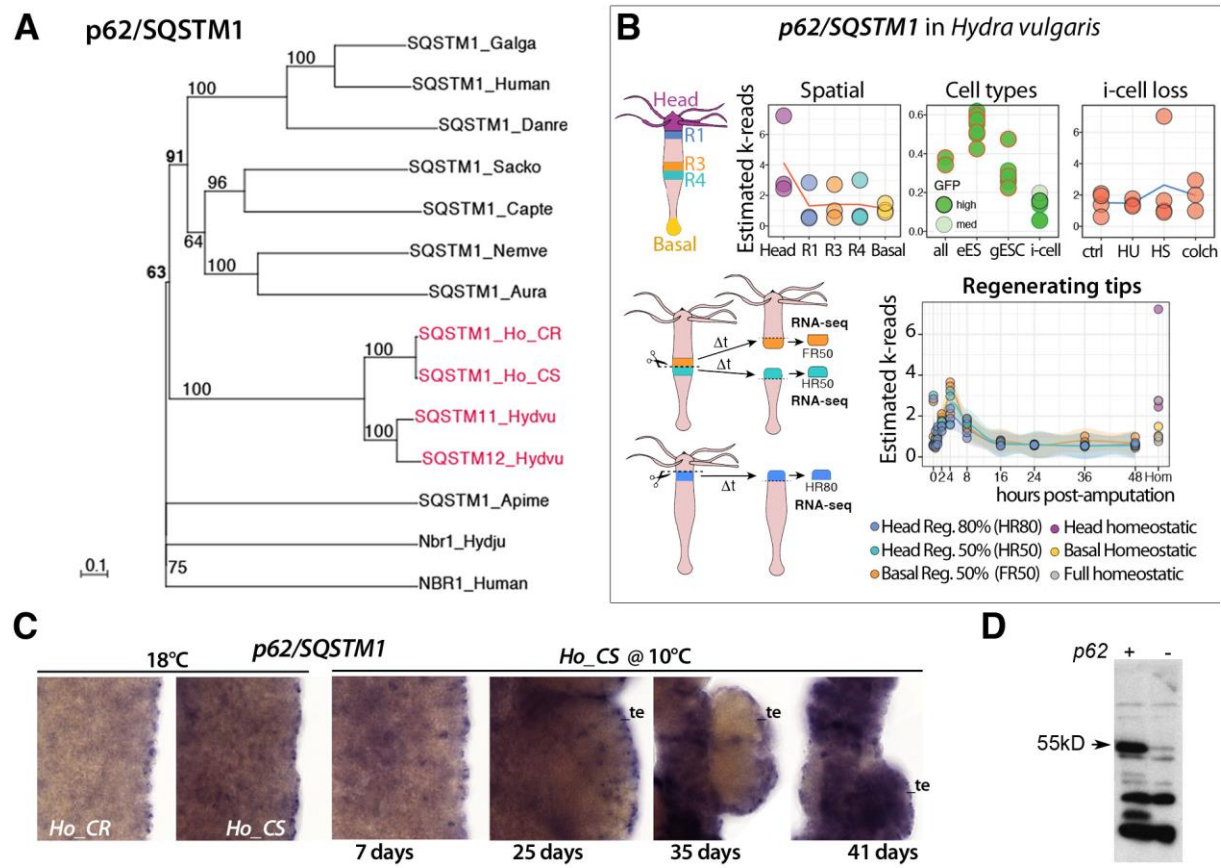
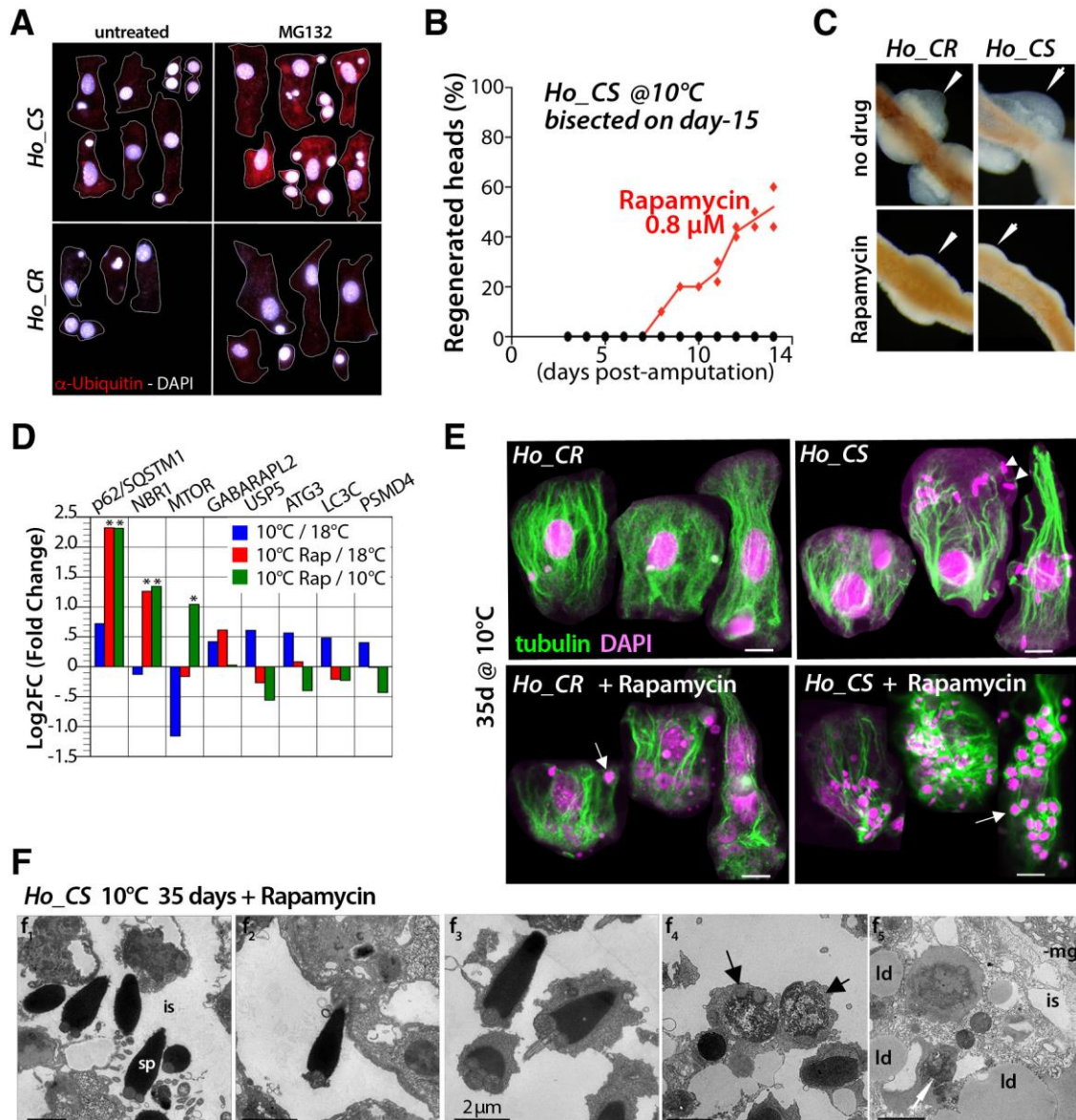
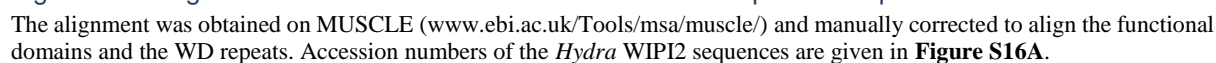


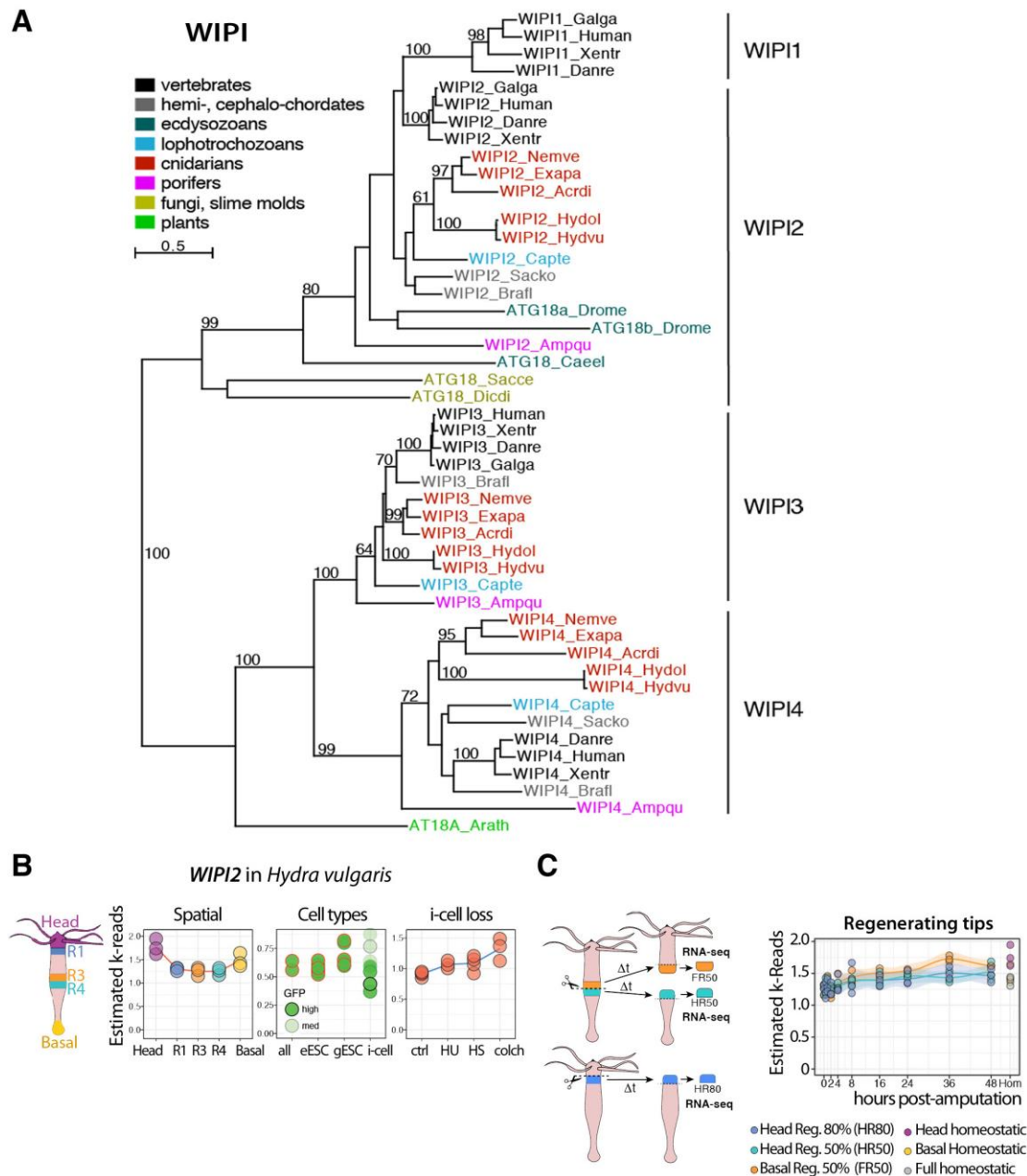
Figure S13: Phylogenetic tree and expression analysis of *p62/SQSTM1* in *Hydra*

(A) Phylogenetic tree of *p62/SQSTM1* protein sequences aligned with MUSCLE and built with PhyML 3.0, tested with 500 bootstraps. NBR1 sequences were used as outgroup. Species code and sequence accession numbers are for *Apime*: *Apis mellifera* (XP_392222.3); *Aurau*: *Aurelia aurita* (Q5EN85); *Capte*: *Capitella teleta* (gb|ELT88176.1); *Danre*: *Danio rerio* (Q6NWE4); *Galga*: *Gallus gallus* (F1NA86); *Human*: Q13501; *Ho_CS*, *Ho_CR*: *Hydra oligactis* (see **Table S3**); *Hydvu*: *Hydra vulgaris* (XP_004206050.1; T2MDZ6); *Nemve*: *Nematostella vectensis* (A7RN64); *Sacko*: *Saccoglossus kowalevskii* (XP_002737931.1). (B) RNA-seq profiles of *H. vulgaris* *p62/SQSTM1* as reported in (Wenger et al., 2014, Wenger et al., 2016, Wenger et al., 2019). **Body position**: expression measured at 5 distinct levels along the body axis of *H. vulgaris* Jussy strain; **Stem cell types**: expression measured in the three stem cell populations of *H. vulgaris* AEP (after FACS sorting cells of transgenic strains that constitutively GFP in one or the other cell type); **i-cell loss**: expression measured 10 days after the heat-shock or drug-induced elimination of cycling interstitial cells; **Regeneration**: expression measured in regenerating tips at 9 time points of three distinct regenerative processes in *H. vulgaris* Jussy strain (HR50, FR50: head or foot regeneration after mid-gastric bisection; HR80: head regeneration after decapitation). (C) Whole-mount *in situ* hybridization showing an ubiquitous expression of *p62/SQSTM1* in *Ho_CR* and *Ho_CS* at 18°C, progressively enhanced in epithelial cells of *Ho_CS* animals undergoing aging. (D) Testing of the anti-*Hydra* *p62/SQSTM1* antisera (batch 507) against the *Hydra* *p62/SQSTM1* protein expressed in TNT-coupled reticulocyte lysate (Promega) (lane +); the empty vector was used as negative control (lane -). The expected weight of *Ho_CS* *p62/SQSTM1* is 54.53 kD.

Figure S14: Anti-aging role of rapamycin in *Ho_CS Hydra*

(A) Immunodetection of ubiquitin in cells from *Ho_CS* and *Ho_CR* animals maintained at 18°C and exposed or not to MG132 for 16 hours. (B) A continuous exposure to rapamycin from day-2 after transfer to 10°C efficiency rescues head regeneration in *Ho_CS* bisected on day-15. (C) Testes (arrowheads) exhibit a reduced size in animals continuously exposed to rapamycin. (D) Proteomic analysis performed on *Ho_CS* animals maintained for 35 days either at 18°C or at 10°C where they were exposed or not to rapamycin for 32 days, *: 0.05, **: 0.001 significance. (E) Engulfed cells detected with an anti α -tubulin antibody (green) and DAPI staining (pink) in epithelial cells from *Ho_CS* and *Ho_CR* animals fixed after 36 days at 10°C. Arrows: nuclei from immature germ cells; arrowheads: sperm cell nuclei. (F) Sperm cells (sp) engulfed in epithelial cells of rapamycin-treated *Ho_CS* animals taken at 35 dpt. Sperm cells can be detected in the intracellular space (is, f1, f2), surrounded by cytoplasm (f3) and digested (f4, f5). Black arrows: mitochondria at the base of sperm cells. Abbreviations: is: intracellular space, ld: lipid droplet, mg: mesoglea. Scale bars = 2 μ m.



Figure S16: Phylogenetic and expression analysis of *WIP12* in *Hydra*

(A) Phylogenetic tree of WIP1 protein sequences aligned with MUSCLE and built with PhyML 3.0, tested with 100 bootstraps. Species code and sequence accession numbers: *Acrdi*: *Acropora digitifera* (coral, XP_015776989.1, XP_015752246.1, XP_015760656.1); *Ampqu*: *Amphimedon queenslandica* (XP_019853755.1, XP_003388703.1, XP_019850615.1); *Arath*: *Arabidopsis thaliana* (Q93VB2); *Brafl*: *Branchiostoma floridae* (XP_002599262.1, XP_002595393.1); *Capte*: *Capitella teleta* (ELT96465.1, ELU11552.1, ELT94793.1); *Danre*: *Danio rerio* (NP_956685.1, XP_005164182.1, Q7ZUW6, Q7ZUX3); *Dicdi*: *Dictyostelium discoideum* (Q54NA2); *Exapa*: *Exaaptasia pallida* (XP_020916524.1, XP_020900004.1, XP_020906575.1); *Galga*: *Gallus gallus* (XP_015135440.1, NP_001006162.1, Q5ZL16); *Human* (Q5MNZ9, Q9Y4P8, Q5MNZ6, Q9Y484); *Hydvu*: *Hydra vulgaris* (T2M354, T2M370, XP_012563670.1, XP_002163439.1); *Hydol* (*Ho_CS*: S022900c0g1, S037678c0g1, S028416c0g1; *Ho_CR*: R024157c0g1); *Nemve*: *Nematostella vectensis* (XP_001630626.1, XP_001626838.1, XP_001635768.1); *Sacce*: *Saccharomyces cerevisiae* (P43601); *Sacko*: *Saccoglossus kowalevskii* (XP_002739331.1, XP_006822202.1); *Xenla*: *Xenopus laevis* (Q6DCV0); *Xentr*: *Xenopus tropicalis* (NP_989387.1, XP_002941343.2, Q640T2). (B, C) RNA-seq profiles of *H. vulgaris* *WIP12* as reported in (Wenger et al., 2014, Wenger et al., 2016, Wenger et al., 2019). **Body position**: expression measured at 5 distinct levels along the body axis of *H. vulgaris* Jussy strain; **Stem cell types**: expression measured in the three stem cell populations of *H. vulgaris* AEP (after FACS sorting cells of transgenic strains that constitutively GFP in one or the other cell type); **i-cell loss**: expression measured 10 days after the heat-shock or drug-induced elimination of cycling interstitial cells; **regeneration**: expression measured in regenerating tips at 9 time points of three distinct regenerative processes in *H. vulgaris* Jussy strain (HR50, FR50: head or foot regeneration after mid-gastric bisection; HR80: head regeneration after decapitation).

SUPPLEMENTARY TABLES

Interstitial lineage genes	Full protein name	UniProt AC / RefSeq <i>Hv</i>	<i>Ho_CR</i> transcript id	<i>Ho_CS</i> transcript id
<i>CnASH</i>	Cnidarian achaete-scute homolog	Q25179	R025980c0g2_i01	S016491c0g1_i01
<i>Cnnos1</i>	Cnidarian nanos-homolog 1	Q9NDP0	R036747c0g1_i01	S031114c0g1_i01
<i>Cnnos2</i>	Cnidarian nanos-homolog 2	Q9NDN9	R033870c0g1_i01	S025194c0g1_i01
<i>cnos-2</i>	Cnos-2 homeoprotein	Q9NFM1	R023828c0g2_i01	S016662c0g1_i01
<i>COUP-TF1</i>	COUP-TF1 nuclear orphan receptor	Q66M18	R038175c0g3_i01	S036363c0g2_i02
<i>foxN1</i>	Forkhead box protein N1	T2MID9	R036487c0g1_i02	S040839c0g1_i02
<i>foxO</i>	FoxO transcription factor	J7HWF0	R038309c1g1_i02	S042977c0g1_i07
<i>Hyzic</i>	Zn-finger transcription factor 1	Q6T520	R067356c0g1_i01	S015485c0g1_i01
<i>Kazal-1</i>	Kazal-type serine protease inhibitor 1	Q1XEF1	R040495c0g3_i05	S040076c1g2_i07
<i>myc1</i>	C-Myc-binding protein 1	D0EM49	R028868c0g1_i01	S034530c0g2_i01
<i>Notch14</i>	neurogenic locus notch homolog protein like 4	XP_012557050.1	R036182c1g1_i01	S041501c1g1_i01
<i>NOWA</i>	Nematocyst outer wall antigen	Q8IT70	R038006c0g1_i01	S038314c1g1_i01
<i>Pax-A</i>	Paired-box homeoprotein A	Q02015	R031053c1g1_i01	S036858c0g5_i01
<i>POU4F2</i>	POU domain protein	T2MDR7	R026985c0g2_i02	S024242c0g1_i01
<i>prdl-b</i>	Paired-like homeoprotein b	Q62546	R031740c0g1_i01	S030596c0g1_i01
<i>Pumilio</i>	Pumilio domain-containing protein KIAA0020	T2MDF1	R039094c0g1_i02	S040698c0g1_i01
<i>RFamide-A</i>	Neuropeptide RFamide A	Q76948	R035154c0g1_i01	S036815c0g1_i01
<i>CnVas1</i>	Vasa-related protein CnVAS1	Q9GV13	R025460c0g1_i01	S033134c0g2_i01
<i>CnVas2</i>	Vasa-related protein CnVAS2	Q9GV12	R033160c0g1_i01	S042823c1g1_i02
<i>ZNF845</i>	Transcription factor ZNF845	I3V7W9	R003173c0g2_i01	S037612c0g1_i01

Table S1: Sequence Accession Numbers of 20 *H. vulgaris* (*Hv*) and *H. oligactis* (*Ho_CS*, *Ho_CR*) genes involved in proliferation and/or differentiation of interstitial cell (i-cell) lineages.

For the cold-induced RNA-seq profiles in *Ho_CS* and *Ho_CR*, see **supplemental Figure-S2**. For the spatial, cell-type, i-cell loss and regeneration RNA-seq profiles of the corresponding transcripts in *H. vulgaris*, see on HydrATLAS: <https://HydrATLAS.unige.ch> (Wenger et al., 2019).

Cell cycle orthologs	Full protein name	UniProt AC / RefSeq Hv	Ho_CR transcript id	Ho_CS transcript id
AURKA	Aurora kinase A	T2MJJ8	R027511c0g1_i04	S041489c3g2_i03
C12orf11	Cell cycle regulator Mat89Bb homolog	T2M413	R038671c0g1_i02	S041657c1g1_i02
CABLES1	CDK5 and ABL1 enzyme substrate 1	T2M990	R029958c0g1_i01	S029735c0g1_i01
CBP	CREB-binding protein	E9AI12	R039021c0g1_i04	S039796c0g2_i01
CCNA	mitotic-specific cyclin-A	P51986	R038551c0g1_i03	S039058c0g3_i03
CCNB	mitotic-specific cyclin-B	P51987	R038974c1g1_i01	S042648c3g5_i03
CCNB3	mitotic-specific cyclin-B3	T2M7Z1	R024808c0g2_i01	S036219c0g1_i01
CCND2	G1/S-specific cyclin-D2	T2MGB1	R031658c0g1_i05	S035897c0g1_i01
CCNF	Cyclin-F	T2M6V5	R033334c0g1_i01	S033757c0g1_i01
CDC123	Cell division cycle protein 123 homolog	T2MHK2	R038855c0g1_i05	S043547c1g1_i01
CDC16	Cell division cycle protein 16 homolog	T2MDN5	R021851c0g1_i01	S021110c0g1_i01
CDC20	Cell division cycle protein 20 homolog	T2MEB9	R032120c0g1_i02	S036535c0g1_i02
CDC23	Cell division cycle protein 23 homolog	T2M3J4	R036686c0g1_i04	S036439c0g1_i02
CDC27	Cell division cycle protein 27 homolog	T2MGT8	R035608c0g1_i01	S036141c0g1_i01
CDC42	Cell division control protein 42 homolog	T2MEG1	R038273c0g1_i01	S033376c0g1_i01
CDC45	Cell division control protein 45 homolog	T2MHN2	R039382c0g1_i02	S039367c0g6_i01
CDC5L	Cell division cycle 5-like protein	T2M796	R026217c0g1_i03	S038652c0g1_i03
CDC6	Cell division control protein 6 homolog	T2M680	R037875c0g1_i01	S030092c0g1_i01
CDC7	Cell division cycle 7-related protein kinase	T2MIW7	R027651c0g1_i02	S035902c0g1_i01
CDC47L	Cell division cycle-associated 7-like protein	T2M7K7	R030222c0g1_i01	S033291c0g1_i01
DIAPH2	Protein diaphanous homolog 2	T2MIT5	R037202c0g1_i01	S041348c0g1_i02
DOT1L	Histone-lysine N-methyltransferase, H3 lysine-79 specific	T2M8S1	R033812c0g1_i01	S037123c0g1_i01
E2F4	Transcription factor E2F4	T2MCU6	R029967c0g1_i01	S008670c0g2_i01
FGFR	Fibroblast growth factor receptor	Q86PM4	R033445c0g1_i01	S034028c0g1_i01
FNTB	Protein farnesyltransferase subunit beta	T2MFI9	R007519c0g1_i01	S003373c0g1_i01
GAS2L1	GAS2-like protein 1	T2M790	R033006c0g2_i01	S034987c0g1_i01
HUS1	Checkpoint protein HUS1	T2MIV2	R011216c0g1_i01	S029062c1g1_i04
ING4	Inhibitor of growth protein	T2M3P3	R035845c0g1_i01	S001006c0g1_i01
KATNA1	Katanin p60 ATPase-containing subunit A1	T2MHM7	R033726c0g1_i01	S035284c0g1_i02
LIN52	Protein lin-52 homolog	T2MBY0	R015400c0g2_i01	S024491c0g1_i01
LIN9	Protein lin-9 homolog	T2MBY8	R032851c0g1_i01	S027133c0g1_i01
MFN2	Mitofusin-2	T2MHD7	R038385c0g1_i01	S030617c0g1_i01
MIIP	Migration and invasion-inhibitory protein	T2MC10	R033074c0g2_i01	S037583c1g1_i01
MNAT1	CDK-activating kinase assembly factor MAT1	T2MF88	R035361c2g1_i01	S042834c3g1_i02
MRE11A	Double-strand break repair protein MRE11A	T2MFZ1	R037286c0g1_i01	S039847c0g1_i02
NPDC1	Neural proliferation differentiation and control protein 1	T2M4U6	R031720c0g1_i01	S038708c0g1_i01
PA2G4	Proliferation-associated protein 2G4	T2M2R0	R038317c0g1_i01	S041220c0g1_i01
PFAH1B1	Lissencephaly-1 homolog	T2MFT1	R036160c0g1_i01	S039362c0g1_i02
PLK1	Serine/threonine-protein kinase PLK1	T2MFR1	R038084c0g2_i01	S038822c0g1_i01
PLK4	Serine/threonine-protein kinase PLK4	T2MJ85	R031836c0g1_i01	S034548c0g2_i02
RAD1	Cell cycle checkpoint protein RAD1	T2MID6	R031826c0g1_i01	S036513c0g3_i02
RAD17	Cell cycle checkpoint protein RAD17	T2MIH3	R040845c0g1_i01	S041741c2g1_i01
RAD9A	Cell cycle checkpoint control protein RAD9A	T2M799	R040444c0g1_i02	S040626c0g1_i01
RSK	Ribosomal protein S6 kinase	E9AI11	R023522c0g2_i01	S008723c0g1_i01
SAV1	Protein salvador homolog 1	T2M622	R038127c0g1_i01	S040596c0g1_i02
SEPT2	Septin-2	T2MD65	R035337c0g1_i01	S039793c0g2_i01
SIPAIL3	Signal-induced proliferation-associated 1-like protein 3	T2MIG6	R036824c0g2_i01	S042925c0g3_i05
TFDP1	Transcription factor Dp-1	T2MDH4	R001653c0g1_i01	S030116c0g1_i02
TMEM30A	Cell cycle control protein 50A	T2M525	R031410c0g1_i01	S038468c1g1_i01
TTC28	Tetratricopeptide repeat protein 28	T2M8B7	R038479c0g1_i04	S041972c0g1_i02
TTK	Dual specificity protein kinase TTK	T2MG79	R008001c0g1_i01	S028488c0g1_i01
USPL1	Ubiquitin-specific peptidase-like protein 1	T2MBR4	R036743c0g1_i02	S040029c0g1_i06

Table S2: Sequence Accession Numbers of 52 *H. vulgaris* (Hv) and *H. oligactis* (Ho_CS, Ho_CR) orthologs to mammalian genes involved in cell cycle and cell proliferation.

For the comparative analysis of the expression of these genes after transfer to cold in Ho_CS and Ho_CR, see **Figure S3** and **Figure S4**. For the spatial, cell-type, i-cell loss and regeneration RNA-seq profiles of the corresponding transcripts in *H. vulgaris*, see on HydrATLAS: <https://HydrATLAS.unige.ch> (Wenger et al., 2019).

Autophagy orthologs	Full protein name	Hv UniProt / RefSeq	Ho_CR transcript id	Ho_CS transcript id
AMBRA1	Activating molecule in BECN1-regulated autophagy protein 1	T2M6D7	R033532c0g1_i01	S034160c0g2_i01
ATG10	Ubiquitin-like-conjugating enzyme ATG10	T2M5V2	R030322c0g1_i01	S032762c0g1_i01
ATG101	Autophagy-related protein 101	T2M6Y4	R055757c0g1_i01	S071050c0g1_i01
ATG12	Ubiquitin-like protein ATG12	T2MIE8	R029364c0g1_i01	S036036c1g1_i01
ATG13	Autophagy-related protein 13	T2MI85	R029409c0g1_i01	S043484c2g1_i01
ATG14	Beclin 1-associated autophagy-related key regulator	T2MBM0	R036673c0g1_i04	S028223c0g2_i02
ATG16L1	Autophagy-related protein 16-1	T2MC97	R036776c1g1_i01	S036117c0g1_i02
ATG2B	Autophagy-related protein 2 homolog	T2M8E3	R026665c0g1_i01	S042169c0g1_i01
ATG3	Autophagy-related protein 3	T2M4W2	R035592c1g1_i05	S040217c0g1_i08
ATG4B	Cysteine protease ATG4B	T2M2V7	R038184c0g1_i02	S037421c1g1_i01
ATG4C	Cysteine protease ATG4C	T2M7B1	R037362c0g1_i03	S043278c1g1_i01
ATG5	Autophagy protein 5	T2M5L4	R021841c0g2_i01	S030832c0g1_i01
ATG7	Ubiquitin-like modifier-activating enzyme ATG7	T2MHR4	R036000c4g1_i04	S040163c0g1_i04
ATG9A	Autophagy-related protein 9A	T2MBB7	R032526c0g4_i02	S041696c3g4_i01
BECN1	Beclin1	T2MDF4	R040450c1g2_i06	S043504c0g1_i03
CALR	Calreticulin	T2MFY9	R015676c0g2_i01	S028677c1g1_i01
CBL	E3 ubiquitin-protein ligase CBL	T2MG42	R038366c0g1_i02	S034365c0g1_i01
CDK2	Cyclin-dependent kinase 2	T2MG16	R026975c0g1_i01	S026262c0g1_i01
CLTC	Clathrin heavy chain	T2MEN5	R038444c0g1_i01	S039376c0g1_i02
CTNBN1	b-catenin	T2MGP6	R031422c0g1_i01	S035025c0g1_i01
DAPK1/MYLK1	Myosin light chain kinase	XP_012566973.1	R040005c0g1_i01	S042661c1g1_i01
DAPK2	Death-associated protein kinase 2	T2M3L1	R037170c1g1_i01	S035730c0g1_i04
DRAM1	DNA damage-regulated autophagy modulator protein 1	T2M9Y1	R010350c0g1_i01	S017218c0g1_i01
DRAM2	DNA damage-regulated autophagy modulator protein 2	T2MB87	R029953c0g1_i01	S037063c0g1_i02
DVL3	Dishevelled-like	Q9GTJ8	R035715c0g1_i01	S028887c0g3_i01
EPG5	Ectopic P granules protein 5 homolog	T2M4L4	R033380c0g1_i03	S041881c0g1_i01
FUNDC2	FUN14 domain-containing protein 2	T2M6E3	R034657c0g1_i01	S040426c0g1_i01
GABARAP	Gamma-aminobutyric acid receptor-associated protein	T2MID2	R034299c0g1_i01	S041977c0g1_i01
GABARAPL2	Gamma-aminobutyric acid receptor-associated protein like 2	T2MFA6	R040572c3g1_i01	S042989c1g3_i05
GOPC	Golgi-associated PDZ and coiled-coil motif-containing protein	T2M5L1	R025782c0g1_i01	S021196c0g1_i01
LAMP1	Lysosome-associated membrane glycoprotein 1	T2MGK4	R034674c0g2_i01	S037683c2g1_i01
LC3A/B	Microtubule-associated proteins 1A/1B light chain 3A	XP_012555909.1	R033468c0g1_i01	S043022c1g3_i01
LC3C	Microtubule-associated proteins 1A/1B light chain 3C	T2M644	R036327c0g1_i01	S040689c0g1_i01
MAPK15	Mitogen-activated protein kinase	T2M8C8	R032105c0g1_i01	S035992c0g1_i02
MFN2	Mitofusin	T2MHD7	R038385c0g1_i01	S030617c0g1_i01
mTOR	S/T protein kinase Target of Rapamycin	T2MFU7	R038760c0g1_i01	S039716c0g1_i01
MYH10	Myosin-10	T2MG36	R041168c0g3_i01	S043809c0g1_i03
NBR1	Next to BRCA1 gene 1 protein	XP_002169141.3	R036941c0g1_i01	S037290c0g1_i02
OPTN	Optineurin	T2M7C5	R030608c0g1_i01	S040493c0g1_i01
P62/SQSTM1	Sequestosome-1	T2MDZ6	R040075c0g1_i01	S041284c0g1_i03
PASK	PAS domain-containing serine/threonine-protein kinase	T2M7L6	R035698c0g1_i02	S035923c0g3_i01
PIK3R4 (VPS15)	Phosphoinositide 3-kinase regulatory subunit 4	T2M6A2	R032824c0g1_i01	S033802c0g1_i01
PIK3C3 (VPS34)	Phosphatidylinositol 3-kinase catalytic subunit type 3	T2M8P5	R028513c0g2_i01	S037049c0g1_i01
PLEKHF2	Pleckstrin homology domain-containing family F member 2	T2M5S9	R038718c0g1_i02	S041724c0g1_i01
PRKAA2	5'-AMP-activated protein kinase catalytic subunit alpha-2	T2MFI8	R036403c0g1_i02	S039556c0g1_i01
PRKAG2	5'-AMP-activated protein kinase subunit gamma-2	T2M3A1	R037932c0g1_i02	S042780c0g5_i04
PSMD4	26S proteasome non-ATPase regulatory subunit 4	T2MFE9	R032102c0g1_i01	S038651c0g3_i01
RAB24	Ras-related protein Rab-24	T2M8J9	R033692c0g2_i01	S043114c1g3_i01
RB1CC1	RB1-inducible coiled-coil protein 1	T2M8Y6	R040512c0g1_i04	S040101c0g1_i01
RUBCN	Run domain Beclin-1-interacting Cys-rich domain-cont. protein	T2M8H1	R033800c0g1_i02	S036891c0g1_i01
SCOC	Short coiled-coil protein	T2M358	R027960c0g1_i01	S031987c0g1_i01
SESN1-2	Sestrin-1	T2M1Y1	R034652c0g1_i01	S030353c0g1_i01
SH3GLB1	Endophilin-B1	T2M3B1	R022339c0g1_i02	S031988c0g1_i03
STK11	Serine/threonine-protein kinase 11	T2MDA0	R028673c0g1_i01	S030765c0g1_i01
STX17	Syntaxin-17	T2MEJ3	R038040c0g1_i05	S040560c0g1_i01
TBC1D14	TBC1 domain family member 14	T2M3G3	R035499c0g1_i01	S042386c0g3_i01
TBC1D25	TBC1 domain family member 25	T2MCX7	R024677c0g1_i03	S037186c0g1_i04
TBC1D5	TBC1 domain family member 5	T2M8P8	R001078c0g2_i01	S027212c0g1_i01
TFEB (MITF)	Transcription factor EB	T2MHT1	R032064c0g1_i03	S029890c0g1_i01
TMEM192	Transmembrane protein 192	T2MAC7	R025234c0g1_i04	S029317c0g1_i01
TOLLIP	Toll-interacting protein	T2M581	R032916c0g1_i01	S064218c0g1_i01
TP53INP1	Tumor protein p53-inducible nuclear protein 1	XP_012566192.1	R036441c0g1_i01	S042256c0g3_i01
ULK1/2	Serine/threonine-protein kinase ULK1/2	XP_002167716.3	R034566c0g1_i03	S032016c0g3_i01
ULK3	Serine/threonine-protein kinase ULK3	T2MBQ7	R023417c0g1_i01	S030594c0g1_i01
ULK4	Serine/threonine-protein kinase ULK4	T2M8D5	R038809c0g1_i01	S035052c0g2_i01
USP5	Ubiquitin carboxyl-terminal hydrolase 5	T2MFQ7	R035151c0g1_i02	S036059c0g1_i03
UVRAG	UV radiation resistance-associated gene protein	T2M3F0	R011659c0g1_i01	S031929c0g1_i02
VAMP3	Vesicle-associated membrane protein 3	T2MCV8	not found	not found
VAMP4	Vesicle-associated membrane protein 4	T2MI55	R007986c0g1_i01	S030362c0g1_i01
VAMP7	Vesicle-associated membrane protein 7	T2MF92	R033884c0g3_i01	S021726c0g1_i01
VAPB	Vesicle-associated membrane protein-associated protein B/C	T2MI95	R039749c0g1_i02	S037148c1g2_i01
VMP1	Vacuole membrane protein 1	T2M837	R031782c0g1_i01	S033370c0g1_i04
VPS13A	Vacuolar protein sorting-associated protein 13A	T2M7E9	R036423c0g1_i01	S039033c0g1_i01
VPS53	Vacuolar protein sorting-associated protein 53	T2MBJ0	R032923c0g1_i05	S035892c0g2_i03
WIP1	WD repeat domain phosphoinositide-interacting protein 2	T2M354	R024157c0g1_i01	S022900c0g1_i02
ZFYVE1	Zinc finger FYVE domain-containing protein 1	T2M5M0	R008385c0g2_i01	S030332c0g1_i01

Table S3: Sequence Accession Numbers of 75 *H. vulgaris* (Hv) and *H. oligactis* (Ho_CS, Ho_CR) orthologs to the mammalian autophagy genes.

For the comparative analysis of the cold-induced gene modulations in *Ho_CR* and *Ho_CS*, see the **Figure S10** and **Figure S11**. For the spatial, cell-type, i-cell loss and regeneration RNA-seq profiles of corresponding transcripts in *H. vulgaris*, see on HydrATLAS: <https://HydrATLAS.unige.ch> (Wenger et al., 2019).

Gene names	Primer names	Primer sequences
mCherry	mCherry-for1	CAGGGGCCCTGGGATCCCCATGGCCGATGATGAAGTTGC
	mCherry-rev1	AGTTCTTCTCCTTTACTCATTTTATATAATTCATCCATTCCACCTG
eGFP	eGFP-for1	TGGAATGGATGAATTATATAAAATGAGTAAAGGAGAAGAACTTTTC
	eGFP-rev1	TACTTCTGAGCCATGCATGCTTTGTATAGTTCATCCATGCCA
hyLC3A/B	LC3A-for1	GCTGGATGAAGTATACAAAGCATGCATGGCTCAGAAGTA
	LC3A-rev1	CGCGCGAGGCAGATCGTCAGGAATTCTTAAAAATTAATGTAAGAACCAA

Table S4: Sequences of the primers used to build the mCherry-GFP-LC3A autophagy sensor

Gene names	siRNA names	siRNA sequences
p62/SQSTM1 <i>H. oligactis</i>	Ho-p62-siRNA1	CAAAGCUUCUGAAGUUUCA
	Ho-p62-siRNA2	CUCAAAUGGCUGCUAAUUA
	Ho-p62-siRNA3	AGAACAUGUUGGAGUUACU
p62/SQSTM1 <i>H. vulgaris</i>	Hv-p62-siRNA1	CAACGUUUCUGAAGUUAUA
	Hv-p62-siRNA2	UGCAAGCAAUAAUGAAGAA
	Hv-p62-siRNA3	AGCCAGCUCAAUCAAUAA
WIPI2 <i>H. vulgaris</i>	WIPI2_siRNA1	GCAAAUGGAGCCGAUCCUU
	WIPI2_siRNA2	GCAACUUAAGCUAUCCUAA
	WIPI2_siRNA3	GGAAGAACCAAGUAGCCAA
scrambled	scramble-siRNA	AGGUAGUGUAAUCGCCUUG

Table S5: Sequences of the siRNA primers used to silence *p62/SQSTM1* and *WIPI2*

Targeted protein	Type	Raised in	Supplier	Ref. number	Dilution /IF	Dilution/ WB
Ubiquitin	monoclonal	mouse	Enzo Life Sciences	BML-PW0755-0025	1:200	NA
Ubiquitin	monoclonal	rabbit	Abcam	ab137025	NA	1:2000
Human LC3B	polyclonal	rabbit	Novus Biologicals	nb100-2220	1:300	1:1000
Hydra p62/SQSTM1	polyclonal	mouse	Delphi Genetics	custom made	1:200	1:1000
Sea urchin α-tubulin	monoclonal	mouse	Sigma-Aldrich	T5168	1:300	NA
Sea urchin β-tubulin	monoclonal	mouse	Sigma-Aldrich	T5293	NA	1:2000

Table S6: List of the antibodies used in this study.

	<i>Ho_CS</i>						<i>Ho_CR</i>						<i>Hv</i>					
Day post-HU	C1	C2	C3	C4	C5	C6	C1	C2	C3	C4	C5	C6	C1	C2	C3	C4	C5	C6
0	10	10	10	10	10	10	10	10	10	10	10	10	10	10	10	10	10	10
3	10	10	10	9	10	10	10	10	10	10	10	10	10	10	10	10	10	10
7	10	10	10	9	10	10	10	10	10	9	10	10	10	10	10	10	10	10
11	10	9	7	9	10	10	10	10	10	9	10	10	10	10	10	10	10	10
15	10	9	7	9	10	10	10	10	10	9	10	10	10	10	10	10	10	10
21	10	9	7	9	10	10	10	10	10	9	10	10	10	10	10	10	10	10
26	8	9	5	9	9	9	9	9	10	8	9	10	10	10	10	10	10	10
30	8	9	4	7	9	7	6	9	8	8	7	8	10	10	10	10	10	10
34	5	4	2	2	5	3	1	3	3	4	2	2	10	10	10	10	10	10
38	2	1	1	1	4	2	0	2	1	1	0	2	10	10	10	10	10	10
42	1	0	1	0	1	2	0	0	0	0	0	0	10	10	10	10	10	9
46	0	0	0	0	0	0							9	9	9	10	10	9
49													9	9	9	10	8	9
52													9	9	8	10	8	9
58													8	7	7	10	8	6
63													6	6	6	8	7	4
65													5	5	5	8	6	4
70													3	4	4	8	5	4
74													3	4	4	6	5	4
77													3	4	4	6	4	4
81													3	4	4	6	3	4
85													2	2	0	4	3	3
88													1	1	0	4	3	2
93													1	1	0	2	3	1
100													0	0	0	0	0	0

Table-S7: Number of animals at different days after HU release (Figure 2I raw data). C: cohort.

Day at 10°C	Ho_CS						Ho_CS +0.8 μ M Rapamycin					
	Cohort1	Cohort2	Cohort3	Cohort4	Cohort5	Cohort6	Cohort1	Cohort2	Cohort3	Cohort4	Cohort5	Cohort6
0	10	10	10	10	10	10	10	10	10	10	10	10
10	10	10	10	10	10	10	10	10	10	10	10	10
14	10	10	10	10	10	10	10	10	10	10	10	10
18	10	10	10	10	10	10	10	10	9	10	10	10
22	10	10	10	10	10	10	10	10	9	10	10	10
28	10	10	10	10	10	10	10	10	9	10	10	10
33	9	9	9	10	8	9	10	10	9	10	10	10
37	6	9	9	8	7	9	10	10	9	10	10	10
41	2	8	6	6	5	7	10	10	9	10	10	9
45	1	7	5	5	5	6	10	10	9	10	10	9
49	1	4	5	3	5	6	10	8	9	9	10	7
53	1	4	2	2	5	3	8	7	8	8	10	7
56	1	4	1	1	2	3	7	6	8	7	10	6
59	0	4	0	1	1	2	7	4	8	7	10	4
65	0	2	0	1	1	1	7	1	7	5	7	3
70	0	2	0	1	0	1	4	0	6	5	4	2
72	0	2	0	1	0	1	4	0	6	5	4	2
77	0	2	0	0	0	1	4	0	6	5	2	1
81	0	2	0	0	0	1	4	0	6	3	2	1
84	0	2	0	0	0	1	4	0	6	3	1	1
89	0	1	0	0	0	1	3	0	6	3	1	1
93	0	0	0	0	0	0	2	0	5	2	1	1
95							1	0	4	2	1	1
100							1	0	3	1	1	0
107							1	0	3	1	0	0
113							1	0	2	0	0	0

Table-S8: Number of animals at different days after transfer to 10°C release, continuously exposed or not to rapamycin (0.8 μ M) (Figure 6B raw data).

SUPPLEMENTARY MOVIES



Movie 1: 3D-reconstruction of LC3 decorated p62/SQSTM1 bodies

LC3 decorated p62/SQSTM1 bodies identified in epithelial cells of *Ho_CS* polyps macerated after 35 days at 10°C. Image acquired on a Leica SP8 confocal microscope, 3D reconstruction performed with Bitplane Imaris.



Movie 2: 3D-reconstruction of an epithelial cell having engulfed germ cells identified in 35 days old *Ho_CS* polyps treated with Rapamycin

3D reconstruction with Bitplane Imaris of the confocal image of engulfed germ cells decorated with p62/SQSTM1 or p62/SQSTM1-LC3 in e-cells of *Ho_CS* polyp maintained at 10°C for 35 days and continuously treated with Rapamycin.

SUPPLEMENTARY REFERENCES

- Birgisdottir, A. B., Lamark, T. and Johansen, T.** (2013). The LIR motif - crucial for selective autophagy. *J Cell Sci*, **126**, 3237-47.
- Bitto, A., Lerner, C. A., Nacarelli, T., Crowe, E., Torres, C. and Sell, C.** (2014). P62/SQSTM1 at the interface of aging, autophagy, and disease. *Age (Dordr)*, **36**, 9626.
- Pankiv, S., Clausen, T. H., Lamark, T., Brech, A., Bruun, J. A., Outzen, H., Overvatn, A., Bjorkoy, G. and Johansen, T.** (2007). p62/SQSTM1 binds directly to Atg8/LC3 to facilitate degradation of ubiquitinated protein aggregates by autophagy. *J Biol Chem*, **282**, 24131-45.
- Seibenhener, M. L., Babu, J. R., Geetha, T., Wong, H. C., Krishna, N. R., Wooten, M. W.** (2004). Sequestosome1/p62 is a polyubiquitin chain binding protein involved in ubiquitin proteasome degradation. *Mol Cell Biol*, **24**, 8055-8068. doi: 10.1128/MCB.24.18.8055-8068.2004
- Wenger, Y., Buzgariu, W. and Galliot, B.** (2016). Loss of neurogenesis in Hydra leads to compensatory regulation of neurogenic and neurotransmission genes in epithelial cells. *Philos Trans R Soc Lond B Biol Sci*, **371**, 20150040.
- Wenger, Y., Buzgariu, W., Reiter, S. and Galliot, B.** (2014). Injury-induced immune responses in Hydra. *Semin Immunol*, **26**, 277-294.
- Wenger, Y., Buzgariu, W., Perruchoud, C., Loichot, G., Galliot, B.** (2019). Generic and context-dependent gene modulations during Hydra whole body regeneration. *BioRxiv* 587147, doi.org: 10.1101/587147